ABSTRACT

THE ANALYSIS AND THE THREE-DIMENSIONAL, FORWARD-FIT MODELING OF THE HARD X-RAY AND THE MICROWAVE EMISSIONS OF MAJOR SOLAR FLARES

by
Natsuha Kuroda

Solar flares are one of the most violent and energetic space weather events that are known to cause various adverse effects on the Earth. One of the major problems that must be solved to understand flares and to be able to predict their magnitudes is how the particles in the solar atmosphere are accelerated after the magnetic reconnection. One way to help solve this problem is to investigate the properties of the high energy electrons produced during the flare impulsive phase, observed in the hard X-ray (HXR) and microwave (MW). The two emissions are considered to be produced by a "common population" of the electrons, but some studies have also reported temporal, spatial, and energy discrepancies between them, challenging the widely-used notion. In order to truly understand the relationship between the two emissions, high-cadence observations must be made simultaneously in two wavelengths, both temporally and spatially, and the spectral inversion must also be spatially-resolved and done in a realistic magnetic field geometry.

In this dissertation, the properties of the high energy electrons produced in two major solar flares, the 2011-02-15 X2.2 flare and the 2015-06-22 M6.5 flare, are investigated, using the high-cadence HXR and MW observations, and the advanced three-dimensional modeling tools. For the 2011-02-15 X2.2 flare, the time delays, source locations, spectral indices, and their temporal evolution of the HXR and the MW emissions during the impulsive phase are investigated using observations made by the Reuven Ramaty High Energy Solar Spectroscopic Imager (RHESSI) and the Nobeyama Radio Observatory (NoRO). For the 2015-06-22 M6.5 flare, the realistic three-dimensional, forward-fit modeling of the HXR and the MW

emission is conducted at one point in time during flare, using the Non-Linear Force Free Field (NLFFF) model extrapolated from the observed photospheric magnetic field, the three-dimensional multi-wavelength modeling tool *GX Simulator*, and the observational constraints provided by the RHESSI and the new Expanded Owens Valley Solar Array (EOVSA).

The major results in the 2011-02-15 M2.2 flare study are: (1) the multiple peaks simultaneously observed in the HXR and the MW during the impulsive phase came predominantly from two locations that suggest two separate episodes of magnetic reconnection, which can be interpreted in terms of tether-cutting flare scenario, (2) the transition between these two episodes occur more slowly in MW, suggesting the trapped nature of the MW-emitting electrons, and (3) the asymmetry in the HXR and MW emission intensity is observed, which can be explained by the asymmetry in the magnetic field strengths discussed in several previous studies. The major results in the 2015-06-22 M6.5 flare study are: (1) the low frequency part of the observed MW spectrum is modeled to be dominated by the emission from a "HXR invisible" source containing a non-negligible number of nonthermal electrons in a large volume of weak magnetic field, (2) the modeled electron populations in the "HXR visible" sources fit the standard flare model, with the thermal population interpreted as the result of chromospheric evaporation and the nonthermal population having an upward break in its power-law energy spectrum, producing HXR and MW emission in different energy range, and (3) the model can be successfully made with a post-reconnection magnetic field configuration. The results from this work motivate further modeling efforts, which have the potential to contribute to the prediction of the intensity of flare soft X-ray (SXR) emission and the Solar Energetic Particles (SEPs).

THE ANALYSIS AND THE THREE-DIMENSIONAL, FORWARD-FIT MODELING OF THE HARD X-RAY AND THE MICROWAVE EMISSIONS OF MAJOR SOLAR FLARES

by
Natsuha Kuroda

A Dissertation
Submitted to the Faculty of
New Jersey Institute of Technology and
Rutgers, The State University of New Jersey – Newark
in Partial Fulfilment of the Requirements for the Degree of
Doctor of Philosophy in Applied Physics

Federated Physics Department

August 2017

APPROVAL PAGE

THE ANALYSIS AND THE THREE-DIMENSIONAL, FORWARD-FIT MODELING OF THE HARD X-RAY AND THE MICROWAVE EMISSIONS OF MAJOR SOLAR FLARES

Natsuha Kuroda

Dr. Haimin Wang, Dissertation Co-Advisor — Date
Distinguished Professor of Physics, NJIT

Dr. Dale E. Gary, Dissertation Co-Advisor — Date
Distinguished Professor of Physics, NJIT

Dr. Gregory D. Fleishman, Committee Member — Date
Distinguished Research Professor of Physics, NJIT

Dr. Andrew J. Gerrard, Committee Member — Date
Professor of Physics, NJIT

Dr. Lucia Kleint, Committee Member — Date
Senior Researcher, University of Applied Sciences Northwestern Switzerland

BIOGRAPHICAL SKETCH

Author: Natsuha Kuroda

Degree: Doctor of Philosophy

Date: August 2017

Undergraduate and Graduate Education:

- Doctor of Philosophy in Physics,
  New Jersey Institute of Technology, Newark, NJ, 2017
- Bachelor of Physics,
  University of Maryland, College Park, MD, 2012

Major: Applied Physics

Presentations and Publications:

Kuroda, N., Gary, D. E., Wang, H., Fleishman, G. D., Nita, G. M., & Jing, Ju., "Three-dimensional forward-fit modeling of the hard X-ray and the microwave emissions of the 2015-06-22 M6.5 flare", *The Astrophysical Journal, under preparation*

Kuroda, N., Wang, H., & Gary, D. E., "Observation of the 2011-02-15 X2.2 Flare in the Hard X-Ray and Microwave", *The Astrophysical Journal*, vol. 807, pp. 124, 2015.

Kuroda, N., Wang, H., & Gary, D. E., "Hard X-ray and Microwave Simulation of 2015-06-22 M6.6 flare", *AAS/Solar Physics Division Meeting*, Boulder, Colorado, May 31-June 3, 2016.

Kuroda, N., Wang, H., & Gary, D. E., "Observation of the 2011-02-15 X2.2 Flare in the Hard X-ray and Microwave", *AAS/Solar Physics Division Meeting*, Boston, Massachusetts, June 2-5, 2014.

Kuroda, N., Wang, H., & Gary, D. E., "Time delays between microwave and HXR observed during the 2011-02-15 X2.2 solar flare", *LWS/SDO Science Workshop*, Cambridge, Maryland, March 3-8, 2013.

Gary, D. E., Kuroda, N., Fleishman, G., et al., "Initial Observations of Solar Bursts with the Expanded Owens Valley Solar Array", *AAS/AGU Triennial Earth-Sun Summit*, Indianapolis, IN, April 26-30, 2015.

Kuroda, N., & Christe, S., "The Flare Productivity of Active Regions", *AGU Fall Meeting*, San Fransisco, CA, December 3-7, 2012.

Kuroda, N., & Gopalswamy, N., "The Relation Between Solar Active Region Location and The Lowest Frequency of Type III Emission", *AGU Fall Meeting*, San Fransisco, CA, December 14-18, 209.

To my parents and my partner, who gave me the strength and the perseverance I needed to finish this work.

ACKNOWLEDGMENT

First, I would like to express my deepest gratitude for my advisors, Dr. Haimin Wang and Dr. Dale E. Gary, for their continuous support and encouragement throughout the research I have done in here at NJIT. Their mentoring has been so great, and I learned from them so much, to always keep learning, to think with a broad perspective, to always keep questioning, and so much more that I cannot list all in here. I will always be looking up to them and the qualities they had as scientists as I navigate through my career. I was extremely lucky to be their graduate student.

I would like to thank Dr. Gregory D. Fleishman, for becoming my committee member and being a great mentor throughout my second project presented in this thesis. He spent so much time answering even the smallest, seemingly too simple questions I asked him about the flare radio and X-ray emissions, and I could not have finished this work without his helps.

I would also like to thank Dr. Gelu M. Nita, for his tireless efforts in improving the simulation software that was a driving force behind the main work of this dissertation. My work turned out to be one of the most complicated case for his invention that demanded many upgrades, but he always provided me with something better than what I asked for when I turned to him for help.

I would like to thank Dr. Andrew J. Gerrard, for becoming my committee member and also for his work as a professor of the *George Ellery Hale Collaborative Graduate Education Program in Solar & Space Physcs* classes. His passion and efforts to bring solar and terrestrial disciplines in the space weather research community together was so admirable, and they always stimulated me to think about my research problems in broader perspective and bigger picture.

I would like to thank Dr. Lucia Kleint, for spending her time to be in my thesis committee, for asking many critical questions about this dissertation, and for being

one of the most inspiring young scientists in our research community. Her research and beautiful presentations have been something I have always been looking up to as a graduate student, and I feel very lucky to know that someone with so much talents will always be ahead of me and lead our solar research community.

I would like to extend my sincere gratitude to all the professors in the Center for Solar-Terrestrial Research and the Department of Physics. I would like to thank Dr. Ju Jing for providing me with an important data component used in this thesis. I would like to thank Dr. Alexander G. Kosovichev for his essential lectures in the Basic Plasma Physics.

I sincerely thank the administrative staff of our group, Ms. Cheryl E. James, Ms. Christine A. Oertel, Ms. Felicia Margolies, Ms. Cindy Montalvo-Harden, and Ms. Leslie M. Williams, for their daily works to make the research work easier and helpful for students.

Special thanks goes to my friends/classmates/co-workers at the Center for Solar-Terrestrial Research, who always lightened up the mood and accompanied my works in the classrooms and research office. I believe that we developed a special bond as we navigate through our graduate study.

I would like to thank my partner, Kohei, for his encouragement and moral support. Thank you for your patience while you listened to my speech about my research, for asking simple questions that inspired me to think about my research problems more deeply, and for your support at every hardship I encountered throughout this study. I am forever indebted to your companionship.

Last, but not least, I would like to share my biggest thanks to my parents, Yahiro Kuroda and Kazuteru Kuroda, for their endless moral support and inspiring me to keep moving forward during the difficult times. Your words and wisdom always encouraged me to not to give up and helped me restore the confidence in

myself at the right moments. This thesis would not have been possible without their encouragement.

This dissertation was supported in parts by NSF grants AST-1312802, AGS-1348513, AGS-1408703, and NASA grants NNX14AC87G, NNX13AG13G, and NNX16AF72G to New Jersey Institute of Technology. My advisors and I are grateful to Dr. Stephen White at the U.S. Air Force Research Laboratory for providing us with the brightness temperature data of NoRP 17 GHz channel, and Dr. Kazumasa Iwai at the Nobeyama Radio Observatory for helping us obtain NoRH and NoRP data used in the work presented in Chapter 2. I am also forever indebted to the the Gary Thomas Fellowship from the Office of the Provost of the New Jersey Institute of Technology, which gave me an invaluable time during the first two years of the program to concentrate on my research and advance in the competitive field of academia.

TABLE OF CONTENTS

TABLE OF CONTENTS
(Continued)

Chapter **Page**

LIST OF TABLES

Table **Page**

LIST OF FIGURES

LIST OF FIGURES
(Continued)

Figure **Page**

LIST OF FIGURES
(Continued)

Figure **Page**

LIST OF FIGURES
(Continued)

Figure **Page**

LIST OF FIGURES
(Continued)

Figure **Page**

LIST OF FIGURES
(Continued)

Figure **Page**

CHAPTER 1

INTRODUCTION

1.1 The Active Sun

For many centuries, the Sun was believed to be a constant, perfect celestial object that provides the energy for the lives on the Earth endlessly and harmlessly. Some scientists, however, knew about the existence of the "imperfect" sunspots as early as seventeenth century (Usoskin 2017), and in 1843, the 11-year sunspot number cycle was discovered by Samuel H. Schwabe. Not long after that, in 1859, Richard Carrington made a first observation of the solar flare, one of the transient, eruptive events that occur on the Sun. The observation was followed by an associated world-wide disruption of the telegraph communication network, and thus the event became the first known example of the Sun's variability that can actually harm our livelihoods on the Earth. Over the years that followed, it became apparent that the Sun actually shows a variety of these eruptive activities, and that many of them can be quite harmful to our society under certain conditions, especially in modern days when we are increasingly dependent on space-borne assets such as GPS or communication satellites. Today we call the study of such Solar variability and its effects on the Earth "Space Weather", and it is of a great interest to both the scientists who investigate the physical mechanisms behind these phenomena, and the general public who need the fore-warning and the mitigation in the case of adverse events (National Science and Technology Council 2015).

1.1.1 Overview of Solar Flares

One of the most violent and energetic space weather events is the solar flare, which is observationally defined as a brightening of any emission across the electromagnetic spectrum occurring at a time scale of minutes to hours (Benz 2017). Operationally,

although historically defined according to the appearance in Hα, it is more recently defined in terms of a sudden brightening in X-rays, with the most widely-known scale being the peak flux (W/m^2) of the 1 - 8 $\mathring{A}$ channel of the *Geostationary Operational Environmental Satellite* (*GOES*) that is located near Earth. Table 1.1 shows the classification of the flare magnitude in GOES scale.

Table 1.1 Flare Magnitude Classification According to the Peak Flux in 1-8 $\mathring{A}$ Channel of GOES Satellite.

Classification	**Peak flux range at *GOES* 1-8 $\mathring{A}$ [$\frac{\mathbf{W}}{\mathbf{m^2}}$]**
A	$< 10^{-7}$
B	10^{-7} - 10^{-6}
C	10^{-6} - 10^{-5}
M	10^{-5} - 10^{-4}
X	$> 10^{-4}$

Within each logarithmic class, the magnitude is measured in linear scale from 1 to 9. For example, an M4 flare (peak flux of 4×10^{-5} W/m^2) is 2 times "larger" than an M2 flare, and 10 times "larger" than a C4 flare. The largest flare ever recorded since the regular recordings of this kind started in 1968 was the one observed on November 4, 2003, with the estimated size of X25-45. The event took place during the so-called "Halloween storm" of 2003, when a number of X-class flares and the subsequent geomagnetic storms caused space weather hazards on the Earth (Schwenn 2006). The uncertainty was in fact due to the saturation of the detector caused by the extreme amount of radiation (the detector limit was X17.4). The size of the flare

recorded by Richard Carrington in 1859 is estimated to be X45 ±5 (Cliver & Dietrich 2013), arguably one of the largest flares ever recorded.

It is well known that larger flares occur less often than smaller flares because they require more energy. According to the Space Weather scale issued by the National Oceanic and Atmospheric Administration (NOAA), the events with the size above X20 occur less than 1 per 11-year solar cycle, and for less intense events, the frequency rises, such as 175 per cycle (140 days per cycle) for X1 events and 2000 per cycle (950 days per cycle) for M1 events (http://www.swpc.noaa.gov/noaa-scales-explanation). Overall, the size distribution of flares (over a certain measure of flare size, such as flare duration or peak flux in soft X-rays) are known to obey a power-law (Crosby et al. 1993), with the indices for the peak soft X-ray (SXR) flux distribution in the range 1.7-2.15 (Aschwanden et al. 1998; Wheatland 2005). Figure 1.1 shows the probability density function for the peak flux of events recorded by the GOES 1-8 $\mathring{A}$ channel in 1975-2003. The power-law index above a nominal threshold of 4×10^{-6} W/m^2 (vertical line) was calculated to be $\sim$2.15 ±0.01.

The temporal evolution of a flare can be roughly divided into three phases: *precursor*, *impulsive*, and *gradual* phases (Kane 1974), although the occurrence and the duration of each phase greatly differ from event to event. Figure 1.2 shows the schematic representation of these phases observed in different wavelengths across the electromagnetic spectrum.

The *precursor* phase is generally recognized by the slow increase in the radiation, especially in SXR and extreme ultra-violet (EUV), caused by the heating of the coronal plasma. They indicate the possible occurrence of the explosive behavior within the following tens of minutes. This phase is also often associated with the emergence of magnetic field into the solar surface (*flux emergence*), which contributes to the build-up of magnetic free energy within the solar atmosphere (Shibata & Magara 2011). Sometimes, transient nonthermal emissions that can be observed in

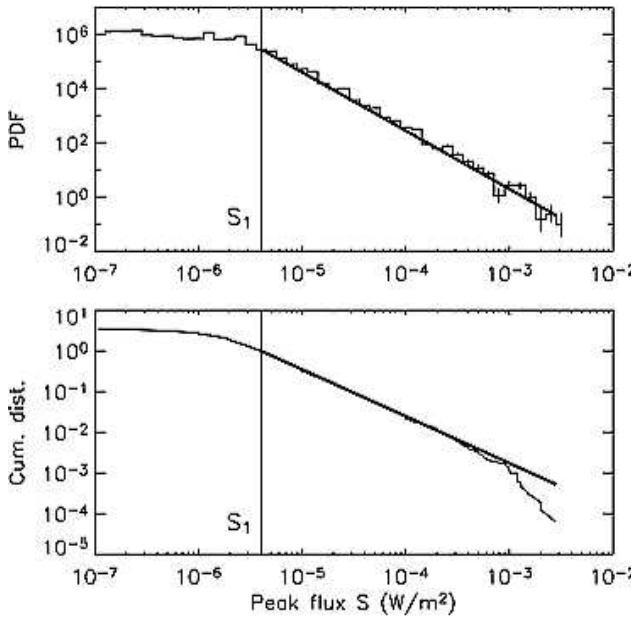

Figure 1.1 (top) Probability density function for the peak flux (1-8 $\mathring{A}$) of GOES events 1975-2003, together with the threshold S1 (vertical line) and the power law model (thick line). (bottom) Cumulative distribution. Source: *Wheatland (2005).*

hard X-rays (HXRs) and microwaves (MWs) occur at locations different from later phases (Wang et al. 2017). In the *impulsive* phase, magnetic reconnection occurs, in some cases multiple times, and the development of this phase can be most closely followed in HXRs and MWs, which show spiky time profiles. Most of the magnetic energy stored in the flaring region is released during this phase, and the released energy can go up to 10^{33} ergs. One type of radio burst, called "type III" radio burst that drift rapidly across a few decades of radio frequencies, is also characteristic of this phase. The *gradual phase* usually refers to the time after the impulsive phase maximum, when the SXR (and the Hα) flux reaches their maxima more slowly and then gradually subsides to pre-flare levels.

The geo-effectiveness of the flare is of great concern because their X-ray and EUV radiation can ionize the Earth's ionosphere and cause radio blackouts, and furthermore, the EUV radiation can heat the outer atmosphere of the Earth and increase the drag on low-orbiting satellites (Schwenn 2006). Solar flares are often

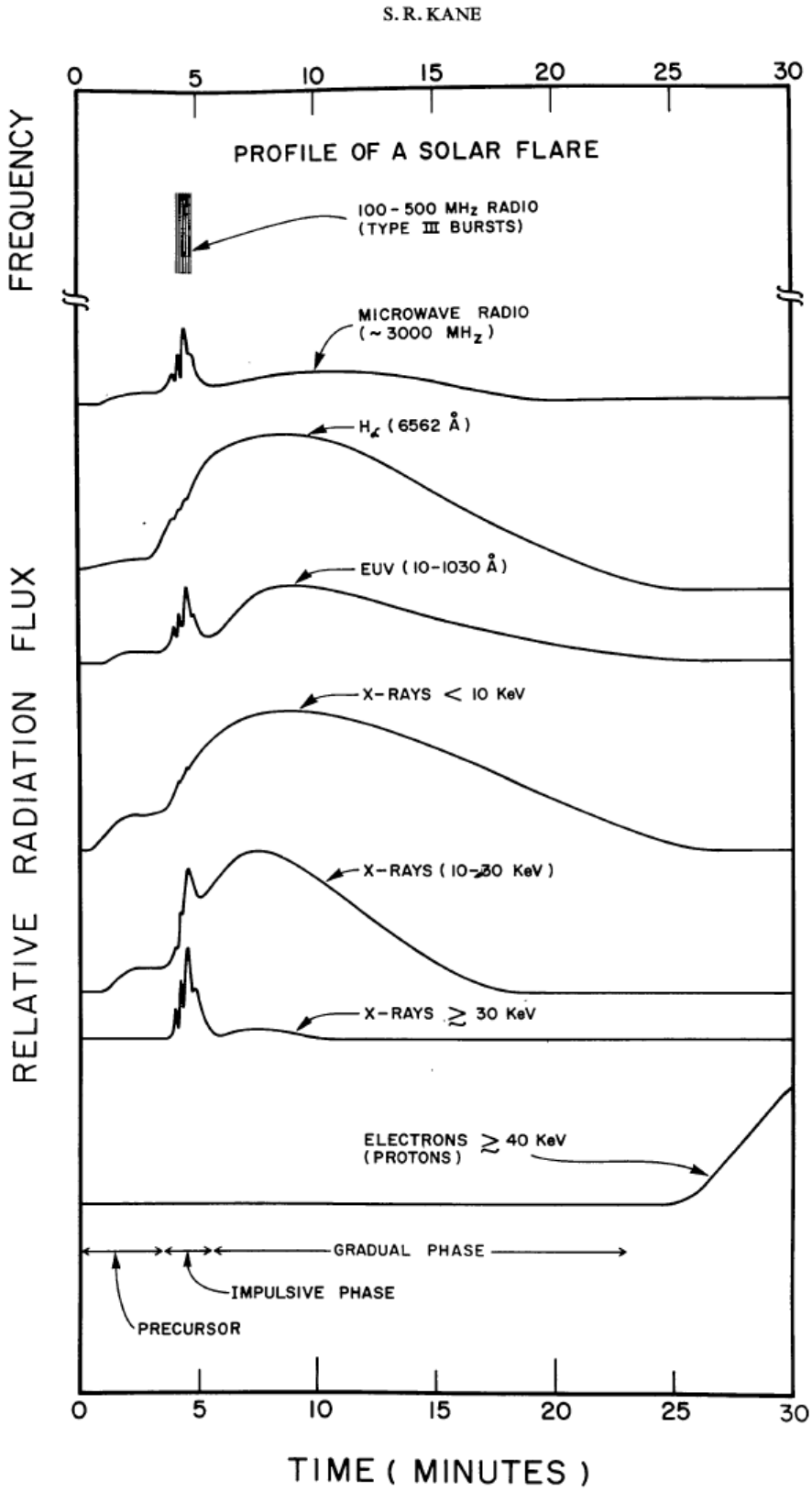

Figure 1.2 A schematic representation of the different phases of a flare observed in different wavelengths across the electromagnetic spectrum. Source: *Kane (1974)*.

associated with Coronal Mass Ejections (CMEs) and Solar Energetic Particles (SEPs), which are both detrimental in terms of the effects on the Earth. CMEs are gigantic clouds of plasma and magnetic fields ejected from the Sun into the interplanetary space that may hit the Earth a few hours or days later (depending on their speed) and initiate geomagnetic storms. Their measured front speeds can reach nearly 3000 km/s, and the total energy (kinetic plus potential energy) can reach some 10^{33} erg (Schwenn 2006). Although not all flares are associated with CMEs, large flares tend to be associated with them (Forbes 2000; Gopalswamy 2004), and the geomagnetic storms triggered by the arrivals of CMEs cause significant consequences such as disruptions in radio communications, surface charging and positioning errors of the satellites, increased radiation dosage for the flight passengers at high altitudes, and possibly a wide-spread power outage and pipeline corrosion (Schwenn 2006). SEPs are electrons and ions that are accelerated near flare sites and from shock waves in the corona and in the interplanetary space up to some GeVs, and they can endanger the space probes and the lives of unprotected astronauts traveling outside the Earth's magnetosphere (Schwenn 2006).

Because of these potential effects on human activities, the understanding of flare mechanisms and their roles in CME and SEP production are becoming increasingly important. However, the research community has not yet reached a consensus among competing theories about how flares are triggered, how their particles are accelerated, and how various flare parameters are related to those of CMEs and SEPs. This dissertation will be focusing on the high-energy electrons produced during the flare impulsive phase, which will help us understand the flare's particle acceleration mechanism. Although ions are often energetically more important, they are much harder to measure because of their lower efficiency in production of electromagnetic emission, hence the electrons must serve as a proxy.

1.1.2 The Standard Flare Model

The widely accepted model for a solar flare is the Standard magnetic reconnection model, referred to as the Carmichael, Sturrock, Hirayama, Kopp and Pneuman, or "CSHKP" model (Carmichael 1964; Sturrock 1966; Hirayama 1974; Kopp & Pneuman 1976). This model assumes that magnetic reconnection in the solar corona is the initiator of magnetic energy release during solar flares. Magnetic reconnection occurs when the magnetic fields of the active region become increasingly twisted over time, and oppositely directed field lines interact with each other.

Figure 1.3 shows the two-dimensional picture of the standard flare model (Lin & Forbes 2000). In the upper panel, magnetic reconnection occurs in the current sheet, and the plasma outflow is ejected to both upward and downward direction. The upward outflow and the reconnected magnetic fields become part of a launching CME. In the lower panel, the downward flow impacts the lower coronal loop and can produce HXR loop-top emission via bremsstrahlung. At this acceleration site, electrons can be accelerated to mildly-relativistic speed (with non-thermal energy), and those that have access to open field lines escape to the interplanetary space and produce type-III radio bursts. Others travel further down along the field lines until they are stopped by the dense, cooler chromosphere, where they give rise to footpoint HXR emissions and Hα emission (flare ribbon). The downward-traveling electrons with larger pitch angles can get trapped due to the effect of the magnetic mirroring at the ends of the loop, and they emit radiation in MW range. Meanwhile, some of the energy released in the corona is transported to the chromosphere via thermal particles behind magneto-acoustic shocks. Reacting to the bombardment of nonthermal particles and the heat conduction from corona, the temperature in the chromosphere increases and the chromospheric plasma expands. The expanded plasma "evaporates" along the magnetic field lines and fills the lower loops, thus giving rise to somewhat delayed EUV and SXR emission.

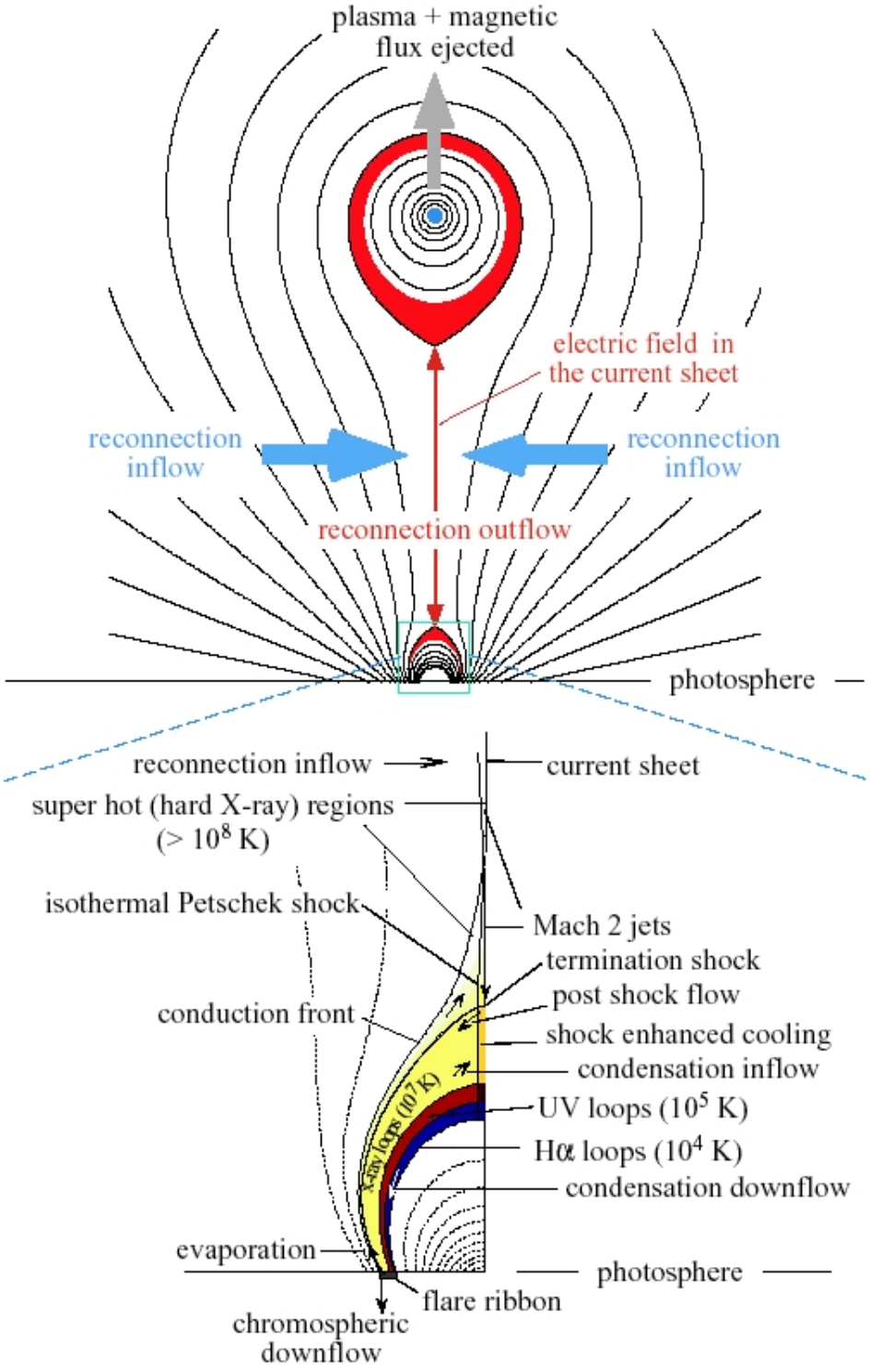

Figure 1.3 The two-dimensional schematic picture of the standard flare model. Source: *Lin & Forbes (2000)*.

The HXR and MW part of this model has been inspired by both the temporal and the spatial observations of the two emissions. As suggested in Figure 1.2, the intensity profiles of the two emissions are commonly known to show a high level of correlation during the first 5-10 minutes of the flare (see also Figure 2.1). Furthermore, it has been observed that their time integral roughly agrees with the SXR time profile (*Neupert effect*; Neupert 1968) for some flares. These observations support the idea that the HXRs and MWs are recording the time scale of the energy release and the resultant particle acceleration processes while the SXRs are recording the accumulating total energy deposited by such processes. In the next two sections, the emission mechanisms for the two emissions will be given, and the examples of their spatial and spectral obvservations, which are used to probe the properties of the flare accelearted electrons, will be provided.

1.2 Flare HXR Emission

1.2.1 Emission Mechanisms

Bremsstrahlung The most common source of flare radiation is produced by bremsstrahlung, when the free electrons in solar plasma interact with the ions and emit photons as they change their paths due to the Coulomb force. This is also called free-free emission since the interacting electron enters and leaves the interaction as a free electron. If the interacting electron gets captured by ion, it is called free-bound emission. The dominant contribution in HXRs (deka-keV range) is free-free emission, and the emitted photons constitute continuum emission.

HXR emission can result only from close binary collisions. In these cases the *differential cross-section* $\sigma_B(\epsilon, E, \Omega)$, which is a cross-section that depends on incident electron energy E, outgoing photon energy ϵ, and outgoing photon direction Ω, become important. A convenient formula is the direction-integrated, non-relativistic, Bethe-Heitler cross-section (Tandberg-Hanssen & Emslie 2009):

$$Q_B(\epsilon, E) = \frac{7.9 \times 10^{-25} \overline{Z^2}}{\epsilon E} \ln \frac{1 + (1 - \epsilon/E)^{1/2}}{1 - (1 - \epsilon/E)^{1/2}} \tag{1.1}$$

where Z, the atomic number of the scattering ions (hydrogen and others), must be considered for the solar atmosphere. The factor $\overline{Z^2}$, the abundance-weighted value of Z^2, is approximately 1.4 for solar conditions (Allen 1973; Emslie et al. 1986).

To make a use of the observed HXR photon emission as a diagnostic tool for probing the high-energy electrons in flares, one must make an assumption of the energy distribution of these electron populations. One is a "thermal population", where the electron population has a Maxwellian distribution of the velocities corresponding to the temperature T. Another one is a "nonthermal population", where the electron population has a non-Maxwellian distribution of the velocities.

Nonthermal Bremsstrahlung The nonthermal population in flares refers to the electrons with a non-Maxwellian energy distribution, accelerated by the energy released in magnetic reconnection. The expression for the photon flux $I(\epsilon)$ (photons cm^{-2} s^{-1} keV^{-1}) observed at the Earth, resulting from the injection of nonthermal electrons with flux density spectrum $F(E, \vec{r})$ electrons cm^{-2} s^{-1} keV^{-1}, at position $\vec{r}$ where the plasma ion density is $n(\vec{r})$ ions cm^{-3} is (Holman et al. 2011):

$$I(\epsilon) = \frac{1}{4\pi R^2} \int_V \int_\epsilon^\infty n(\vec{r}) F(E, \vec{r}) Q_B(\epsilon, E) dE dV, \tag{1.2}$$

where $R = 1\mathrm{AU}$ and V is the emitting source volume.

As the plasma density of the target increases, Coulomb energy loss (scattering) between electrons and electrons increases as well, and this must be taken into the account for the energy spectrum of electrons injected into the source (in solar plasma, the energy transfer between electrons is much faster than between electrons and ions). The loss rate is expressed by (Holman et al. 2011):

$$\frac{dE}{dt} = -(K/E)n_e(\vec{r})v(E), \tag{1.3}$$

where $K \sim 3.00 \times 10^{-18}(\Lambda_{ee}/23)$ keV^2 cm^2, Λ_{ee} is the Coulomb logarithm ($\sim$23 for the solar corona) for electron-electron collisions, $n_e(\vec{r})$ is the plasma electron number density, and $v(E)$ is the speed of the fast electron. This expression can be further simplified with the relation $vdt = dz$, to give

$$\int EdE = -KN_e(z) \tag{1.4}$$

$$N_e(z) = \int_{LOS} n_e(z)dz \text{ cm}^{-2}. \tag{1.5}$$

where $N_e(z)$ is called plasma electron *column density*. The evolution of an electron's energy over a certain column density is then $E^2 = E_0^2 - 2KN_e$, which leaves, for instance, a 10 keV electron to lose all of its energy over a column density of 1.7×10^{19} cm^{-2}, and 50 keV electron to lose all of its energy over a column density of 4.2×10^{20} cm^{-2}.

If these Coulomb energy losses are not significant within a spatially unresolved X-ray source region, the emission is called *thin-target*, while if the beam of nonthermal electrons lose all their suprathermal energy within the spatially unresolved source and become thermalized during the observational integration time, the emission is called *thick-target*. For the thin-target case, Equation. 1.2 can be inverted to obtain the instantaneous effective electron flux density spectrum present in the X-ray emitting region, in electrons per cm^2 per second per keV. For the thick-target case, the photon spectrum observed at the Earth is (Holman et al. 2011):

$$I_{thick}(\epsilon) = \frac{1}{4\pi R^2} \int_{\epsilon}^{\infty} \mathscr{F}_0(E_0)\nu(\epsilon, E_0)dE_0 \tag{1.6}$$

$$\nu(\epsilon, E_0) = \int_{E_0}^{\epsilon} \frac{n(\vec{r})v(E)Q_B(\epsilon, E)dE}{dE/dt},$$

where $\mathscr{F}_0(E_0)$ is the electron beam flux distribution in electrons per second per keV, and ν is the number of photons produced by a single electron of energy E_0. Assuming that an electron is thermalized within the observational integration time, inverting this equation gives us the flux spectrum of the electrons injected to the X-ray emitting region, in electrons per second per keV.

The high-energy part of the observed HXR photon spectra that show a power-law shape (see Figure 1.5 right, above ∼30 keV) can be usually fitted with a single or a double power-law, and for a single power-law, the photon spectrum from the electron flux distribution of the form $\mathscr{F}(E) = AE^{-\delta}$ is also well approximated by the power-law form $I(\epsilon) = I_0\epsilon^{-\gamma}$. The relationship between these two spectral indices for thin- and thick-target model are $\gamma_{thin} = \delta + 1$ and $\gamma_{thick} = \delta - 1$. However, these δ stand for different distribution spaces, *flux density* spectrum ($F(\vec{r}, E)$) for thin-target and *flux* spectrum ($\mathscr{F}(E)$) for thick-target. It is sometimes convenient to transform these into *electron number density* spectrum, $f(\vec{r}, E)$, through the relations $F(\vec{r}, E) = f(\vec{r}, E)v(E)$ for the former and $\mathscr{F}(E) = f(\vec{r}, E)Av(E)$ for the latter, where A is the area of the emitting source that must be obtained from the observation. If we assume that $f(\vec{r}, E) \propto E^{-\delta'}$, then the spectral index relation become $\gamma_{thin} = \delta' + 0.5$ and $\gamma_{thick} = \delta' - 1.5$.

Thermal Bremsstahlung Bremsstrahlung emission from a thermal population is called thermal bremsstrahlung, and for HXRs it typically refers to the population having a sufficiently large temperature, $\sim 10^8$K ($kT \approx \epsilon \approx$10 keV). The low energy

part of the HXR spectrum (below $\sim$ 10 keV in Figure 1.5 right, for example) is usually attributed to this emission. If we assume a population of n_e hot electrons with a Maxwellian distribution corresponding to a tempearture T in a volume V, then its energy distribution function is (Tandberg-Hanssen & Emslie 2009):

$$f_E(E) = \frac{2n_e}{\pi^{1/2}(kT)^{3/2}} E^{1/2} \exp(-E/kT) \text{ electrons cm}^{-3}\text{erg}^{-1} \tag{1.7}$$

The bremsstrahlung produced by the collisions between these electrons with ambient protons (of the same density, n_e) is (Tandberg-Hanssen & Emslie 2009):

$$I(\epsilon) = n_e V \int_\epsilon^\infty f_E(E) v(E) \sigma_B(\epsilon, E) dE$$

$$= D \frac{Q}{\epsilon T^{1/2}} exp(-\epsilon/kT) \tag{1.8}$$

where $D = 5.7 \times 10^{-12} \overline{Z^2} \text{cm}^{-3}\text{s}^{-1}\text{K}^{1/2}$, and $Q = \int n_e dV$ is a quantity called the *emission measure* (EM) of the source. In many cases, it is useful to use *differential emission measure* (DEM), which is applicable to non-isothermal sources (Tandberg-Hanssen & Emslie 2009),

$$Q(T) = n_e^2 dV/dT \tag{1.9}$$

The photon spectral shape of thermal bremsstrahlung emission is also known to depend on the shape of this DEM spectrum. For instance, for the photon spectrum with a power-law shape $I(\epsilon) = a\epsilon^{-\gamma}$, the source DEM spectrum has the form $Q(T) \propto T^{1/2-\gamma}$.

1.2.2 Observational Examples

Flare HXR emission above ∼12 keV from nonthermal bremsstrahlung is almost always observed from the footpoints of the flaring loop (Guo et al. 2012; Jeffrey & Kontar 2013; Masuda et al. 1994; Ishikawa et al. 2011; Torre et al. 2012). Since it is produced in the chromosphere where the plasma density is high, the emission is treated with the thick-target model. HXR emission can also be observed above the flaring loop, although rarely, as the so-called "above-the-loop-top" (ALT) source. The most celebrated example of an ALT source is the one introduced in Masuda et al. (1994), shown in Figure 1.4.

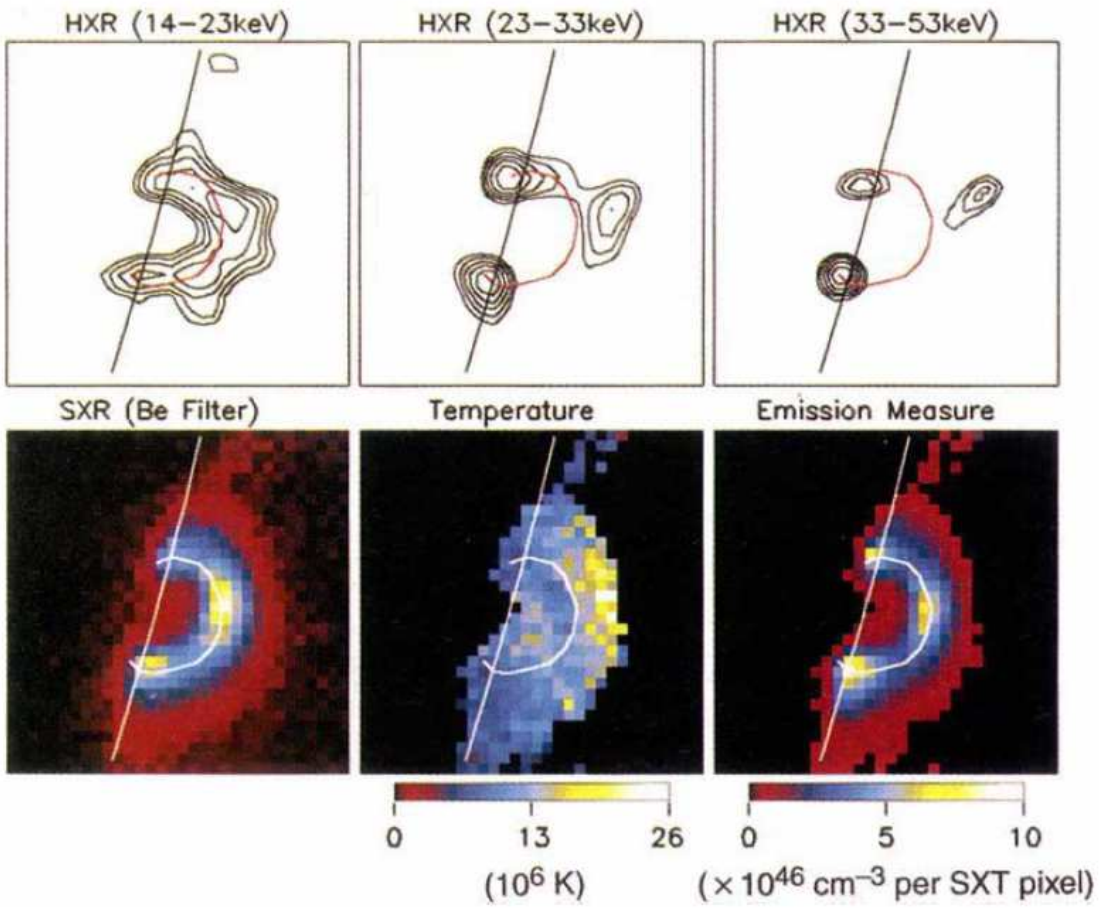

Figure 1.4 HXR (top row) and SXR (bottom row) images of the limb flare on 1992, Jan. 13 observed by Yohkoh satellite. Source: *Masuda et al. (1994)*.

In this study, the authors studied a limb flare, and observed a HXR source located well above the apex of the SXR loop, together with the usual footpoint source (top middle panel). The authors interpret this region as the acceleration region, and the calculation of the electron density in this source and the injected electron rate from the thick-target emission at the footpoint revealed that almost all electrons must be accelerated in the coronal source and stream down to the chromosphere, which requires a highly efficient mechanism for particle acceleration.

Another example of the flare HXR emission is shown in Figure 1.5, taken from Krucker & Battaglia (2014).

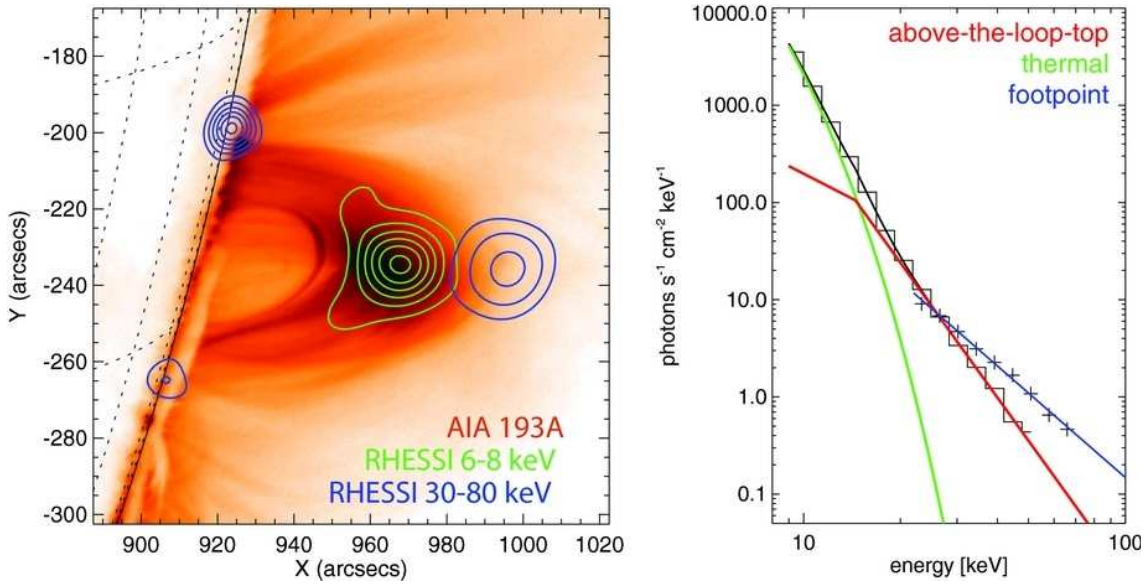

Figure 1.5 Left: HXR (contours) and EUV (background) observation of the limb flare of 2012, July 19. HXR observation was made by the *Reuven Ramaty High Energy Solar Spectroscopic Imager* (*RHESSI*) and EUV observation was made by the *Solar Dynamic Observatory* (*SDO*). Right: Spatially-resolved (between coronal and chromospheric HXR source) HXR photon spectra are obtained from RHESSI imaging spectroscopy. Source: *Krucker & Battaglia (2014)*.

In this study, the emission in the 6-8 keV image is interpreted due to thermal bremsstrahlung, and the corresponding temperature and the emission measure is derived. The 30-80 keV HXR ALT source is interpreted as thin-target nonthermal bremsstrahlung since the column density is assumed to be relatively small in the

higher corona. The instantaneous nonthermal electron density from this source is derived based on the spatially-resolved spectrum obtained from imaging spectroscopy (Figure 1.5, right), and the result also indicated that a bulk acceleration process energizes all electrons in the source.

1.3 Flare MW Emission

1.3.1 Radiative Transfer

An important concept in radio astronomy (which includes MW analysis in its high-frequency end) is the radiative transfer, which can be conceptually understood that the observer on the Earth measures the radiation intensity in terms of the interplay between the emissivity and the absorption coefficient of the source (either by the emitting volume itself or by the volume located closer to the observer), accumulated along the line of sight.

Consider the geometry shown in Figure 1.6, where the radiation from a volume element dV has an associated emissivity η_ν and the absorption coefficient κ_ν, which is the fraction of intensity I absorbed per unit length.

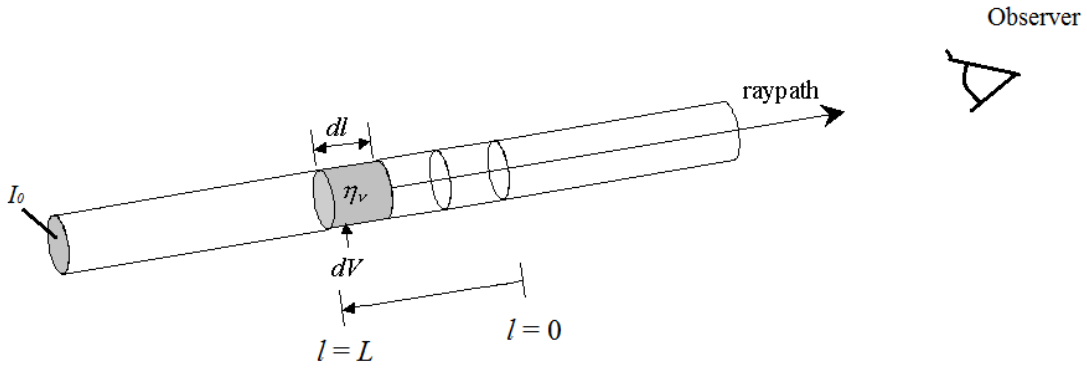

Figure 1.6 The geometry of the radiative transfer equation. Source: *Radio Astronomy Lecture Series, New Jersey Institute of Technology, Physics 728 by Dr. Dale E. Gary (https://web.njit.edu/ gary/728/).*

The incremental intensity dI over dl is then expressed as $dI = \eta_\nu dl - \kappa_\nu I dl$. Rearranging this, one gets the *radiative transfer equation*

$$\frac{dI}{dl} + \kappa_\nu I = \eta_\nu \tag{1.10}$$

The solution of this differential equation, assuming η_ν and κ_ν are both constant over the path, is

$$I = I_0 e^{-\int_0^L \kappa_\nu dl'} + \frac{\eta_\nu}{\kappa_\nu}(1 - e^{-\int_0^L \kappa_\nu dl'}) = I_0 e^{-\tau_\nu} + \frac{\eta_\nu}{\kappa_\nu}(1 - e^{-\tau_\nu}) \tag{1.11}$$

where $\tau_\nu = \int_0^L \kappa_\nu dl'$ is called the *optical depth* or *opacity*, integrated **from** the observer, and is the measure of how many e-foldings of intensity reduction the emission from a certain source (layer) goes through before reaching to the observer.

For a thermal source in radio frequencies, the ratio of η_ν and κ_ν in the second term is conveniently described by the Rayleigh-Jeans limit of the Planck function ($h\nu << kT$), that is

$$\frac{\eta_\nu}{\kappa_\nu} = \frac{2kT}{c^2}\nu^2 \tag{1.12}$$

where k is the Boltzmann constant, c is the speed of light, ν is the observing frequency, and T is the quantity we call the *brightness temperature* from now on. Inserting T_b to all the equivalent intensity term in the Equation. (1.11) gives

$$T_{b,obs} = T_{b0} e^{-\tau_\nu} + T_{b,source}(1 - e^{-\tau_\nu}) \tag{1.13}$$

The observed brightness temperature is the sum of the attenuated "external" emission (the first term) and the internal emission and the absorption of the volume element closer to the observer. The radio emission source is called either *optically-thick* or *optically-thin*, distinguished by the conditions of τ_ν: $\tau_\nu >> 1$ for the former and $\tau_\nu << 1$ for the latter. For each regime, the above equation reduces to

$$T_{b,obs} = T_{b,source} \text{ (optically-thick regime)} \tag{1.14}$$

$$T_{b,obs} = T_{b0}(1 - \tau_\nu) + T_{b,source}\tau_\nu \text{ (optically thin regime)} \tag{1.15}$$

Note that $T_{b,source}$ is the physical temperature of the source if the thermal source is in the optically-thick regime. On the other hand, for a nonthermal source it is an *effective temperature*, $T_{eff} = \langle E \rangle / k$, where $\langle E \rangle$ is the mean energy of the electrons and does not depend on the physical temperature of the source. That is

$$T_{b,obs} = T \text{ (thermal source in optically-thick regime)} \tag{1.16}$$

$$T_{b,obs} = T_{eff} \text{ (nonthermal source in optically-thick regime)} \tag{1.17}$$

$$T_{b,obs} = T_{b0}(1 - \tau_\nu) + T_{eff}\tau_\nu \text{ (nonthermal source in optically-thin regime)} \tag{1.18}$$

The opacity is a function of the observing frequency ν, and the expression of κ_ν (and the corresponding η_ν which can be obtained by the Equation. 1.12) is different for each radio emission mechanism and for thermal and nonthermal energy distribution. Each emission mechanism has its own characteristic brightness temperature spectral shape for both thermal and nonthermal electron energy distributions that shift in certain directions responding to the changes in various relevant physical parameters (see Figure 1.7). This is useful to deduce unknown physical parameters of the emission region from the observed spectrum, when one can assume that the observation is dominated by one emission mechanism and some parameters are known or estimated

from other observations. However, the above derivation assumes that both η_ν and κ_ν are constant along L (a *homogeneous* source). In many cases, a source will be inhomogeneous over the entire LOS composed of multiple such layers, so the observed spectrum may be complicated and cannot be attributed to one set of parameters (and sometimes not to a single emission mechanism). In this case, one must solve the radiative transfer equation (Equation. 1.10) exactly along the LOS using the expressions for η_ν and κ_ν for all possible emission mechanism. Other effects of the medium, such as Razin suppression (Ginzburg & Syrovatskii 1969) and mode coupling (Melrose 1980) should also be taken into account during this integration.

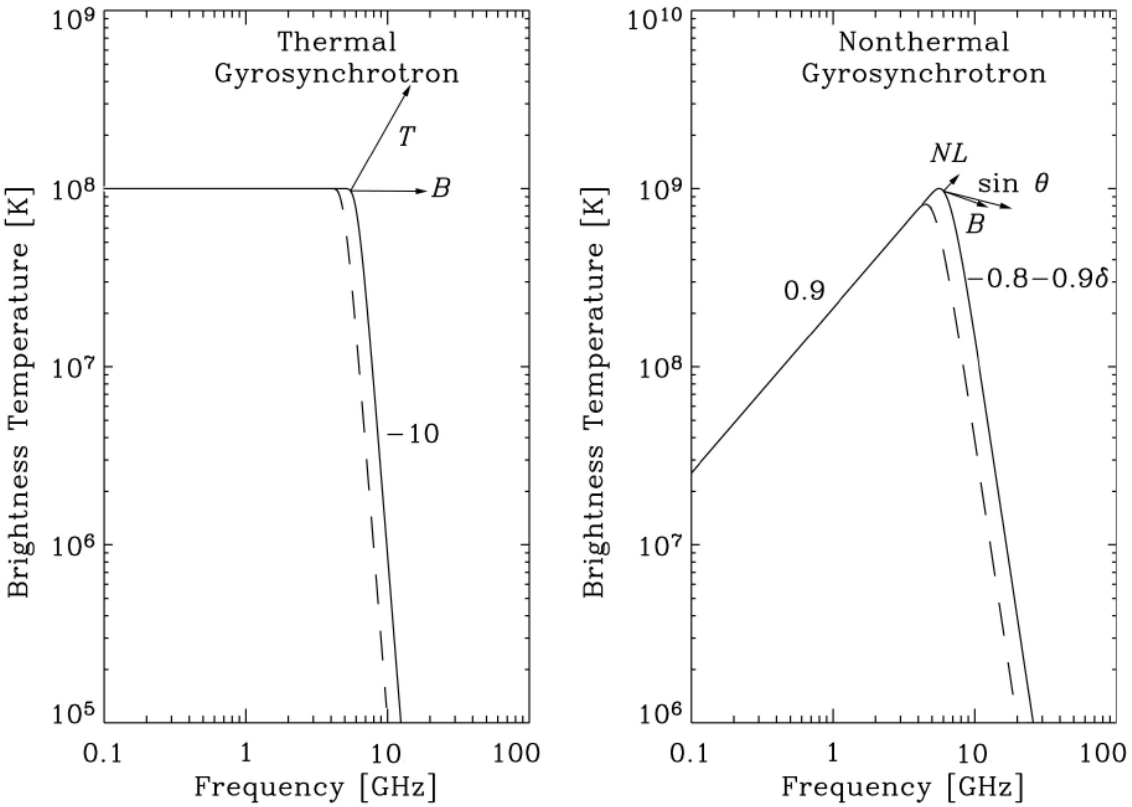

Figure 1.7 The characteristic brightness temperature spectrum for thermal (left) and nonthermal (right) gyrosynchrotron emission, which usually dominates the flare MW emission. The solid and dashed continuum curves correspond to x-mode and o-mode emission, respectively, which usually correspond to right-circular-polarization (RCP) and left-circular- polarization (LCP). Source: *Gary & Keller (2004).*

Lastly, the measured intensity can also be expressed in *flux density*, which is just Equation. 1.12 integrated over the solid angle $d\Omega$,

$$S_\nu = \int \frac{\eta_\nu}{\kappa_\nu} = \frac{2k\nu^2}{c^2} \int T_{b,obs} d\Omega \tag{1.19}$$

where limits of integration differ between the observation of a point (unresolved) source and of a extended source. In the former case, the emission is integrated over the entire source (i.e., total flux density from the source). In the latter case, the emission is integrated only over the beam, of which the size is determined by the observing frequency (wavelength) and the extent of the instrument. Two fundamental quantities used by the radio/MW telescope are *Jansky* (1 Jy = 10^{-26} W m^{-2} Hz^{-1}) and *Solar Flux Unit* (*sfu*, 1 sfu = 10^{-22} W m^{-2} Hz^{-1} = 10,000 Jy).

1.3.2 Emission Mechanisms

Gyroresonance and Gyrosynchrotron radiation The electrons in a magnetized plasma feel the Lorentz force when interacting with the ambient magnetic fields, and emit radiation as they gyrate around the magnetic field lines due to the centripetal acceleration. The fundamental gyrofrequency of an electron, ω_B, depends on the magnetic field B:

$$\omega_B = \frac{eB}{2\pi m_e c} = 2.8 \times 10^6 B \text{ Hz} \tag{1.20}$$

As the energy of the gyrating electron increases, the relativistic effect comes in and the emission starts to beam strongly in the direction of v (velocity of the electron). This asymmetry causes the radiated power to start appearing at harmonics of ω_B, $s\omega_B$, where s is a harmonic number, in the frequency spectrum. For low number of s, the emission is called *gyroresonance* emission, and is more related to thermal population due to the low energy of the electrons. The characteristic T_b spectrum

for thermal gyroresonance emission for 10^6 K corona (plus 10^4 K chromosphere, a "background" optically-thick emission) is shown in Figure 1.8, with the arrows indicating the direction of the shift of the spectrum corresponding to the changes in its relevant physical parameters.

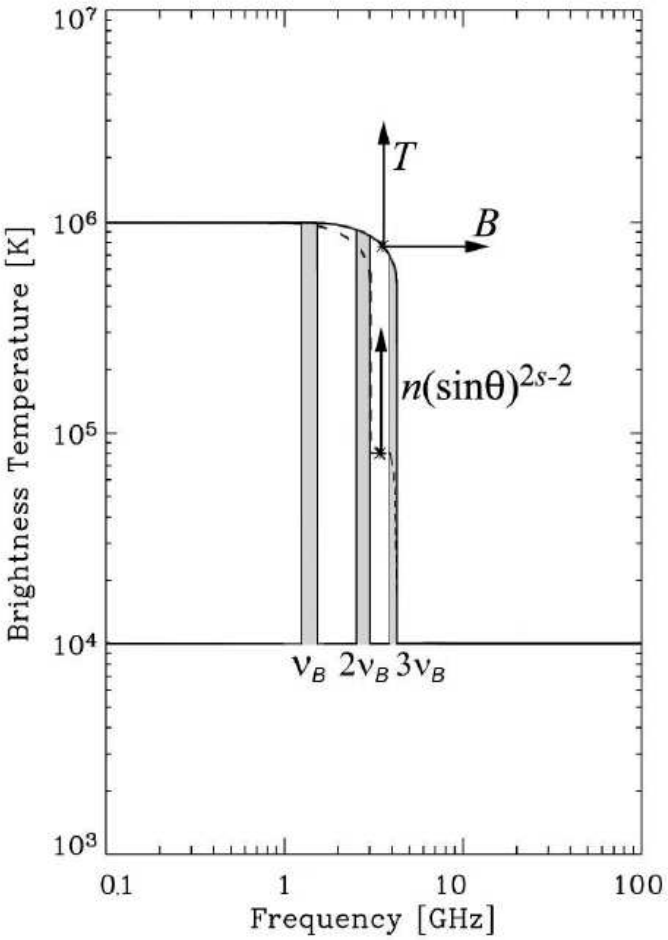

Figure 1.8 The characteristic brightness temperature spectrum for thermal gyroresonance emission. Note that the continuum is the emission from the entire LOS over which the magnetic field strength vary smoothly while discrete lines are the emission from isogauss layer with $B = 500$ G. The solid and dashed continuum curves correspond to x-mode and o-mode emission, respectively. Source: *Gary & Keller (2004).*

For high harmonic numbers ($s = 10 - 100$), at which the electrons are mildly relativistic and thus most likely have a nonthermal distribution (with energies of 100-300 keV), the emission is called *gyrosynchrotron* (GS) emission. GS emission from

a nonthermal power-law electron distribution usually dominates the flare spectrum, and the widely-used, simplified empirical expressions for T_{eff}, η_ν, and κ_ν that are valid over the range $2 \lesssim \delta \lesssim 7$, θ (viewing angle) $\gtrsim 20^o$, $10 \lesssim s \lesssim 100$, and for isotropic pitch-angle distribution are (Dulk 1985):

$$T_{eff} \approx 2.2 \times 10^9 10^{-0.31\delta} (sin\theta)^{-0.36-0.06\delta} s^{0.05+0.085\delta} \tag{1.21}$$

$$\frac{\eta_\nu}{BN} \approx 3.3 \times 10^{-24} 10^{-0.52\delta} (sin\theta)^{-0.43+0.65\delta} s^{1.22-0.90\delta} \tag{1.22}$$

$$\frac{\kappa_\nu B}{N} \approx 1.4 \times 10^{-9} 10^{-0.22\delta} (sin\theta)^{-0.09+0.72\delta} s^{-1.30-0.98\delta} \tag{1.23}$$

where N is the number density of the electrons with energy E. The characteristic spectral shapes for T_b and the corresponding S_ν are shown in Figure 1.9 (second row), along with those for other emission mechanisms.

As can be seen, the optically-thin part of the spectrum can be used to infer δ, using Equation. 1.22. Also, the GS emissivity is sensitive to the polarization of the radiation, such that the degree of circular polarization (right-circular-polarization, RCP, or left-circular-polarization, LCP) can give the information about the angle of the magnetic field line to the LOS. This property is useful in the analysis of the loop morphology in the flaring active regions. However, the anisotropy of the pitch-angle distribution has been found to affect the intensity, local spectral index value, and polarization of optically-thin GS emission (Fleishman & Melnikov 2003). It is also important to note that these expressions are only valid in the medium where thermal particle density is low. If the medium has high thermal particle density, the refractive index becomes less than 1, and thus the GS radiation is supressed within the medium (Razin suppression, Ginzburg & Syrovatskii 1969) and the low-frequency

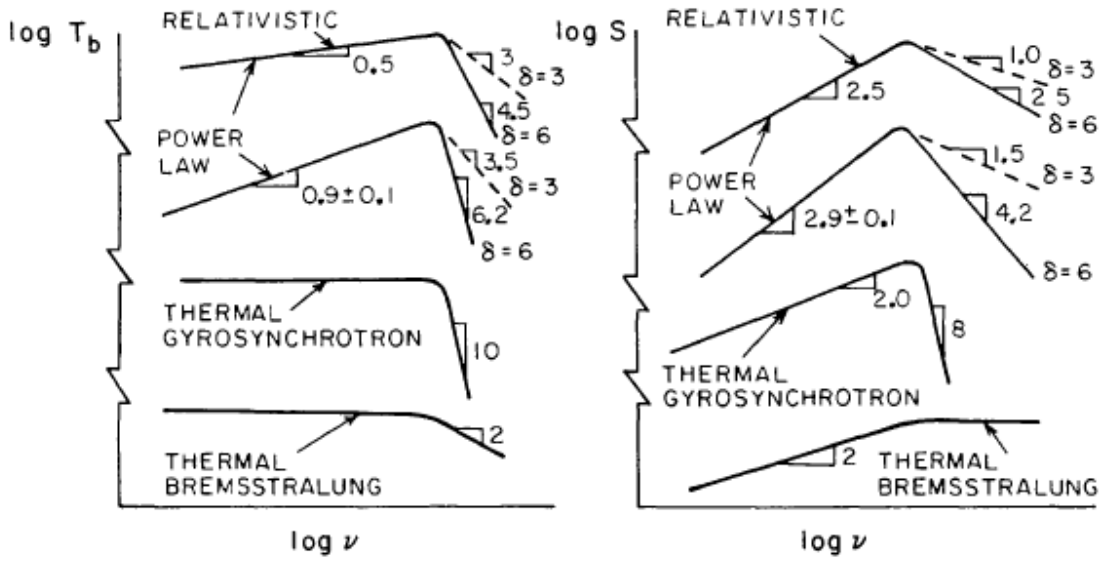

Figure 1.9 Schematic spectra of brightness temperature and flux density for bremsstr-ahlung (bottom) and gyrosynchrotron (top three) radiation. The typical spectral shape for flare emission is the gyrosynchrotron radiation from electrons with power-law spectrum (second from the top). Dashed and solid curve in the optically-thin regime (falling part) correspond to the different spectral index (δ) for the emitting electron spectrum. Source: *Dulk (1985)*.

part of the GS spectrum steepens. Therefore, in many cases where flare morphology and electron energy distribution become complex, these simplified spectral analyses are generally not suitable for detailed quantitative analysis. In the past, use of these simplified approximate expressions was necessitated by the complexity and computational difficulty of using the exact theory. However, recent advances in fast GS codes (Fleishman & Kuznetsov 2010), together with realistic 3D modeling tools (Section 3.3) have superseded use of the approximate expressions except for qualitative understanding.

Thermal Bremsstrahlung Bremsstrahlung from distant collisions between thermal electrons and ions can give rise to MW emission (as opposed to the close-binary collisions for HXRs), although it is in most cases overcome by the stronger GS emission during flares. The emissivity of thermal bremsstrahlung is:

$$\eta_\nu = (\frac{2^6\pi e^6}{3m_e c^3})(\frac{2\pi}{3m_e kT})^{1/2} n_e n_i Z^2 G_{ff}(T,\nu) \tag{1.24}$$

where $G_{ff}(T,\nu)$ is called the Gaunt factor, related to the Coulomb logarithm introduced when discussing HXR (Equation. 1.3), and is given by

$$G_{ff}(T,\nu) = (3^{1/2}/\pi)\ln[\frac{\pi(kT)^{3/2}}{2^{1/2}Ze^2 m_e^{1/2}\nu}]. \tag{1.25}$$

The absorption coefficient of thermal bremsstrahlung is:

$$\kappa_\nu \sim 9.78\times10^{-3}\frac{n_e}{\nu^2 T^{3/2}}\sum_i Z_i^2 n_i \tag{1.26}$$

$$\times\begin{cases} 18.2 + \ln T^{3/2} - \ln\nu \ (T < 2\times10^5 \text{ K}) \\ 24.5 + \ln T - \ln\nu \ (T > 2\times10^5 \text{ K}) \end{cases}$$

.

The characteristic spectral shapes for T_b and S_ν are shown in Figure 1.9.

1.3.3 Observational Examples

A schematic model of nonthermal GS emission (Bastian et al. 1998; Gary et al. 2013) reveals that, at lower frequencies (optically thick regime), the magnetically weak, loop-top source has higher brightness temperature than the magnetically stronger footpoint sources. However, because the loop-top source has a lower peak frequency (the frequency at which $\tau_\nu = 1$) than footpoint sources due to the strength of the magnetic field, the footpoint sources outshine the loop-top source at higher frequencies. In case of an asymmetric loop, the magnetically weaker footpoint reaches its optically thin regime at lower frequency than the magnetically stronger footpoint does, thus the magnetically strong footpoint dominates at higher frequencies.

An example of an observation that matches this picture is shown in Figure 1.10, taken from Lee & Gary (2000). In this figure, the 5 GHz source is the optically-thick GS source and 17 GHz source is the optically-thin GS source. Furthermore, the authors found a strong asymmetry in the magnetic field strengths between two footpoint source locations, which correspond to the asymmetry in the observed MW intensity from the footpoints.

An example of the observation that exploits the power of polarization dependence of the optically-thin nonthermal GS emission is shown in Figure 1.11. In this study, the authors found a gradient in the degree of polarization over one, not fully resolved GS footpoint source. They interpreted this signature as the result of an unresolved magnetic loop rooted in a bipolar magnetic structure, which agreed with the magnetogram observation. The unresolved loop was interpreted as the emerging flux loop that triggered the magnetic reconnection for this flare.

1.4 Scientific Goal and Dissertation Outline

Because of the temporal correlation of the HXR and MW emission and the theoretical background that supports the idea that the electrons with nonthermal energy can give rise to these emission through different mechanisms, there is a common notion in the solar physics research community that a "commmon population" of flare-accelerated electrons produce both HXR and MW emission. However, this idea has to be closely examined since there have been some studies that suggest slight discrepancies between the two observations. The first is the delay between their impulsive peak times; it has been observed that MW peaks often lag HXR peaks (Cornell et al. 1984; Gary & Tang 1985; Silva et al. 2000). The time scale of this delay varies from subsecond to sometimes more than ten seconds. The second is the discrepancies between the HXR-inferred and the MW-inferred electron energy spectral indices (δ); the indices are different generally by $\sim$2 (Kundu et al. 1994; Silva et al. 2000). The third is

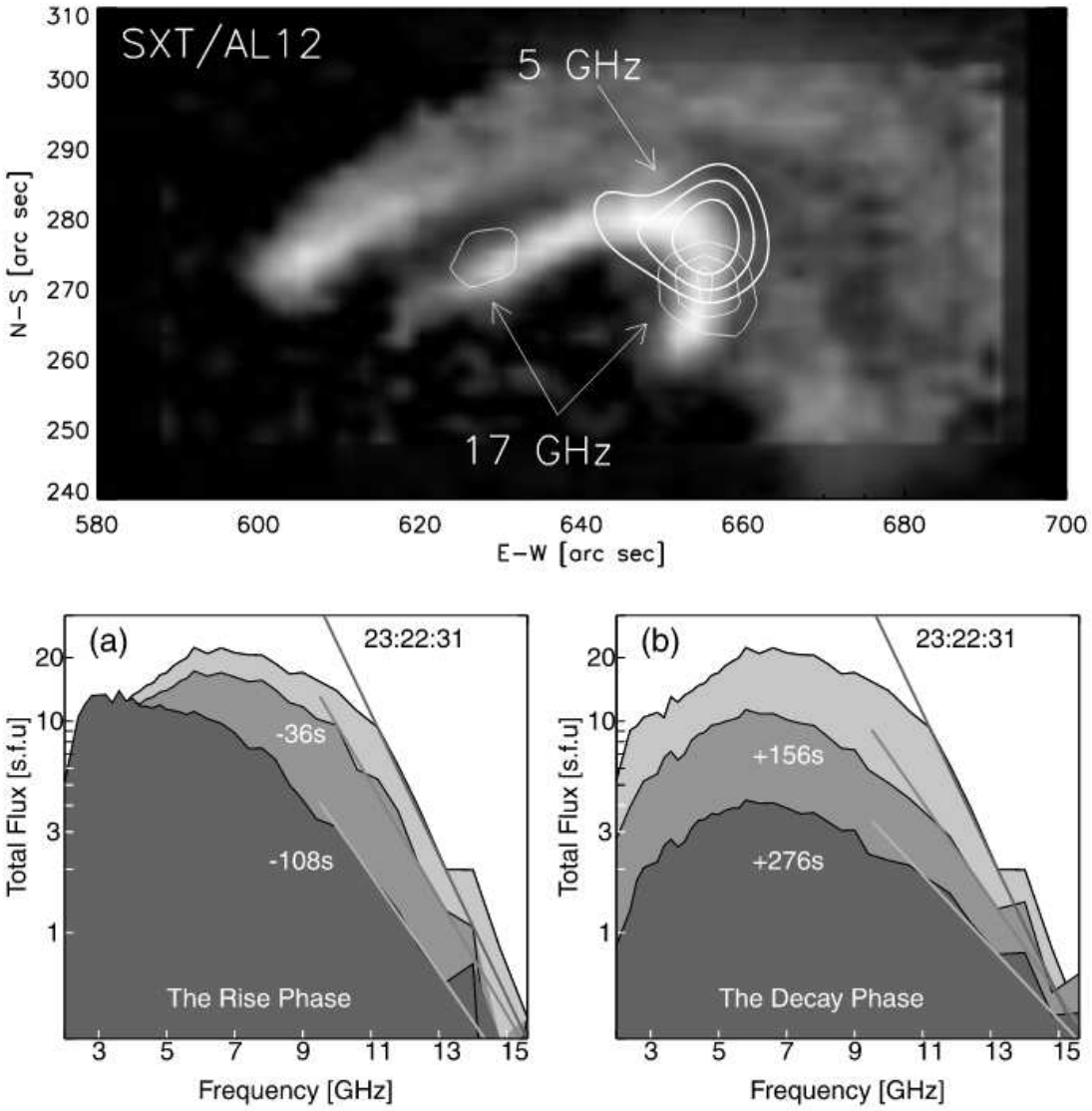

Figure 1.10 MW observation of 1993 June 3 flare from the *Owens Valley Solar Array*. Top: MW 5 GHz and 17 GHz contours on top of the SXR image from *Yohkoh* satellite. Bottom: Spatially-integrated total flux spectra taken at different times of the observation. Source: *Lee & Gary (2000)*.

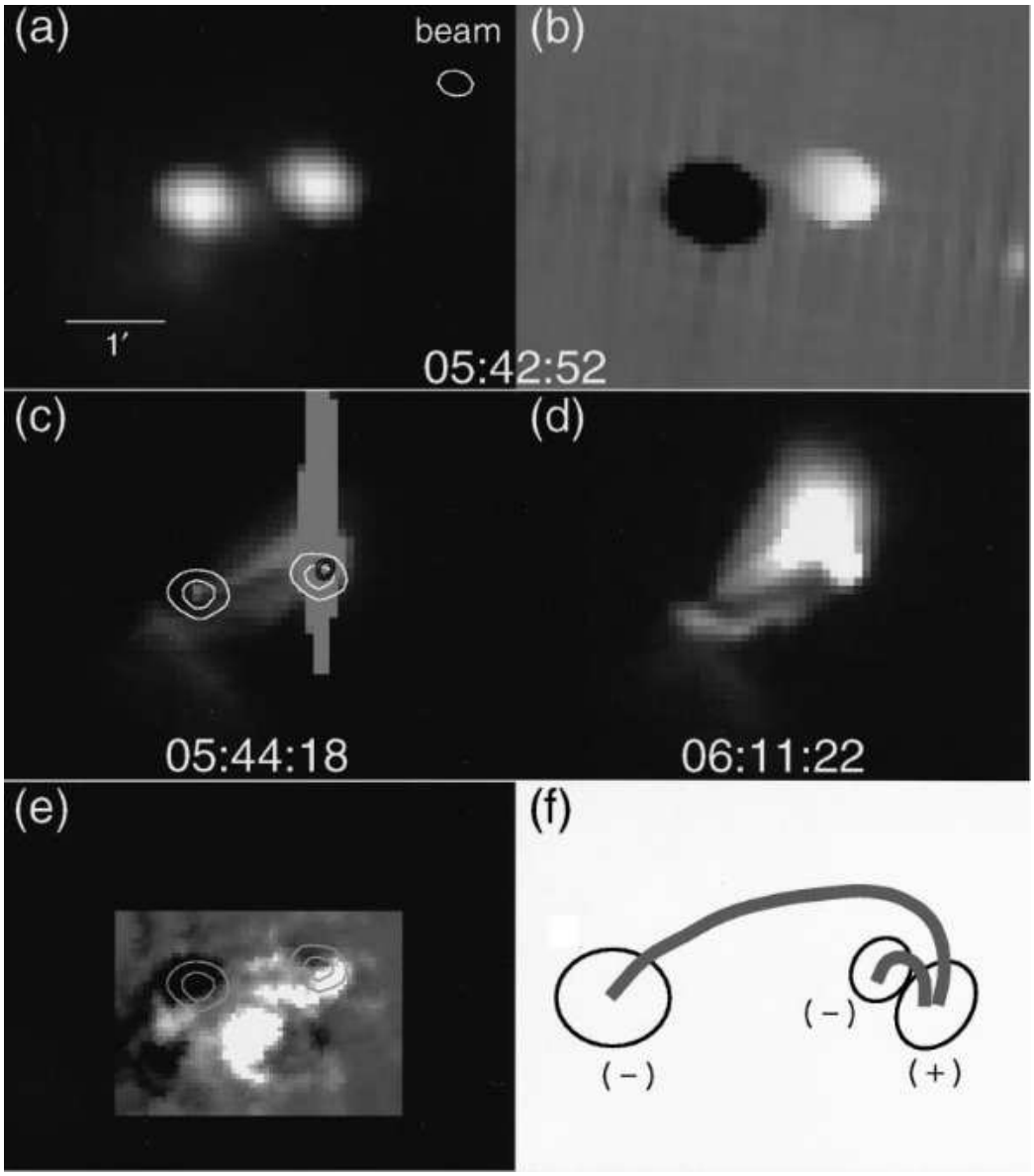

Figure 1.11 Images of C4.1 flare on 1993 June 7. (a-b) Images of the intensity and the degree of polarization ($T_{b,(RCP-LCP)}/T_{b,(RCP+LCP)}$) at 17 GHz from the *Nobeyama Radioheliograph*; black to LCP and white for RCP. (c-d) SXR images taken from *Yohkoh* during the peak and the decay phase of the flare. White contours show the total intensity image and black contours show the HXR image from *Yohkoh*. (e)Magnetogram taken from *Mees Observatory*. (f) Schematic drawing of the magnetic field configuration of this flare. Source: *Hanaoka (1997)*.

the energy range of the HXR-emitting electrons and the MW-emitting electrons; it has been suggested that the former is lower than the latter, and this may be related to the inferred δ discrepancy (Nitta & Kosugi 1986; Takakura 1972; Kundu et al. 1994). And lastly, the source locations and their interpretations between two emissions are slightly different. The MW source variously appears as a loop-top source or a whole-loop structure with enhanced loop-top (Asai et al. 2013; Kushwaha et al. 2014; Kuznetsov & Kontar 2015) at low frequencies, as well as single or double footpoint sources at higher frequencies (Kundu et al. 1982; Asai et al. 2013). These observations are interpreted as the signature of nonthermal electrons trapped within the magnetic flux tube, as opposed to the HXR-emitting electrons which are thought to pass though the magnetic mirror point immediately and then precipitate to the chromosphere in much shorter time scale.

One way to investigate the sources of these discrepancies is to use the high-cadence observation simultaneously made in HXRs and MWs, both temporally and spatially. The problems of the difference in the energy range and spectral index can be investigated by inverting the entire electron energy spectrum from the observations simultaneously made in both HXRs and MWs. However, this has been difficult. One reason for the difficulty is that flares that enable us to invert the observed X-ray photon spectrum to the electron energy spectrum extending above few hundreds of keV are relatively large (e.g., high M- or X-class flares), and large flares complicate the X-ray spectrum inversion because the thermal part of the X-ray spectrum dominates the nonthermal part at lower energies, sometimes up to 30 keV or higher. Another reason is that, for MW, inverting the electron energy spectrum from the observed MW spectrum is oversimplified for quantitative analysis.

The aim of this work, presented in the following two chapters, is to find the relationship between HXR-emitting and MW-emitting electron population in finer details through multi-wavelength analysis enabled by the combination of high-

resolving space-borne and ground-based observatories, and offer the possible solutions to those discrepancy problems. Chapter 2 is an observational study that explores the time delays, source locations, spectral indices, and their temporal evolution of the HXR and MW emissions during the impulsive phase of the well-observed X2.2 flare of 2011, Feb. 15. Chapter 3 is a simulation study that addresses some of the discrepancies mentioned above through realistic, three-dimensional, forward-fit modeling of the HXR and MW emission at one time just after the impulsive phase of the well-observed 2015, Jun. 22 M.5 flare. The constraint of the MW part of the model is provided by the prototype data from the observatory that is designed to emphasize imaging spectroscopic capability in the 1-18 GHz MW range, *the Extended Owens Valley Solar Array* (*EOVSA*, currently being commissioned). Chapter 4 gives the conclusions and discussions from this study, as well as some ideas for future work.

1.5 Instruments and Research Tools

In this section, we will briefly introduce the high-resolution instruments and realistic modeling tool that were essential in carrying this work.

The Reuven Ramaty High Energy Solar Spectroscopic Imager (RHESSI): RHESSI (Lin et al. 2002) is the space telescope designed to perform imaging and spectral observations of solar flares from SXR ($\sim$ few keV) to gamma-rays (up to $\sim$ 20 MeV), with angular resolutions as fine as 2 arcseconds, a spectral resolution of $\sim$1 keV, and a temporal cadence of typically 4 s (the spacecraft rotation period). Finer temporal resolution can be obtained through the use of demodulation code hsi_demodulator.pro of the SSW software (Arzner 2004; Qiu et al. 2012). Images can be reconstructed by CLEAN, Maximum Entropy Methods (MEM), Forward-Fitting, or PIXON methods, choosing time, energy range, and a combination of collimators (1 to 9). The spectral analysis can be done by using the Object Spectral Executive (OSPEX) software (Schwartz et al. 2002), which can perform the deconvolution of

the observed photon-count spectrum with known response function to deduce the true photon spectrum from the Sun, and the spectral-fitting using many pre-defined functions that represent emission from various particle energy distribution.

***The Nobeyama Radio Polarimeters* (*NoRP*) and *The Nobeyama Radioheliograph* (*NoRH*)**: Nobeyama Radio Observatory (NoRO; Nakajima et al. 1985, 1994) is the solar-dedicated radio-telescope located in Japan, continuously observing the Sun for about eight hours (22:30 - 6:30 UT) everyday. NoRP records the total incoming flux from the Sun in 1, 2, 3.75, 9.4, 17, 35, and 80 GHz with the temporal cadence of 0.1 s. NoRH produces the full-disk images of the Sun in 17 and 34 GHz total flux intensity (Stokes I) with a cell size of 10 arcsec/pixel and 5 arcsec/pixel, respectively. The 17 GHz observation is also made in circular-polarization (Stokes V). The time cadence is 1 s for normal mode and 0.1 s for event mode.

***The Expanded Owens Valley Solar Array* (*EOVSA*)**: EOVSA (Nita et al. 2016) is the newly expanded and upgraded solar-dedicated radio array (formerly known as *OVSA*, (*Owens Valley Solar Array*; Gary & Hurford 1990) that is currently being commissioned to have the unprecedented imaging spectroscopic capability in MW (2.5-18 GHz) at more than 300 frequency channels with the spatial resolution of 60 arcsec/GHz (finest $\sim$3.3 arcsec at 18 GHz), 1-s time cadence, and four polarizations. EOVSA has been taking total flux density measurements since October 2014, and the cross-correlated amplitude measurements, which can be used to calculate the relative visibility of the source, since June 2015.

***The Solar Dynamic Observatory* (*SDO*)**: The SDO (Pesnell et al. 2012) is a space-borne solar telescope with three onboard instruments: *The Atmospheric Imaging Assembly* (*AIA*; Lemen et al. 2012), *the Helioseismic and Magnetic Imager* (*HMI*; Schou et al. 2012), and *the Extreme Ultraviolet Variability Experiment* (*EVE*; Woods et al. 2012). The AIA observes the full-disk solar atmosphere in 10 different energy channels from white-light continuum (photosphere) to Fe VIII line (coronal

flaring regions). Its temporal cadence is 10 to 12 seconds and the spatial resolution is 1 arcsec. The HMI provides the line-of-sight component and the vector magnetogram of the photosphere every 45 seconds (LOS) and 720 seconds (vector magnetogram). The spatial resolution is 1 arcsec/pixel. The EVE obtains EUV spectra of the full-disk Sun at a spectral resolution of $\sim 1\mathring{A}$ and a cadence of 10 s.

GX Simulator: The *GX Simulator* (Nita et al. 2015) is an IDL-based, three-dimensional graphical-user-interface (GUI) platform that allows its users to (1) import a photospheric magnetic field map and extrapolate it to generate a 3D magnetic field model, or alternately import an externally-defined 3D magnetic field model, (2) investigate the magnetic field topology of the 3D model and create a desired magnetic flux tube on which the user will be performing the multi-wavelength (HXR, MW, and EUV as of this writing) emission calculation, (3) populate the magnetic flux tube with thermal and nonthermal populations of electrons with spectral parameters defined by the user, (4) generate 2D images and spectra through calculations using the internal codes, and (5) compare simulated images and spectra with the observed images and spectra. The details of its internal codes in HXR and MW range are discussed in Section 3.3.

Non-Linear Force Free Field (NLFFF) Extrapolation: NLFFF extrapolation is one kind of realistic coronal field extrapolation assuming the low plasma β (the ratio of the plasma pressure to the magnetic pressure) for the upper chromosphere and lower corona. In this case, the Lorentz force vanishes ($\vec{j} \times \vec{B} = 0$), and the force-free magnetic field is characterized by the condition where the electric currents are parallel to the magnetic field lines, i.e.,

$$\bigtriangledown \times \vec{B} = \alpha \vec{B} \tag{1.27}$$

$$\bigtriangledown \cdot \vec{B} = 0 \tag{1.28}$$

The NLFF case is where we treat the parameter α not constant for all field lines, as opposed to the LFF case where α is constant. The case where $\alpha = 0$ (current-free) corresponds to the potential field extrapolation. The NLFFF extrapolation model is shown to agree with measured fields in a newly developed active region better than the LFF or potential field extrapolation model (Wiegelmann et al. 2005). The extrapolation from the measured photospheric data requires pre-processings (since the photosphere is not truly force-free), which is briefly described in Section 3.2.1.

CHAPTER 2

OBSERVATION OF THE 2011-02-15 X2.2 FLARE IN THE HARD X-RAY AND MICROWAVE

Previous studies have shown that the energy release mechanism of some solar flares follow the Standard magnetic-reconnection model, but the detailed properties of high-energy electrons produced in the flare are still not well understood. We conducted a unique, multi-wavelength study [1] that discloses the spatial, temporal and energy distributions of the accelerated electrons in the X2.2 solar flare on 2011 February 15. We studied the source locations of seven distinct temporal peaks observed in HXR and MW light curves using the RHESSI in 50-75 keV channels and Nobeyama Radioheliograph in 34 GHz, respectively. In addition, we studied the polarization properties of MW sources, and time delay between HXR and MW.

2.1 Introduction

In the study of solar flares, a widely accepted model of the physical mechanism of flares is the Standard magnetic reconnection, referred to as the "CSHKP" model, which assumes magnetic reconnection as the principle mechanism responsible for accelerating flare particles (Hudson 2011). In this model, magnetic reconnection occurs somewhere above the magnetic loop structure of the active region. The form of this magnetic reconnection mechanism is currently not fully understood, although hypotheses such as a large-scale or a collection of small-scale DC electric fields (Dreicer fields) have been suggested (Litvinenko 1996). Magnetic reconnection gives considerable energy to the particles that are present at the reconnection site, in some cases accelerating them to the relativistic regime.

[1] This chapter is based on the following paper: Kuroda, N., Wang, H., & Gary, D. E., "Observation of the 2011-02-15 X2.2 Flare in the Hard X-Ray and Microwave", *The Astrophysical Journal*, vol. 807, pp. 124, 2015.

The dynamics of these accelerated particles after leaving the reconnection site is still not well understood. However, one key observation is that, among the many wavelengths at which flare energy is emitted, HXR and MW emissions show time profiles that are very well-correlated during the impulsive phase of the flare (e.g., Kundu et al. 1982; Cornell et al. 1984; Asai et al. 2013). This observational fact has led many to the conclusion that the same population of electrons is responsible for producing HXR and MW emission, and many studies have been done on various aspects of this behavior. Kundu et al. (1982) analyzed the dynamics of 1980 Jun 25 flare using MW time profile, MW images, and HXR time profile. Cornell et al. (1984) investigated the causes of the time delay between corresponding HXR and MW peaks, and Asai et al. (2013) studied several flares that had corresponding HXR and MW time profiles in terms of electron spectral indices.

One of the interesting topics related to this correlation, and which will be discussed in this chapter, is the delay between their peak times. It has been observed that MW peaks often lag HXR peaks. The time scale of this delay varies from subsecond to sometimes more than ten seconds. Cornell et al. (1984) discussed that the delay observed in their study (an average of 0.2 s) can be explained by the existence of two components of energetic electrons: a prompt component that immediately escapes from the acceleration region, and a delayed component that first undergoes pitch-angle scattering and thus is less impulsive. They discussed that the first component would be the population which produces HXR and the second component would be the population which produces MW, and therefore MW peaks lag HXR peaks. Gary & Tang (1985) studied a single-peaked event in HXR and MW, and found that the delay they found can be explained simply by the difference in decay time of HXR and MW emission (Gary & Tang 1985). They claimed that the two emission processes share the same acceleration profile, but not necessarily the same population; MW-emitting electrons are those that are trapped within the magnetic

fields (because of magnetic mirroring), where the HXR-emitting electrons are those that directly hit the chromosphere. The MW emission has longer decay time than HXR emission because of prolonged trapping, which accounts for the observed delay in the MW peak. Silva et al. (2000) conducted a statistical study of 57 simultaneous peaks of HXR and MW, and found that most probable delay time to be $2 - 4$ seconds, and that the delay time decreased as the HXR energy increased, which supports the hypothesis that the MW-emitting electrons are the higher-energy counterpart of the HXR-emitting electrons. However, they also found that the electron energy spectral index for MW is harder than that for HXR by $0.5 - 2.0$ on average for 75% of the bursts, which was interpreted as due to an upward break in the energy spectrum of the accelerated electrons responsible for HXR and MW emission. They give three hypotheses that could account for their results, (1) HXR- and MW-emitting electrons are different populations that are accelerated by different means at different sites, (2) MW-emitting electrons are accelerated by second-step acceleration, or (3) accelerated electrons follow so-called "trap-plus-precipitation" model, which explains that some of the accelerated particles that get trapped, and give off MW emission, eventually "precipitate out" due to Coulomb collisions, and become those that hit the chromosphere and give off delayed HXR emission (Melrose & Brown 1976). This same model was used by Aschwanden et al. (1995) to study two different components of HXR emission.

In terms of the relative locations of HXR and MW emission, HXR emission can come from loop-top (above-the-loop) and/or footpoint sources, and for MW it can come from either a combination of loop-top and loop-legs or from footpoint sources, depending on the MW frequency. For HXR energies above ~ 12 keV, the emission comes from loop-top and/or footpoint sources (Guo et al. 2012; Jeffrey & Kontar 2013; Masuda et al. 1994; Ishikawa et al. 2011; Torre et al. 2012). Loop-top sources observed at this energy range have been considered as evidence for the particle

acceleration region. They can sometimes be observed simultaneously with footpoint sources (Ishikawa et al. 2011; Kuznetsov & Kontar 2015). For example, Kuznetsov & Kontar (2015) analyzed the spatial properties of the 2004, May 21 flare, and found a loop-top source in 12 – 25 keV range, a loop-top source with footpoint sources in 25 – 50 keV range, and only footpoint sources in 50 – 100 keV range. Above $\sim$ 50 keV, footpoint sources start to clearly dominate. For MW in the range 3 GHz $\sim$ 30 GHz, the dominant emission mechanism in a flare is gyrosynchrotron radiation produced by electrons with mildly relativistic energy distribution. A schematic model of such emission (Bastian et al. 1998; Gary et al. 2013) reveals that, at lower frequencies (optically thick regime), the magnetically weak, loop-top source has higher brightness temperature than the magnetically stronger footpoint sources. However, because the loop-top source has a lower peak frequency than footpoint sources and the brightness temperature of the loop-top source falls off more steeply than that of footpoint sources in the optically thin regime, the footpoint sources have higher brightness temperature than the loop-top source at higher frequencies. In case of an asymmetric loop, the magnetically weaker footpoint reaches its optically thin regime at lower frequency than the magnetically stronger footpoint does, thus the magnetically strong footpoint dominates at higher frequencies. Such is indeed observed: the MW source variously appears as a loop-top source or a whole-loop structure with enhanced loop-top (Asai et al. 2013; Kushwaha et al. 2014; Kuznetsov & Kontar 2015) at low frequencies, as well as single or double footpoint sources at higher frequencies (Kundu et al. 1982; Asai et al. 2013). MW footpoint sources usually match or tend to be spatially very close to HXR footpoint sources in near-disk-center flares. However, this is not the case for near-limb flares, since MW and HXR emissions are produced at different heights (MW emission is produced at the magnetic mirroring point, which is above chromosphere). Also, Sakao et al. (1996) found that, in double footpoint configuration with asymmetrical magnetic strength, stronger HXR emission tends

to originate from the weaker magnetic footpoint (Sakao et al. 1996). They argue that the magnetically stronger side of the loop has stronger magnetic mirroring, thus allowing fewer energetic particles to penetrate, producing weaker HXR emission. Since stronger MW footpoint emission comes from magnetically stronger footpoint as mentioned before, this may result in the discrepancy between HXR and MW emission source location in some cases.

In this study, we analyzed the impulsive phase of the X2.2 solar flare that occurred on 2011, February 15, which showed correlated HXR and MW time profiles. This event has received considerable attention in the literature (Zharkov et al. 2013; Kerr & Fletcher 2014; Milligan et al. 2014; Inoue et al. 2014; Wang et al. 2014) because it was the first X-class flare of the current Solar cycle and was successfully covered by many different instruments. Summarizing these studies, Zharkov et al. (2013) analyzed the seismic/sunquake response, Kerr & Fletcher (2014) analyzed the white-light emission, Milligan et al. (2014) calculated the total energy radiated by the lower solar atmosphere (optical, ultra-violet, and extreme ultra-violet wavelength) and that of the non-thermal electrons derived from HXR. Wang et al. (2014) analyzed flow motion and sunspot rotation of the active region during the impulsive phase. Inoue et al. (2014) performed a magnetohydrodynamic simulation based on non-linear force-free field for the active region responsible for this flare. This paper focuses on the study of flare accelerated electrons, and we do so by observing the flare in HXR and MW in high-temporal (sub-second) and spatial (one to few arcsec) resolutions. To our knowledge, this is the first time the high-resolution comparison between HXR and MW emission of this flare was drawn. We observed that this flare consisted of several temporally distinct peaks in HXR and MW, and we spatially resolved them to see if they were coming from the same or different sources.

In Section 2.2 we list the sources of data we used for the study. In Section 2.3 we describe the analysis in terms of energy/frequency-dependent time profiles and

images. We give the results of the analysis in Section 2.4, and conclude in Section 2.5.

2.2 Data

The X2.2 flare occurred on Feb. 15, 2011, starting from approximately 0130 UT and ending at about 0700 UT, from the active region 11158 located at about S21W28. We used data from the RHESSI for HXR observation and NoRP and NoRH for MW observation. The instrument uses the solar disk for determining absolute position and brightness scale, assuming that the solar disk has a uniform brightness temperature of 10^4 K at 17 GHz. However, during bright solar flares such as this one, the solar disk may be relatively too weak for a precise determination of absolute position, and the source positions can display a jitter of roughly 5 arcsec. We discuss this further in Section 2.4.2. The temporal cadence we used is 0.1 second and 1 second for NoRP and NoRH, respectively. We also used data from the AIA on board the SDO for extreme ultraviolet observation, and magnetogram data obtained from the HMI on board the SDO.

2.3 Analysis

To investigate the properties of flare accelerated electrons, we analyzed the temporal and spatial profiles of the impulsive phase of the flare using instruments listed above. As will be shown, the impulsive phase of this flare (about 10 minutes) consisted of several temporally distinct peaks in HXR and MW. Each peak, according to the standard magnetic reconnection model, comes from a temporally distinct magnetic reconnection event which produces highly accelerated electrons. The aim of this study is to spatially resolve these temporal peaks, in both HXR and MW, to find if they were coming from different or the same source locations. We also compare their locations against extreme ultraviolet and magnetogram images. We investigate time

delays between HXR and MW peaks, and examine their relationship to the spatial and temporal analysis results.

2.3.1 HXR and MW Time Profile

RHESSI successfully covered the entire period of the impulsive phase of this flare, which is from about 0148 UT to 0158 UT. We plot the HXR lightcurve during this period in 50 – 75 keV energy channels. The time profile is shown as a black curve in Figure 2.1. In order to accomplish the highest temporal resolution, we utilize demodulating code as described in Qiu et al. (2012), and reduced its default cadence to 0.2 – 0.3 seconds.

The NoRP and NoRH successfully observed the entire period of this flare. The time profiles in these frequencies are plotted in Figure 2.2. In this flare, the MW time profiles for 9.4 GHz and 17 GHz showed the best correlation with the 50 – 75 keV HXR time profile. The time profiles for MW at 9.4 GHz and 17 GHz during impulsive phase are shown as the red and blue curve, respectively, in Figure 2.1. Note that 17 GHz flux is artificially increased by 500 SFU, to be on the same plotting window as the 9.4 GHz curve.

We chose HXR peaks that were sufficiently distinct and had correlating MW peaks, and calculated the peak times. Those peaks are marked with short grey, red, and blue lines for HXR, MW 9.4 GHz, and MW 17 GHz, respectively, in Figure 2.1. To calculate the peak time, we fitted a third-degree polynomial over a certain data range that includes a visually distinguishable spike in the target peak, and chose several other ranges to obtain several peak times, from which their median was taken as the peak time and their standard deviation was taken as the peak time uncertainties. The peak times and their uncertainties for each frequency are summarized in Table 2.1.

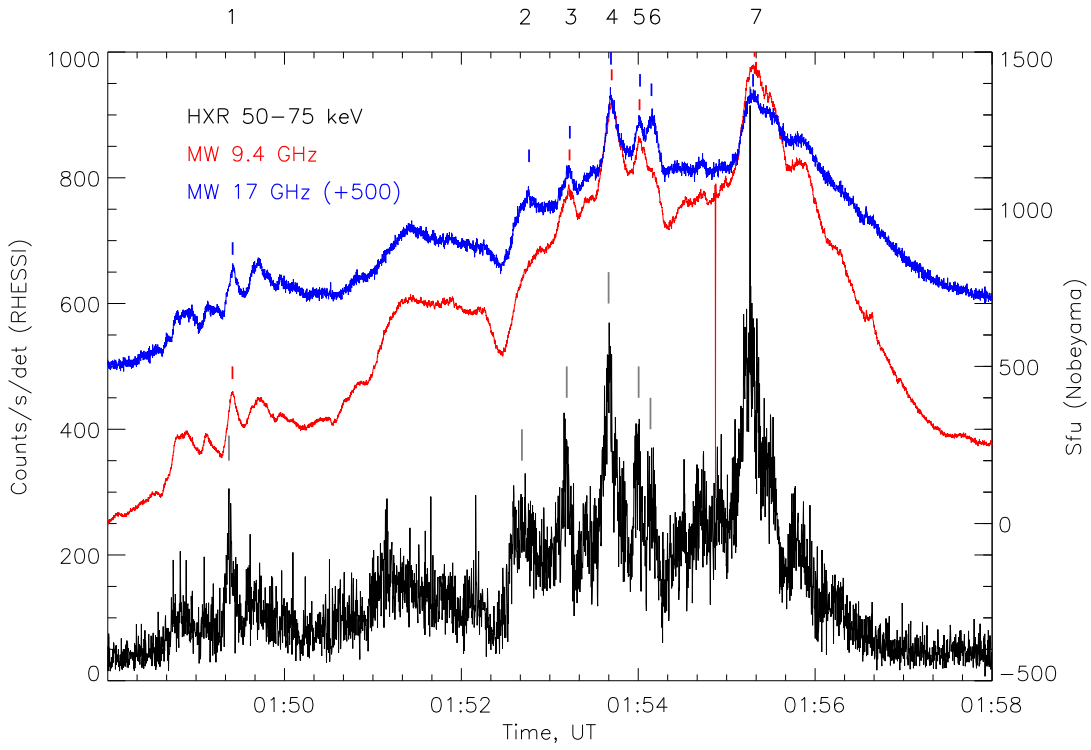

Figure 2.1 HXR 50 – 75 keV, MW 9.4 GHz, and MW 17 GHz time profile from 01:48:00 to 01:58:00. HXR cadence is 0.2 to 0.3 second and MW cadence is 0.1 second. Grey, red, and blue short lines indicate the HXR, MW 9.4 GHz, and MW 17 GHz peaks, respectively, which we identified and calculated the peak times. Note that we only chose combinations of peaks that were distinct enough to calculate the peak times, and MW 17 GHz flux is artificially increased by 500 SFU in order for it to be on the same plotting window as the 9.4 GHz curve.

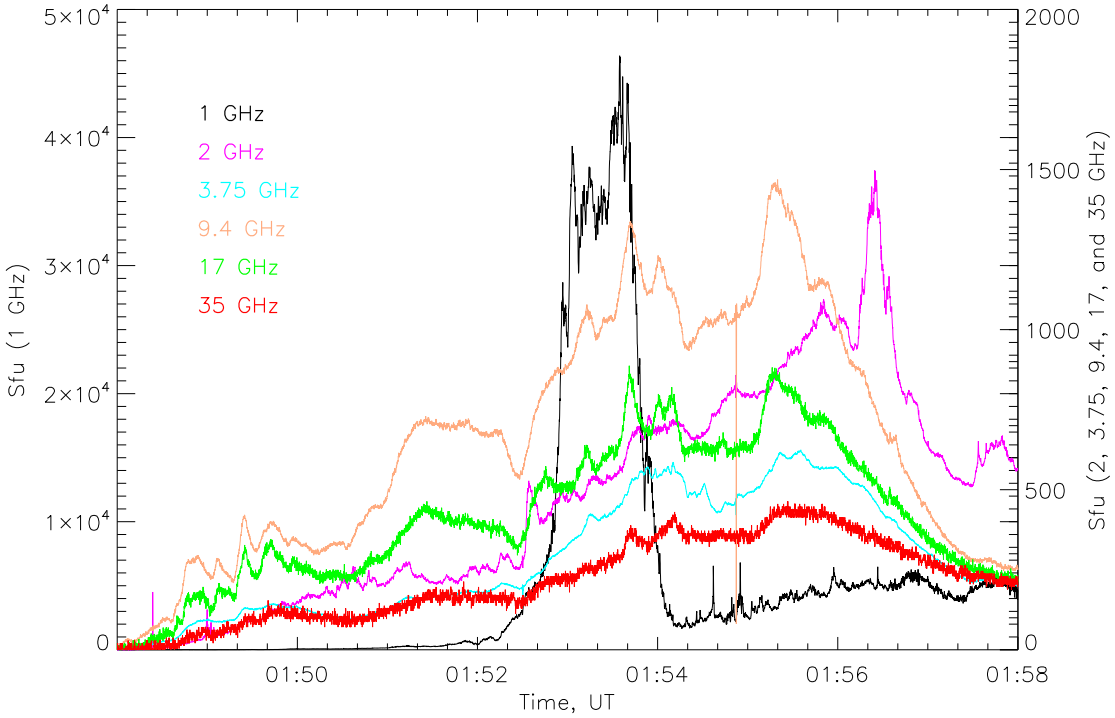

Figure 2.2 NoRP time profiles from 01:48:00 to 01:58:00 in 1, 2, 3.75, 9.4, 17, and 35 GHz frequencies. All are background subtracted. Note that the Y-axis' scale for 1 GHz is different from the Y-axis' scale for 2, 3.75, 9.4, 17, and 35 GHz.

Table 2.1 HXR Peak Times and MW Delay Times (and Their Uncertainties). The Unit is Second.

Peak number	**HXR 50-75 keV**	**MW 9.4 GHz delay time**	**MW 17 GHz delay time**
1	01:49:22.3 (0.127)	2.4 (0.48)	2.5 (0.53)
2	01:52:41.1 (0.210)	N/A (N/A)	4.8 (0.25)
3	01:53:11.5 (0.177)	1.9 (0.80)	2.1 (0.90)
4	01:53:39.9 (0.357	2.1 (0.72)	1.6 (0.69)
5	01:54:00.3 (0.196)	0.6 (0.55)	0.9 (0.53)
6	01:54:08.3 (0.638)	N/A (N/A)	0.7 (0.91)
7	01:55:15.9 (0.247)	3.0 (0.73)	2.0 (0.66)

2.3.2 HXR and MW Imaging

We next analyzed the spatial locations of these peak emissions. For HXR, we utilized RHESSI OSPEX software prepared by the RHESSI team. We used the PIXON algorithm in the 50 – 75 keV energy range, with 1 arcsec resolution, using the front segments of detectors 1 and 3 – 8 with 7 – 36 seconds integration time. We determined appropriate integration times for each peak based on the shape of the lightcurve; we chose intervals during which lightcurves showed single and clear rise-and-fall behaviors. We also identified MW emission sources, obtaining images from NoRH in 17 GHz and 34 GHz, in stokes I, at peak times in the 17 GHz time profile. The images in 34 GHz were synthesized by the readily available Hanaoka program (Hanaoka et al. 1994) from the Nobeyama Observatory. We overplotted HXR and MW energy contours for each peak separately on the HMI continuum image at 01:47UT, and they are shown in Figures 2.3 and 2.4. We also overplotted HXR and MW 34 GHz contours on the EUV images from AIA HeII 304 channel, which usually show flare ribbons, and they are shown in Figure 2.5. Note that AIA images for peak 3 and 4, and peak 5 and 6 are identical because we chose minimally saturated images at the time closest to HXR peak time, and images between these peaks were much more saturated.

2.4 Observational Results

2.4.1 HXR Emission Sources

In HXR, most emission sources were identified to be footpoint sources. The energy range that we used, 50 – 75 keV, is well within the non-thermal electron energy range that is known to show footpoint sources in the thick-target model (Saint-Hilaire et al. 2010). In Figure 2.3, they can all be seen as double sources over the polarity inversion line as well. Their locations all coincide with flare ribbons seen in AIA He 304 in Figure 2.5, which further supports that they are the footpoints of magnetic loops. For peak 1, the type of the source is uncertain. Since it is a single source, it could be

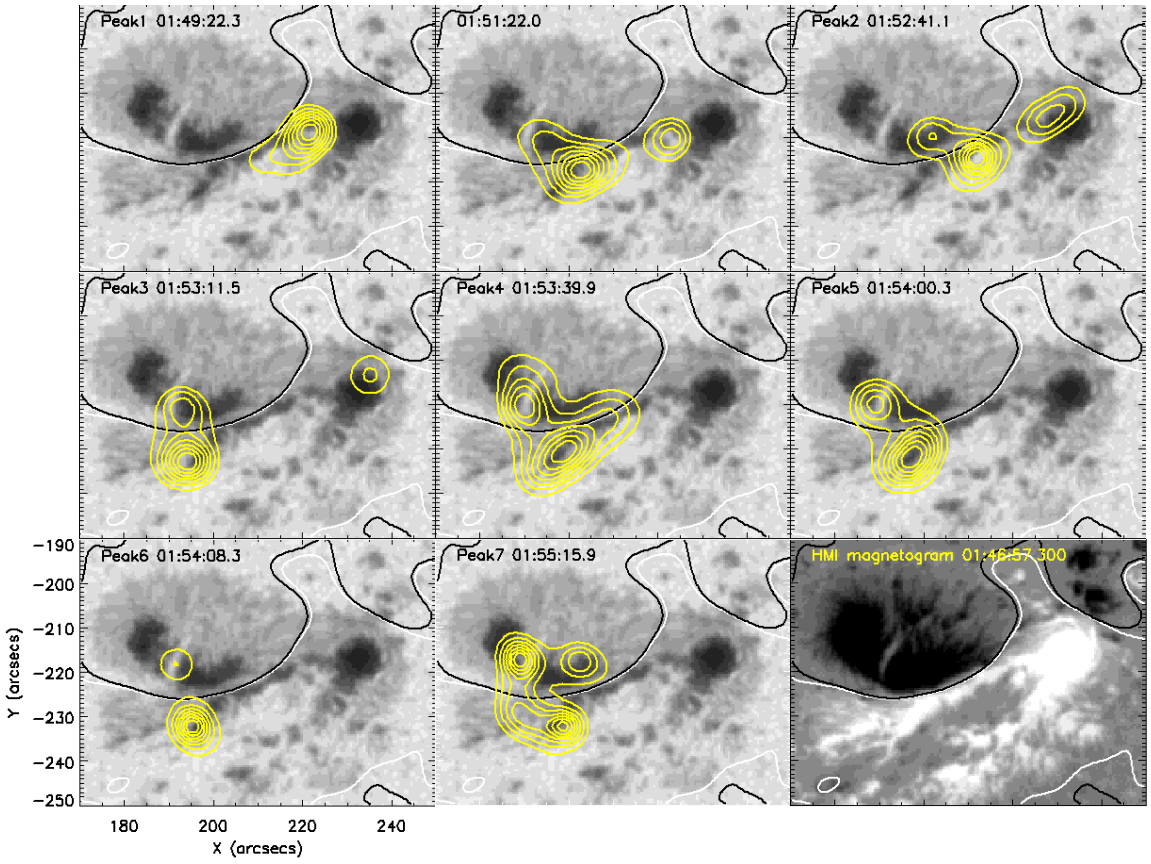

Figure 2.3 RHESSI PIXON image intensity contours in 50 – 75 keV for peaks 1-7. One frame is additionally shown between peak 1 and 2, at 01:51:22 UT (40 seconds integration) to show the flare development during this long interval (see Figure 2.1). Contour levels are 30 – 90 percent of the maximum. White and black contours indicate the positive and negative sides of the polarity inversion lines, respectively.

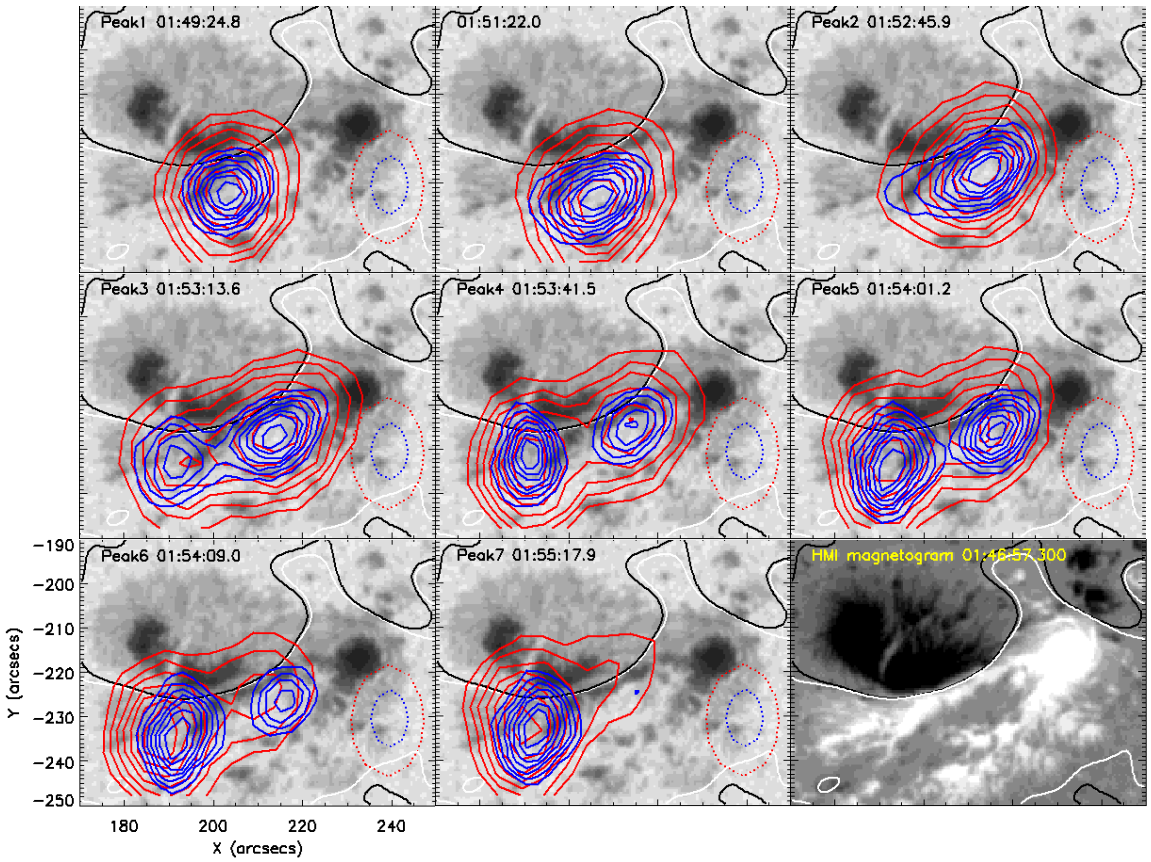

Figure 2.4 NoRH images' intensity contours in 17 GHz (red) and 34 GHz (blue) at peak times for peak 1-7 in 17 GHz time profile shown in Figure 2.1. One frame is additionally shown between peak 1 and 2, at 01:51:22 UT to show the flare development during this long interval (see Figure 2.1). Contour levels are 30 – 90 percent of the maximum. The dotted red and blue circles show the beam sizes (contour of half power beam width) at each time for 17 GHz and 34 GHz, respectively. White and black contours indicate the magnetic polarity inversion lines, as in Figure 2.3.

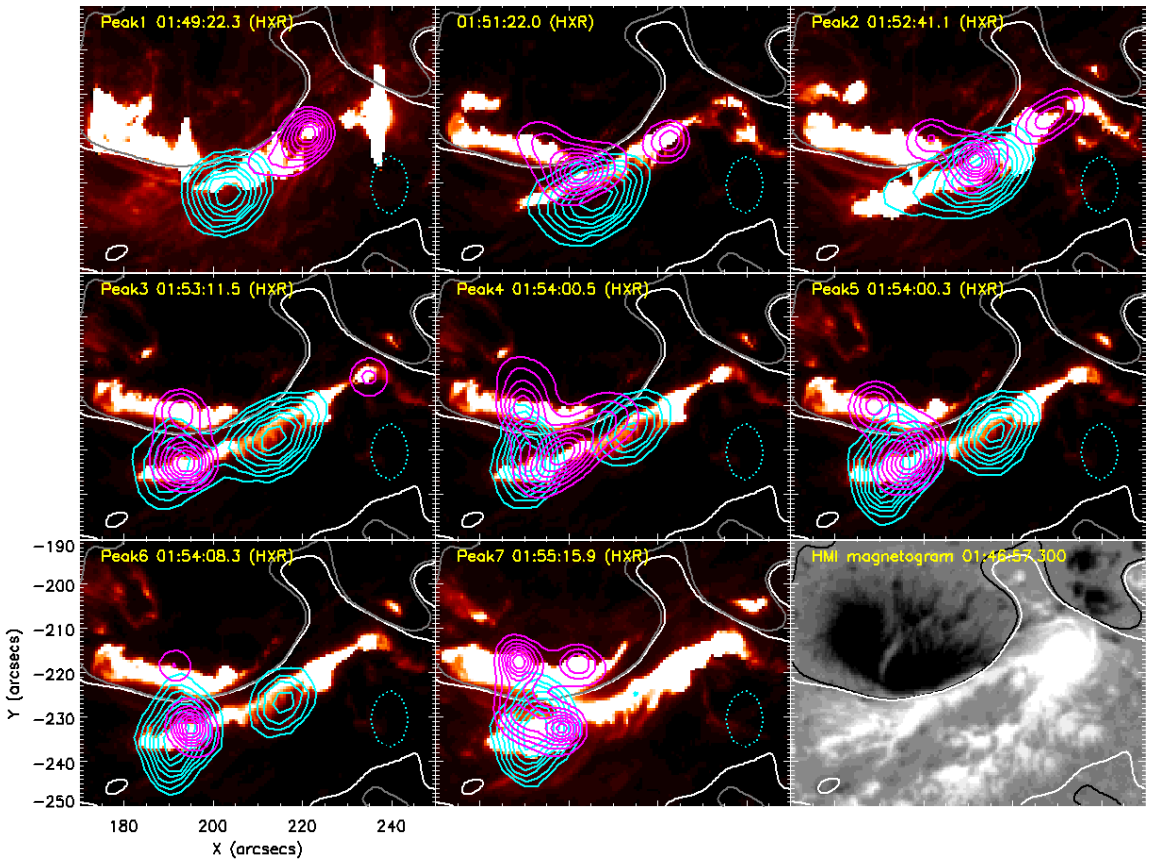

Figure 2.5 MW 34 GHz intensity contours (cyan) overlapped with HXR 50 – 75 keV energy contours (magenta) on top of AIA HeII 304$\mathring{A}$ images with the polarity inversion line, for peak 1-7. The dotted cyan circles show the beam size (contour of half power beam width) at each time for 34 GHz. One frame is additionally shown between peak 1 and 2, at 01:51:22 UT to show the flare development during this long interval (see Figure 2.3).

a loop-top source or a single footpoint source. For peak 2, there is a single elongated source to the west of double-footpoint sources. We confirmed that this is the same source as the single remote western source observed at peak 3. The single remote source in peak 3 is one of the footpoint sources expected in a quadrupolar loop configuration, and this is also observed by Wang et al. (2012). Interestingly, the location of this source coincides with one of the seismic/sunquake sources observed by Zharkov et al. (2013). For peak 4, the somewhat elongated shape of the source was likely caused by the reappearance of western footpoint source observed at peak 2, since the elogation is directed along the flare ribbon, shown in Figure 2.5. For the rather spatially complex peak 7, analysis with shorter integration time revealed that the weakest, north-western source appeared only at the end of the integration time of peak 7, and therefore most of the emissions come from the pair of north-eastern and southern footpoint sources.

It is clear from the observation of the entire period that there are two distinct double-footpoint sources involved; the one best exemplified by the HXR image at peak 2, and another one responsible for the emission during the later peaks, 3 to 7. This suggests that there are at least two distinct magnetic reconnection sites for this flare. In order to make our results more quantitative, we conducted the following analysis. First, we identified source kernel pixels by taking image pixels that are above 80 percent of the maximum intensity of the image at peaks 2 and 3. The image of these kernel pixels are shown in Figure 2.6. We produced a running average movie of HXR images in 50 – 75 keV with 4 seconds between and 40 seconds over each frame, and used this movie to plot the time profiles of the mean value of identified kernel pixels (movie provided as the online supplemental material). The result is shown in Figure 2.7. The black curve indicates the "total intensity" HXR curve, which is the same curve as the black curve in Figure 2.1, but with a 4 s resolution. The red curve is the time profile of the mean kernel intensity of the source observed at peak 2 (western

source), and the green curve is the time profile of the mean kernel intensity of the source observed at peak 3 (eastern source). The red and green vertical line marks the peak time for peak 2 and 3, respectively. The plot clearly shows the aforementioned change of double-footpoint sources; the sharp rise in intensity of the western source and the low intensity of the eastern source at peak 2 confirm that the emission was purely from the western source for peak 2. The rest of the peaks, peak 3 to 7, come mainly from the eastern source.

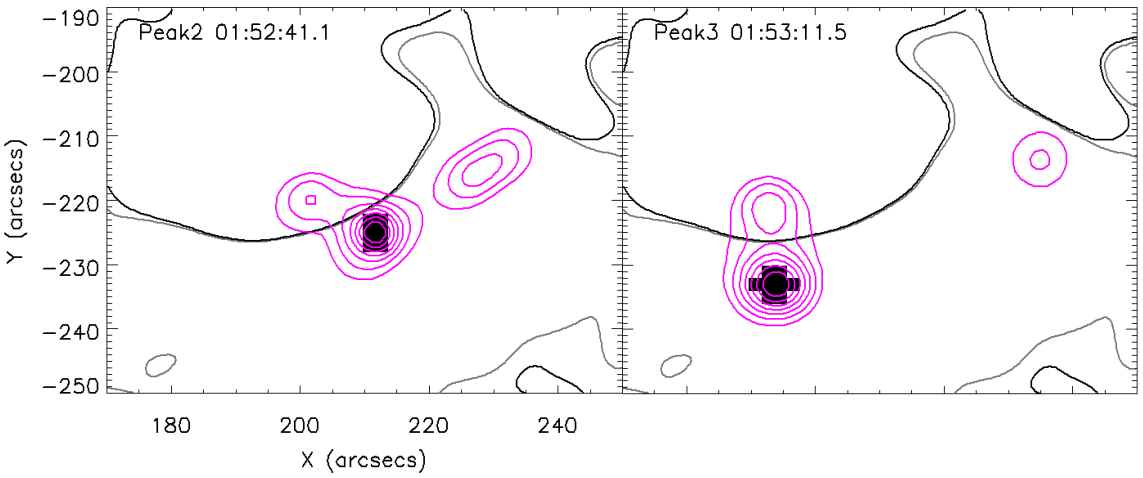

Figure 2.6 Identified HXR kernel pixels at peak 2 and 3, with threshold of 80 percent of the maximum intensity of the entire image.

Finding two spatially distinct HXR sources, we attempted to investigate if they have different spectral properties by conducting imaging spectroscopy analysis, obtaining images from 30 keV to 100 keV with 5 keV intervals. However, both sources become unrecognizable above 50 keV, preventing us from calculating meaningful spectral indices for them.

2.4.2 MW Emission Sources

For MW, Figure 2.4 shows the 17 GHz and 34 GHz images at the peak times of the 17 GHz time profile. As mentioned in the introduction, MW sources can be either a combination of loop-top and loop-legs or footpoint sources, depending on

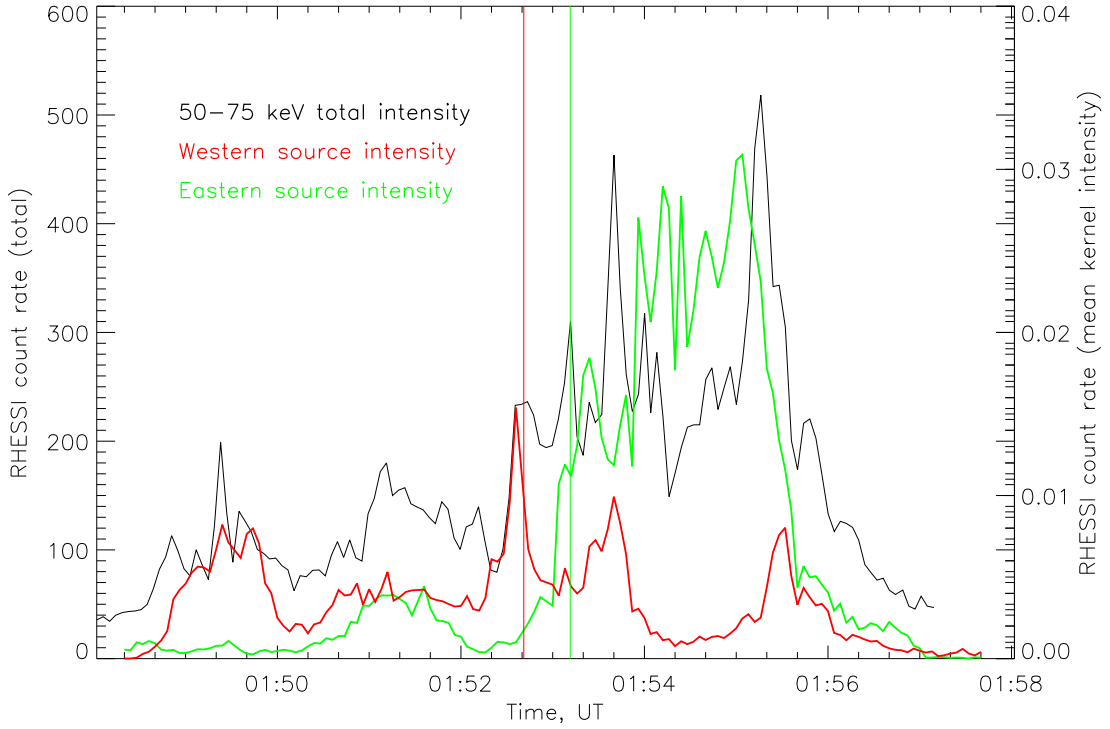

Figure 2.7 HXR total intensity vs. mean kernel intensity time profile. The black curve is the original HXR lightcurve that was shown solely in Figure 2.1, presented with the same resolution as other two colored curves (4 seconds). The red curve is the time profile for the western source, and the green curve is the time profile for the eastern source. The red vertical line marks 01:52:41.1, the peak time at peak 2, and the green vertical line marks 01:53:11.5, the peak time at peak 3.

the MW frequency. Since this flare shows sources that are spatially close in both frequencies, we assume that the source type is the same for both frequencies. We first analyze the case of footpoint sources. We know that in this flare, the peak frequency of MW emission during the impulsive phase is between 9.4 GHz and 17 GHz or higher based on the NoRP total power data (see Figure 2.2), so the 17 GHz and 34 GHz emissions are clearly in the optically thin regime. If the observed sources are footpoint sources, then this fits the scenario for the schematic model mentioned in the introduction; the emission is produced by gyrosynchrotron radiation from electrons with non-thermal energy distribution, which is dominated by footpoint sources as one reaches to optically-thin frequency range. However, in this scenario the MW sources should appear as double-footpoint sources straddling the neutral line, whereas, in Figure 2.4, the MW sources in peaks 1 and 2 are single sources, and in later peaks, when the MW sources are double sources, the pair are oriented along and well south of the neutral line. Because of the limited NoRH spatial resolution, together with the positional uncertainty mentioned in Section 2.2, we consider it likely that the sources in all cases should be shifted north by at least 5-10 arcsec (although we did not do so in Figure 2.4), and are in reality filled-loop or unresolved double-footpoint sources oriented across the neutral line. We also note that the projection effect may be taking place as well, since the active region is located in the southern hemisphere and the MW emission should be generated at some height above the photosphere even for footpoint sources (as mentioned in the Introduction); such a projection would shift the sources south relative to the surface. Support for this interpretation is provided by the NoRH circular polarization maps shown in Figure 2.8 (available only at 17 GHz, since NoRH measures the 34 GHz emission in total intensity only). Hanaoka (1996) and Nishio et al. (1997) showed that, if there are two unresolved MW sources with opposite polarities, they can appear as a single source with a gradient of the degree of polarization. Such is indeed observed in our case, where Figure 2.8 shows that peaks

3–7 to all have a N-S gradient in degree of polarization. In contrast, peak 2 has mainly E-W-oriented gradient, but from a location where the orientation of the neutral line turns more N-S. Peak 1 source may be different from all other sources, like in the case of HXR discussed in previous section. This therefore suggests that, at least for peak 2–7, our MW sources could be optically-thin, unresolved double-footpoint sources. Moreover, Figure 2.8 shows that the source with left-circular polarization (north side) has higher degree of polarization, suggesting that the magnetic field is stronger on the negative side of the polarity inversion line as observed. At the same time, Figure 2.3 shows that the HXR sources are typically stronger on the opposite, positive polarity side of the polarity inversion line, so that this interpretation also agrees with the findings of Sakao et al. (1996), who found that HXR and MW sources in loops of asymmetric magnetic strength are strongest on opposite sides of the polarity inversion line.

Although the above discussion mentions the idea that each MW source is unresolved double-footpoint sources, recent NoRH observations of larger loops (Reznikova et al. 2009, 2010), where the morphology evolution is more easily seen, indicate that the MW loops tend to start out dominated by footpoint sources but then quickly evolve to loop-leg or even loop-top dominated sources, and this is likely the case also in our event. This is the result of the accumulation of mildly relativistic electrons due to trapping in the loop, and can also explain why the sudden jump in location from western to eastern source, seen in HXR between peaks 2 and 3, is delayed and evolves more slowly in MW. To investigate this more quantitatively, we repeated the kernel light-curve analysis done for HXR, in Figures 2.6 and 2.7, for MW. It is clear from Figure 2.4 that there are three distinct MW emission sources; the one for peak 1, another one for peak 2, and the one that appears at peak 3 and continues to dominate for the rest of the peaks. Comparing to the HXR sources that

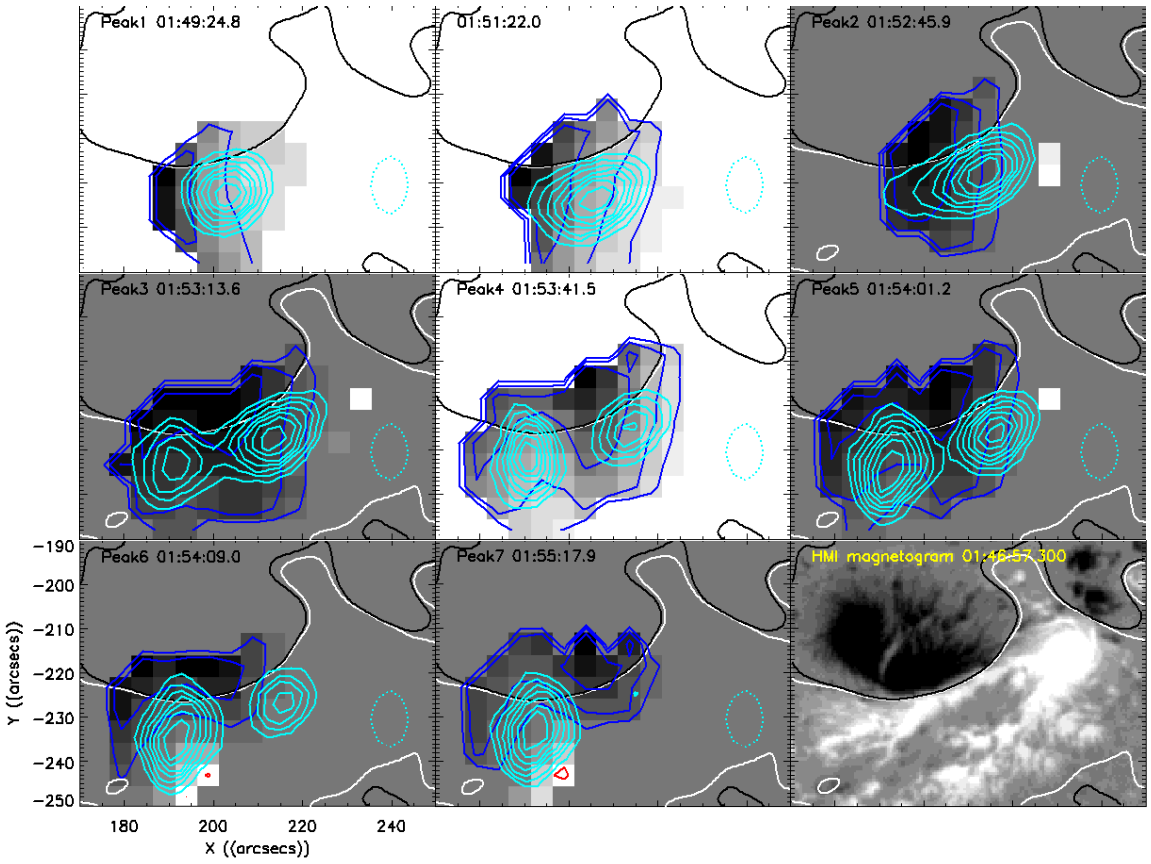

Figure 2.8 NoRH degree of polarization map (17 GHz) for peak 1 – 7. Red contours are the degrees of right-circular polarization and blue contours are the degrees of left-circular polarization, both in the scale of 5, 10, 20, 40, 60, and 80 percent. MW 34 GHz intensity contours are overlapped in cyan, with the dotted circles showing the beam size (contour of half power beam width) at each time. One frame is additionally shown between peak 1 and 2, at 01:51:22 UT to show the flare development during this long interval (see Figure 2.1).

were discussed in previous section, it is striking to note the similarity in which the sources change.

To identify the source kernel pixels, we chose 34 GHz images and used intensity thresholds of 90 percent for peak 2 source and 60 percent for peak 3 (we decreased the threshold for peak 3 because it was weaker than the peak 2 source at that time and we could not collect kernel pixels when setting the threshold above 70 percent of the maximum intensity). The kernel pixel locations are shown in Figure 2.9. We plotted time profiles for the two sources against the spatially integrated 34 GHz NoRH signal. The result is shown in Figure 2.10, with the same color scheme as for the HXR curves in Figure 2.7. The red curve is the time profile for the western source, and the green curve is the time profile for the eastern source. The red and green vertical lines mark the peak time for peaks 2 and 3, respectively. Just as in HXR, it is seen that the peak 2 emission was purely from western source, and the eastern source first appears at peak 3. However, peak 3 does not become dominant in MW until a time between peaks 3 and 4, due to the longevity of trapped particles in the western source. By the time of peak 4, it is clear that the eastern source was the only source responsible for all peaks. In summary, we observed the exact same source change behavior in MW as was seen in HXR. It is also clear from Figure 2.5 that MW sources are all located very close to HXR sources. Therefore, the observations show evidence that there are two different magnetic reconnection sites—one responsible for emission in both HXR and MW at peak 2, and another for peaks 3 to 7.

We note that the peak brightness temperatures at 17 GHz in this event are 40-70 MK, and, since the emission is optically thin, the kinetic temperature must exceed 100 MK, so the emission is undoubtedly due to nonthermal electrons. We therefore calculate the electron energy spectral index (δ) using the equation $\alpha = \log(F_{35}/F_{17})/\log(35\ \text{GHz}/17\ \text{GHz})$, where F_{35} and F_{17} indicates the flux at 35 GHz and 17 GHz, respectively, and the approximation for gyrosynchrotron emission from

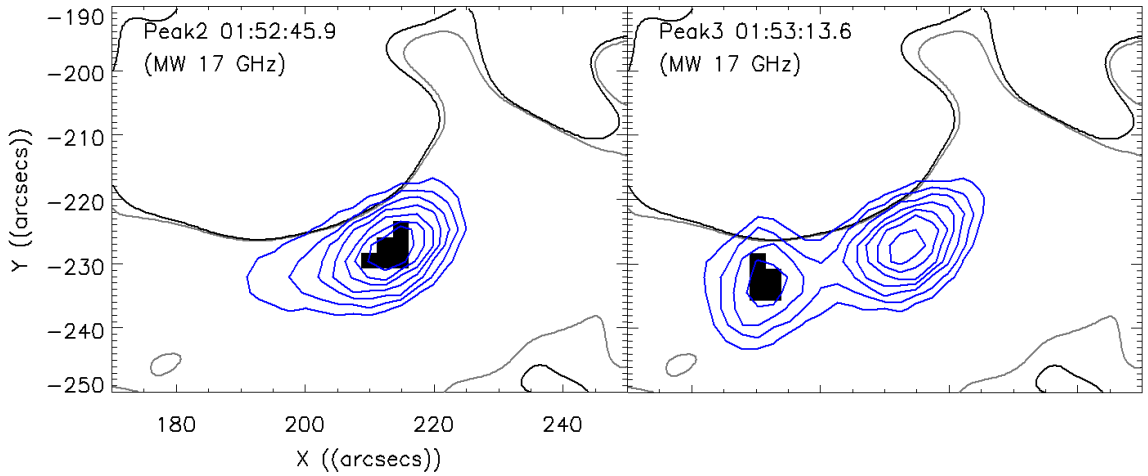

Figure 2.9 Identified MW kernel pixels at peak 2, with threshold of 90 percent of the maximum intensity of the entire image, and at peak 3, with threshold of 60 percent of the maximum intensity of the entire image.

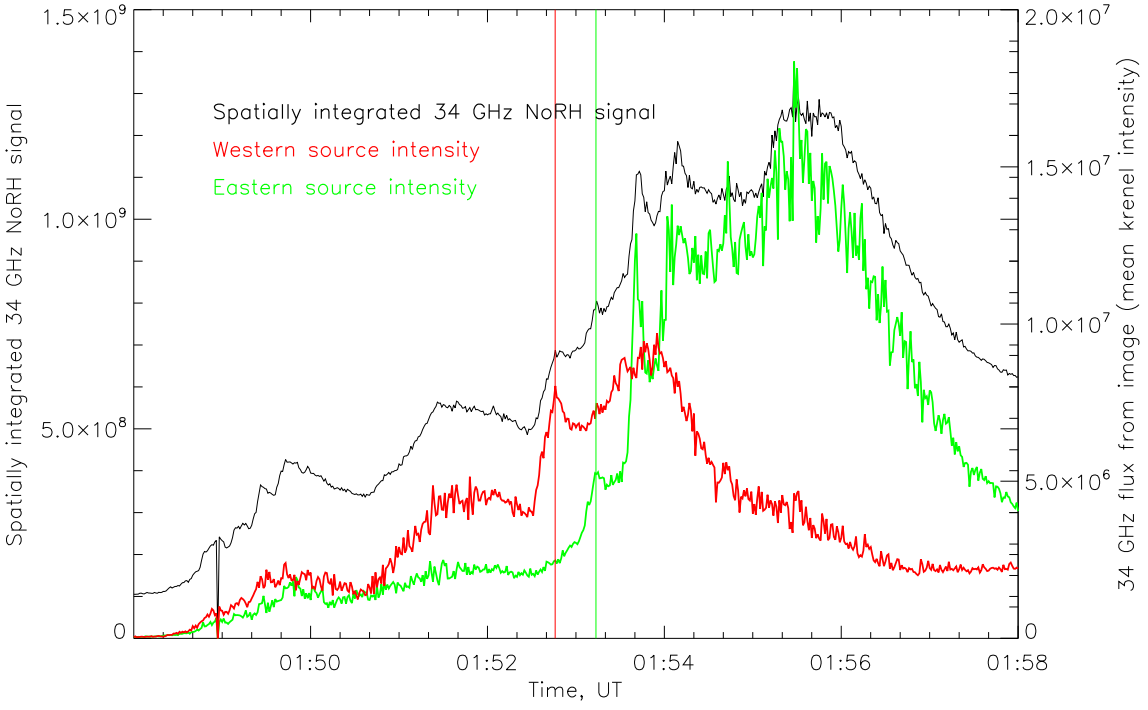

Figure 2.10 Spatially integrated 34 GHz NoRH signal vs. mean kernel intensity time profile. The black curve is the spatially integrated signal from 34 GHz NoRH images. The red curve is the time profile for the western source, and the green curve is the time profile for the eastern source. The red vertical line marks 01:52:45.9, the peak time at MW 17 GHz peak 2, and the green vertical line marks 01:53:13.6, the time of peak 3 at MW 17 GHz peak 3.

nonthermal electron energy distribution derived by Dulk (1985), $\delta = (1.22 - \alpha)/0.9$. The result is shown in Figure 2.11. We also show δ derived from HXR, which were calculated by Milligan et al. (2014), assuming a collisional thick-target model with a power-law electron spectrum at higher energies (Milligan et al. 2014). Blue vertical lines indicate HXR peak times. We see that the δ for HXR is around $5 \sim 7$, and δ for MW is around $2 \sim 3$. The difference between them is about $3 \sim 4$, which is much larger than the result found by the statistical study of Silva et al. (2000) (0.5 – 2). Their study also shows that the mean value of δ for HXR is 5.8 ± 0.8, and that for MW is 4.8 ± 1.0. Therefore, this seems to indicate that the MW indices we found may be harder than usual by $1 \sim 2$ in this scenario.

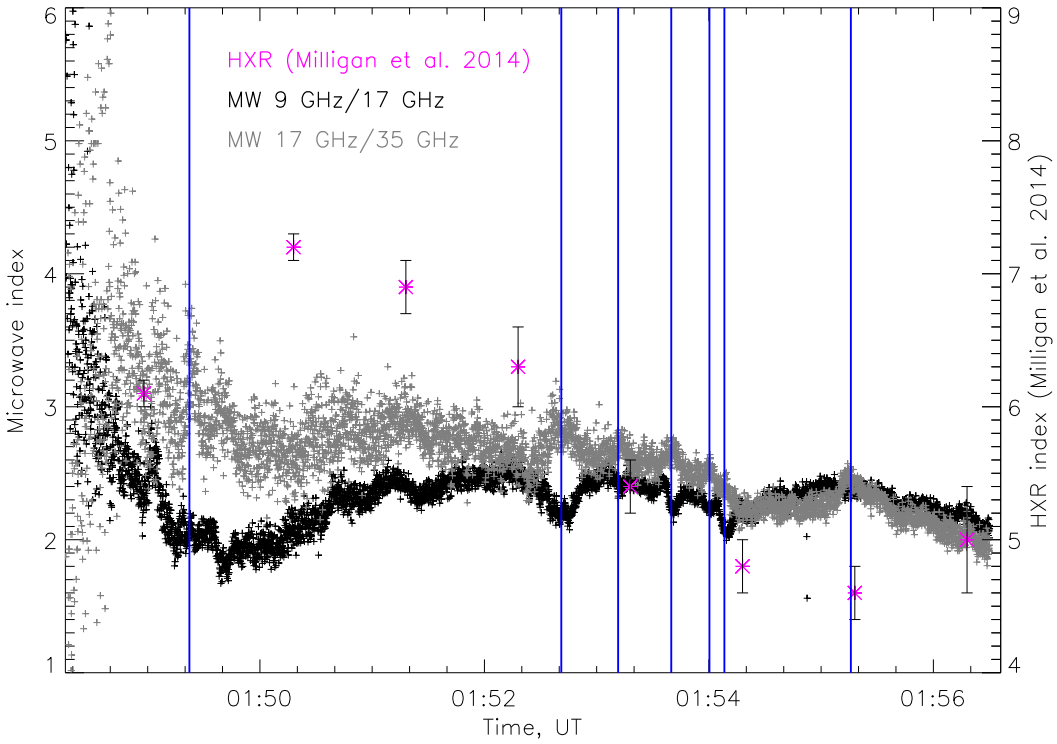

Figure 2.11 Time profile of electron spectral indices inferred from the MW observations. The electron power indices inferred from the HXR observations, calculated by Milligan et al. (2014), are also plotted. Blue vertical lines indicate time of identified HXR peaks.

2.4.3 Time Delays Between HXR Peaks and MW Peaks

As mentioned in the Introduction, in addition to the correlation between MW and HXR time profiles, it has been observed that MW peaks sometimes lag HXR peaks. We conducted an analysis on this aspect as well. Table 2.1 summarizes the delay time of MW 9.4 GHz and 17 GHz peaks respect to the corresponding HXR peaks. Note that, for peaks 5 and 6, we conclude that there are virtually no delays between HXR and either MW frequency, since delays are smaller than 2σ. We would also omit analysis for peak 2 since HXR signal for this peak involves two visually distinguishable spikes, which poses a problem in our method of determining the peak time and its uncertainty (see Section 2.3.1).

Summarizing other peaks (1, 3, 4, and 7), we found that the MW peaks are delayed relative to the corresponding HXR peaks by 1.9 to 3.0 s, with uncertainties less than 1 s. We interpret this result in light of the results on the spatial analysis we conducted in previous sections. In previous sections, we showed that, in both HXR and MW, there were two different emission sources. Since HXR and MW source locations were observed to be close to each other, we concluded that there were two different magnetic reconnection sites responsible for emission in both HXR and MW. Although peak 1 shows MW and HXR sources that are not spatially coincident (Figure 2.5), their close similarity of time profile suggests that MW and HXR emissions are closely connected, so we include it in the analysis. Thus, we compared delays among peaks 1, 3, 4, and 7. As seen in Table 2.1, since each delay is within the error bars of the others, it is hard to draw conclusions about any correlations between delays and other parameters such as MW energies, the peak X-ray or MW flux, or their ratio. Note, however, that at 9.4 GHz, the delay for peaks in the second source (peaks 3, 4 and 7) seems to increase toward later peaks. This corresponds to the general flux increase toward later peaks, seen most prominently at 9.4 GHz, and also seen in 17 GHz and 35 GHz (see Figure 2.2 peak 7 is the

strongest peak observed at $\sim$ 01:55). This correlation is explicable in terms of the idea introduced by Gary & Tang (1985), that the delay time of MW respect to HXR can be a result of the longer trapping time of MW producing electrons compared to that of HXR signal. To test this, we calculated the decay times of the 17 GHz MW signal at peak 3, 4, and 7 (by fitting each curve to simple exponentially decay function for few seconds after the peak) to be 6.05$\pm$1.29, 8.49$\pm$1.22, and 27.5$\pm$3.55 s, respectively, which increases toward later peaks, but the decay time of peak 7 is clearly strongly influenced by blended temporal peaks, and so is unreliable. To summarize, our investigation of delay times shows MW delayed with respect to HXR, but relative delay and decay times do not show a clear pattern in this event, due primarily to the breadth of the peaks, which produces relatively large uncertainties.

2.5 Discussion and Conclusion

The comprehensive observations of the 2011 February 15 X2.2 flare provide an unique opportunity to investigate the properties of accelerated flare electrons. Besides coordinated coverage in both MW and HXR imaging spectroscopy that are not often available, this event has multiple emission peaks, allowing us to investigate possible different magnetic reconnection and particle acceleration processes associated with the individual peaks. We obtained two major results in this study.

(1) We investigated time delays of MW peaks in respect to HXR peaks. Although this delay was found in several previous studies (e.g., Cornell et al. 1984; Gary & Tang 1985; Silva et al. 2000), our study allows a closer examination of such delay in the multiple peaks of a single event. We found that the MW lags HXR (50 – 75 keV) by 1.9 to 3.0 seconds, with an uncertainty below 1 second. We also found that this delay is not related to other parameters: the delay is similar for different MW frequencies, such as in 9.4 and 17 GHz; the delay does not depend on the peak flux or power index of the HXR and MW emissions; there is no difference in the

delay for the two flare stages that will be discussed in our second result below. Our study does not provide additional information beyond the existing explanation of the delays such as the concept of trap-plus-precipitation, and differences in the energy range of electrons that produces MW and HXR, as we discussed in the Introduction Silva et al. (2000).

(2) Applying image de-convolution techniques, we identified source locations of each peak in both HXR and MW. HXR and MW basically evolve with similar patterns. We found two distinct phases of the emissions, the first stage with one emission peak, and the second stage containing 5 remaining peaks. The source morphology and location change substantially between these two stages. Therefore, we postulate that, in this flare, there are two distinct magnetic reconnection sites that produced HXR and MW emissions. For HXR, we found that there is a sharp transition in a time duration as short as 30 seconds between the two stages. For MW, it is interesting to note that the first source does not immediately disappear. In fact, it remains at a site of MW emission until the last, strongest peak starts. This may be related to the result (1) concerning the trapping of electron that delays MW emissions.

It is important to understand the physical mechanisms of the two stages of emission. It is clear that they are associated with energy release in two different sites. Within each stage, the sub-peaks seem to be at the same sites. Therefore, there must be two different groups of magnetic fields that are reconnected at the two stages. Wang et al. (2012) showed that the development of this flare can be explained by the tether cutting scenario originally proposed by Moore et al. (2001). Inoue et al. (2014) has performed a data-driven MHD simulation for this specific event, and they identified two clear stages of magnetic reconnection, consistent with the tether cutting scenario as well. Our observation also seems to support the tether-cutting scenario, perhaps with with some variation, as explained in the following. In the

tether cutting scenario, a flare occurs in two stages, starting from the quadrupolar loop configuration. In the first stage, two J-shaped loops reconnect to form a set of two new loops, one small loop falling down toward the surface and another large loop erupting away from the surface. In the second stage, the erupting large loop cuts through the arcade fields as it rises, reconnecting as it meets new, larger loops. Wang et al. (2012) observed four HXR footpoints that can create two J-shaped loops, and their conjugate ends correspond to the peak 3 HXR double-footpoint sources we observed. They observed an increase in horizontal magnetic field strength in the area between these double-footpoint sources, which was interpreted as the evidence for the first stage of the tether cutting (a collapsing small loop was formed between these double-footpoint, increasing the horizontal magnetic field strength). Our observation seems to indicate that this "first stage" occurred at peak 2 as well. The schematic pictures explaining our version of the tether cutting scenario are shown in Figure 2.12. In Figure 2.12, the red circles indicate the HXR double-footpoint sources observed at peak 2 and the green circles indicate the HXR double-footpoint sources observed at peak 3. The yellow circles indicate the two remote footpoint sources that were observed by Wang et al. (2012) (we observed one of them as well, see Figure 2.3 or 2.5). The purple lines indicate the suggested flaring loops. The AIA 94 image taken at pre-flare time, 01:47:14 UT, is shown in (d) for comparison. The blue stars in (a) and (b) indicate the two different reconnection sites. We propose the following scenario for the development of this flare. First, a reconnection occurs between loop 1 and loop 2, leaving a small loop between red circles and a large loop between northern green circle and western yellow circle. This corresponds to peak 2, where HXR is emitted from the locations corresponding to two red circles and western yellow circle, and MW is emitted from the small loop formed between two red circles. Next, a second reconnection occurs between the large loop formed in the first reconnectoin and loop 3. This leaves a second small loop between two green circles and also a second large

loop between two yellow circles. This corresponds to peak 3, where HXR is emitted from the locations corresponding to two green circles and western yellow circle, and MW is emitted from the second small loop between two green circles. After peak 3, MW emission continues from the second small loop (and the first small loop). For HXR, the second large loop formed in peak 3 rises and cuts through the arcade fields, leaving the footpoint emissions through peak 4 to 7. This interpretation is based on the fact that we see the eastern HXR double-footpoint sources move around - along and away from the flare ribbon - as the flare progresses beyond peak 3 (see Figure 2.5). On the other hands, MW sources after peak 3 show almost no movements, which suggests to us that the emission was coming from relatively stable loop. Our scenario basically follows what was already proposed by Wang et al. (2012), but has a slightly new detail because of the additional sources that were observed simultaneously in HXR and MW at peak 2, **before** the first stage claimed by Wang et al. (2012). It suggests to us that, at least for this flare, the first stage of the tether cutting may have been temporally and spatially distributed.

We also estimated the sizes of flaring loops based on the HXR and MW observation. From HXR observation, the height of the loop at peak 3 is about 4,300 km (semi-circular loop shape assumption). For the same peak, MW emission is generated at the height of approximately 10,000 to 20,000 km (assuming that the projection effect is displacing the true source location 5 – 10 arcseconds). According to the simulation results by Inoue et al. (2014), the height of the top of the ascending loop at the time equivalent to right after the peak 3 in our study is approximately 21,600 km. These approximation roughly fits to our proposed scenario, that (at peak 3) the small loop left behind after the first stages of the tether cutting became the source of HXR emission at its footpoints, and the large loop that was newly formed started to erupt. Meanwhile, MW was emitted from the height between the small loop and the erupting loop - possibly from the top of the small loop.

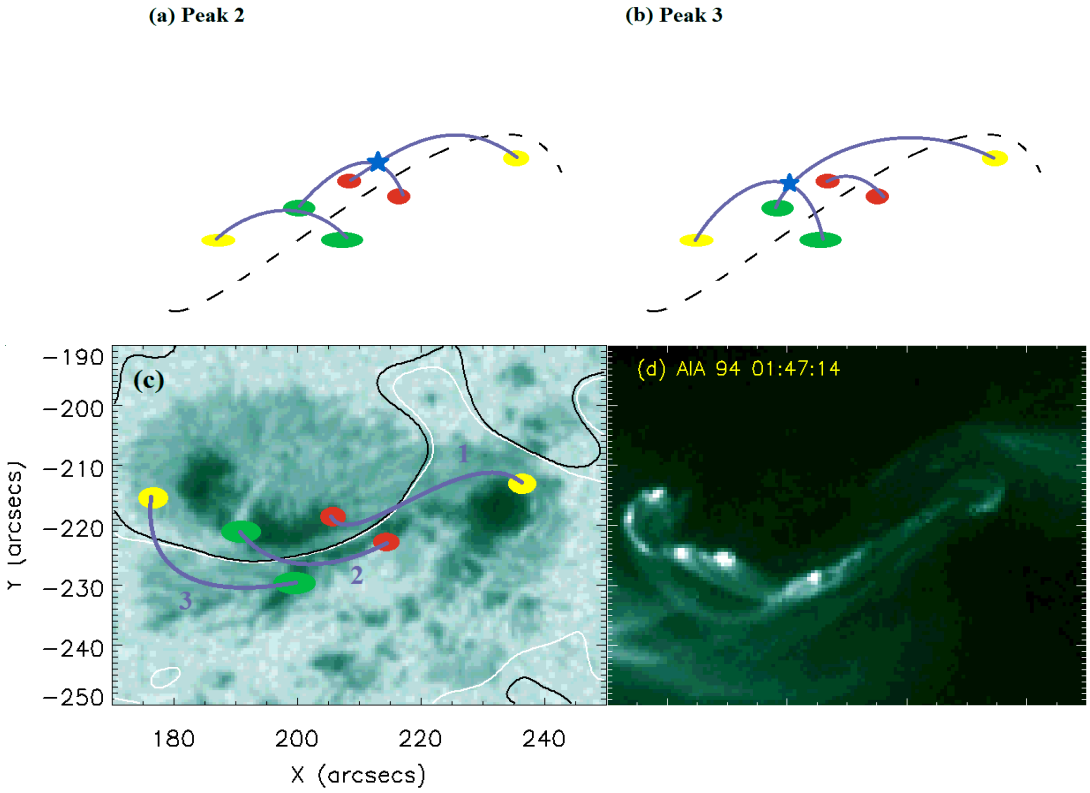

Figure 2.12 The schematic pictures demonstrating the suggested geometry of the flaring loops based on the analysis of HXR and MW sources. (a) and (b): The scenarios for peak 2 and 3, respectively. The red circles correspond to the western HXR double-footpoint sources at peak 2, the green circles correspond to the eastern HXR double-footpoint sources at peak 3, the purple lines correspond to the suggested flaring loops, and the yellow circles correspond to two of the footpoint sources that were observed by Wang et al. (2012), which were expected in their quadrupolar loop configuration. The blue stars indicate possible reconnection sites. (c): Top view of the suggested loop configuration. (d): AIA 94 image taken at pre-flare time, 01:47:14 UT. See texts for details.

Finally, our observations address the asymmetry between MW and HXR sources that was discussed by Sakao et al. (1996) and Wang et al. (1995). Those authors found that high-frequency MW sources tend to be located in strong magnetic field regions, while HXR are weaker there due to reflection of precipitating electrons by converging fields. Instead, HXR sources are stronger at weaker field regions, where MW are not as efficiently produced at high frequencies. Analyzing the magnetic structure of the AR, we found that all MW sources exhibit a gradient in degree of polarization, with the greater degree of polarization on the negative polarity side of the source. Since the NoRH maps show the sources to be located entirely on the positive-polarity side of the PIL, we believe that the true location of the radio sources should be 5-10 arcseconds north of where they appear, but are shifted southward due to the uncertainty in NoRH position calibration and/or by the projection effects. Since we found the stronger HXR sources to be on the positive-polarity side of the PIL, shifting the MW sources north would also result in consistency with the Sakao et al. (1996) and Wang et al. (1995) results. Our study would further motivate the modeling in two areas: the modeling of both HXR and MW emission based on the input accelerated electron distribution, and the modeling of the acceleration process of electrons during the magnetic reconnection.

CHAPTER 3

THREE-DIMENSIONAL FORWARD-FIT MODELING OF THE HARD X-RAY AND THE MICROWAVE EMISSIONS OF THE 2015-06-22 M6.5 FLARE

In this study [2], we conduct the simultaneous modeling of HXR and MW emission motivated by the first study introduced above. We closely examine the well-established notion of a "common population" of the accelerated electrons simultaneously producing the HXR and the MW emission during the flare impulsive phase, which has been challenged by some studies reporting the discrepancies between the two observations, as introduced in Chapter 1. The traditional methods of their spectral inversion have some problems that can be mainly attributed to the unrealistic and the oversimplified treatment of the flare emission. To properly address this problem, we use a Non-linear Force Free Field model extrapolated from an observed photospheric magnetogram as input to the three-dimensional, multi-wavelength modeling platform *GX Simulator*, and create a unified electron population model that can simultaneously reproduce the observed HXR and MW observations. We model the end of the impulsive phase of the 2015-06-22 M6.5 flare, and constrain the modeled electron spatial and energy parameters using observations made by the highest-resolving instruments currently available in two wavelengths, the RHESSI for HXR and the EOVSA for MW.

3.1 Introduction

It has been recognized that MW emission and HXR emission observed during impulsive phases of solar flares show very similar temporal behaviors (White et al.

[2]This chapter is based on the following paper: Kuroda, N., Gary, D. E., Wang, H., Fleishman, G. D., Nita, G. M., & Jing, Ju., "Three-dimensional forward-fit modeling of the hard X-ray and the microwave emissions of the 2015-06-22 M6.5 flare", *The Astrophysical Journal*, *under preparation*

2011, and references therein). This signature in general suggests that these two emissions, although observed in very different spectral windows, are produced by a common population of particles under a process of energization during the impulsive phase of solar flares. The dominant emission mechanism in the two wavelengths is likely to be different; the HXR emission is produced by bremsstrahlung and the MW emission is mostly produced by gyrosynchrotron radiation. The former is produced when high-speed electrons lose energy by collisions with more-stationary targets within the ambient plasma, producing photons with HXR energies. Thus the HXR emission is mostly dependent on and tells us about the ambient plasma density at flare site and the energy of accelerated electrons that collide with them. The latter is produced when moving electrons are deflected by the Lorentz force in the magnetized plasma. Thus the MW emission is mostly dependent on the energy of mildly relativistic electrons, and the strength of magnetic fields around which these electrons gyrate; i.e., the magnetic field strength at the flare site.

Considering the two emission mechanisms, one may assume that the two observations should converge to the same energy spectrum for the accelerated electrons, and in some simple (single-loop) flares, this is the case (e.g., Fleishman et al. 2016b). However, there is a record of observations that seems to suggest otherwise; the indices of nonthermal electron energy spectra inferred from HXR and MW observations are different (Kundu et al. 1994; Silva et al. 2000). Generally, the studies that found a difference between the HXR-inferred electron energy spectral index and the MW-inferred electron energy spectral index found that the latter is harder than the former by $\sim$2 (Kundu et al. 1994; Silva et al. 2000). Some suggest that considering two different electron energy distributions residing in different energy range (i.e., there is a break in the spectrum) could solve this problem, since MW-emitting electrons are thought to have higher energy than those emitting in HXR (Takakura 1972; Kundu et al. 1994). There are some difficulties with inferring the electron energy spectrum

from the observed HXR and MW spectrum, however. On the observational side, flares that enable us to invert the observed HXR photon spectrum to the electron energy spectrum extending above a few hundreds of keV are relatively large (e.g., high M- or X-class flares), and large flares complicate the HXR spectral inversion because the thermal part of the HXR spectrum dominates the nonthermal part at lower energies, sometimes up to 30 keV or higher. There have been some observations of giant flares showing the HXR photon spectrum extending to several hundreds of keV, but the results are mixed regarding the possible break in electron energy spectrum from event to event; the 1980 June 4 event introduced in Dennis (1988) showed a hardening break of $\sim$2 at $\sim$300 keV in the HXR photon spectrum spanning from $\sim$20 keV to $\sim$20 MeV, while 2002 July 23 event observed by the Reuven Ramaty High Energy Solar Spectroscopic Imager (RHESSI) from 250 keV to 8.5 MeV did not show such a break (White et al. 2003; Smith et al. 2003). For MW, the frequency resolution of most of the instruments that record the total solar radio intensity spectrum has been limited, and it has been sometimes difficult to determine an accurate turnover frequency, resulting in uncertainties in the spectral index of the optically thin part of the MW spectrum that is used to determine the nonthermal electron energy spectral index (Kundu et al. 1994; White et al. 2003; Kundu et al. 2009). The difference in the source locations of HXR and MW emissions (footpoint and/or above-the-loop-top for the former, whole-loop and/or footpoint for the latter) further complicates the simultaneous analysis. On the modeling side, for MW, inverting the electron energy spectrum from the observed MW spectrum has in the past been oversimplified for quantitative analysis. Therefore, the shape of the energy spectrum of the common population of electrons producing HXR and MW could be different from event to event, and whether or not it has a break at some energy remains inconclusive.

In this study, we create one unified multi-loop electron population model that can simultaneously reproduce the observed HXR and MW images and spectra at one

point in time during a flare. Unlike many previous studies, we use a realistic three-dimensional magnetic field cube based on magnetic field measurements, positioned at the actual location of the active region at the time of the observation. We constrain the model by using observations from the highest-resolving instruments available in both HXR and MW wavelengths. In Section 3.2, we introduce these instruments and the HXR and the MW observations obtained from them. In Section 3.3, we introduce the modeling platform and the work flow of our simulation for the flare. In Section 3.4, we present the results of the simulation, with quantitative parameters of the electrons. In Section 3.5, we discuss what the results suggest in terms of the spatial and the energy distributions of high energy electrons in the flare.

3.2 Data

3.2.1 Instruments

In this study, we use four observational data sources to constrain the HXR and MW emission model: HXR images, HXR spatially integrated spectrum, MW image, and MW spatially integrated spectrum. We also employ an observation-based three-dimensional magnetic field model. For X-ray images and HXR spatially integrated spectrum, the data from RHESSI are used. For this study, the collimators 2 and 4 were excluded due to their insensitivity to below ∼20 keV and the lack of segmentation, respectively, and the sensitivities of all the other collimators were lowered to as low as 76 % of the launch value (the lowest being the collimator 1). The MW data are taken from the newly expanded solar-dedicated radio array the Expanded Owens Valley Solar Array (EOVSA). Formerly known as OVSA (Owens Valley Solar Array), EOVSA is currently being commissioned to have the unprecedented imaging spectroscopic capability in frequency range of 2.5-18 GHz at more than 300 frequency channels, with the spatial resolution of ∼60 arcsec/ν_{GHz} (finest 3.3 arcsec at 18 GHz), 1-s time cadence, and four polarizations. At the time of the event used for this study, EOVSA was recording total radio flux intensity and

cross-correlated amplitudes from nine baselines from seven antennas. We used the total intensity MW spectrum (spatially integrated spectrum at 171 frequency channels within 2.5-18 GHz), and the relative visibilities calculated from the cross-correlated amplitudes as a spatial constraint replacement for images, which were not available yet.

The cross-correlated amplitudes from a baseline can be converted into one-dimensional relative visibility spatial information to determine the characteristic source size in the direction of the baseline orientation, assuming a simple Gaussian source shape. We use the following relationship (see Appendix for derivation):

$$\ln(V_{Rel}) = \ln(\frac{a_{ij}}{\sqrt{a_{ii}a_{jj}}}) = -8.393 \times 10^{-11} B_{\lambda}^2 d^2 = -9.325 \times 10^{-14} B_{cm}^2 d^2 f_{GHz}^2 \quad (3.1)$$

where a_{ij} is the cross-correlation amplitudes from the baseline consisting of antenna i and j, a_{ii} and a_{jj} are the auto-correlation total power amplitudes from antenna i and j, respectively, B_{λ} is the projected baseline length in number of wavelength, d is the one-dimensional characteristic source size in arcseconds, B_{cm} is the projected baseline length in cm, and f_{GHz} is the observing frequency in GHz. Note that, with this definition, V_{Rel} is independent of calibration because antenna-based gains cancel within $\frac{a_{ij}}{\sqrt{a_{ii}a_{jj}}}$. This shows that if the plot of $\ln(\frac{a_{ij}}{\sqrt{a_{ii}a_{jj}}})$ vs. B_{λ}^2 shows a linear dependence with a negative slope, then the one-dimensional characteristic source size can be estimated by a simple relationship. The steeper the slope, the larger the source size in the direction of that baseline's orientation. In reality, the source could be elongated more in one direction than another. Such size variance will be projected onto the baselines with different orientation angle; the relative visibility plots from different baselines with different orientations can reveal the characteristic source size in different directions. At the time of the event for this study, the prototype correlator was not producing valid auto-correlations. Therefore, we used the cross-correlated

amplitudes from the shortest baseline as a proxy for auto-correlated total power amplitudes for each baseline (i.e., $\sqrt{a_{ii}a_{jj}} \sim a_{12}$ where antenna 1 and antenna 2 constituted the shortest baseline within the array). The length of this baseline at the time of the observation was B_λ ∼508 at the highest frequency (18 GHz), which yields the minimum fringe spacing of ∼400 arcseconds. This is confirmed to be well above the size of the target active region, which means that this baseline should not be resolving any flaring sources. Therefore, the cross-correlated amplitude from this baseline can be used as a good approximation for the total power from each antenna, although this approximation now has the disadvantage that V_{Rel} is no longer independent of calibration.

For the magnetic field model, we used the Non-Linear Force Free Field (NLFFF) model extrapolated from the SHARP Active Region Patches Cylindrical Equal Area (CEA) photospheric vector magnetogram from Helioseismic and Magnetic Imager (HMI; Schou et al. 2012) on board the Solar Dynamic Observatory (SDO; Pesnell et al. 2012) (available every 12 minutes). The net force and torque in the observed photospheric field are first minimized by a preprocessing procedure in order to obtain the chromosphere-like data that meets the force-free condition (Wiegelmann et al. 2006); for advantages in disadvantages of this approach, see Fleishman et al. (2017). The weighted optimization method (Wheatland et al. 2000; Wiegelmann 2004) is then applied to the preprocessed photospheric boundary to perform the NLFFF extrapolation within a box of $256 \times 180 \times 200$ uniform grid points, corresponding to $\sim 230 \times 160 \times 180$ Mm^3. The performance of the extrapolation was verified by visually comparing the model field lines with the $171\mathring{A}$ channel images from Atmospheric Imaging Assembly (AIA; Lemen et al. 2012) on board the SDO.

3.2.2 Observations

In this study, we analyze a well-observed M6.5 flare that occurred on 2015 June 22 (Jing et al. 2016; Liu et al. 2016; Wang et al. 2017). The flare started around 17:50 UT, and reached the Soft X-ray (SXR) peak (1.0-8.0 $\AA$ channel of Geostationary Operational Environment Satellite (GOES) X-ray monitor) at around 18:23 UT, and subsided to background level at around 02:00 UT on the next day. Figure 3.1 shows the lightcurves from GOES, RHESSI, and EOVSA for this flare from 17:36 UT to 18:43 UT. There were two precursors at around 17:24 UT and 17:42 UT (only the latter is shown in Figure 3.1) (Wang et al. 2017). The parent active region 12371 was located at N13W06 at the time of the flare.

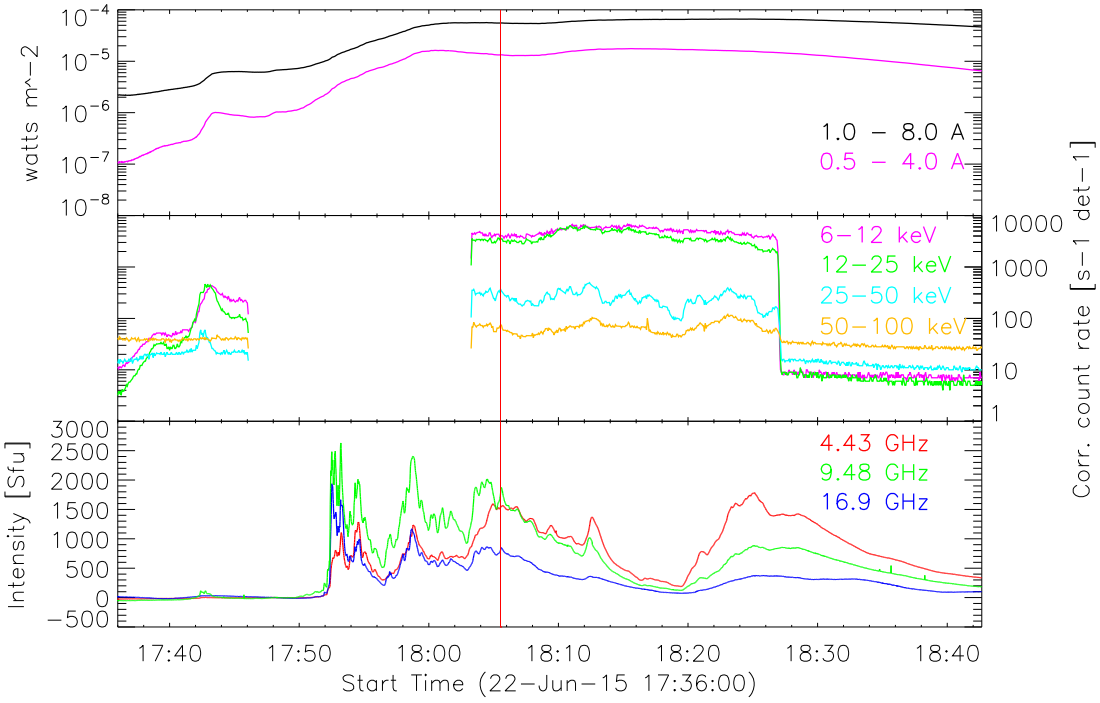

Figure 3.1 Lightcurves from GOES (top), RHESSI (middle), and EOVSA (bottom) for 2015-06-22 X6.5 flare. RHESSI's data gap is due to its passage through the South Atlantic Anomaly. The vertical red line indicates 18:05:32 UT, the time at which the simultaneous modeling of HXR and MW observations was conducted. The drop in the RHESSI lightcurve at ~18:27 UT is due to the spacecraft's night time.

As seen in Figure 3.1, RHESSI missed most of the impulsive phase of the flare due to its passage through the South Atlantic Anomaly (SAA). However, EOVSA coverage during this period shows multiple sharp peaks leading to GOES SXR maximum. In this study, we must choose a time covered by both RHESSI and EOVSA for the model, and since HXR images are crucial in this modeling, as will be shown in the later section, we chose the earliest time at which RHESSI's HXR 25-50 keV lightcurve showed the peaky behavior after the spacecraft came out of SAA. This was 18:05:32 UT, which is indicated by the red vertical line in Figure 3.1.

Figure 3.2(a) shows RHESSI image contours (50, 70, 90 %) in 6-12, 20-35, and 50-75 keV obtained at 18:05:32 UT, integrated over 2 minutes, reconstructed with the CLEAN algorithm, overplotted onto the HMI line-of-sight (LOS) magnetogram taken at 18:04:26 UT. The image shows clear double footpoint emissions in 50-75 keV rooted at regions of opposite magnetic field polarity. The region joining these footpoints is filled by a 6-12 keV source, presumably coming from the loop filled with heated chromospheric plasma, although it cannot be determined if this loop is footed exactly at the 50-75 keV sources. The intermediate-energy 20-35 keV image shows an interesting morphology; two of the sources are nearly co-spatial with the 50-75 keV footpoint sources, but one is located between them, giving the appearance of three sources tracing out one loop that connects them. The centroid of this middle 20-35 keV source and the centroid of 6-12 keV source (the center of its northwestern bulge) seems to be slightly shifted, and since there seems to be no region of strong magnetic field corresponding to the location of the middle 20-35 keV source (in contrast to the case of 50-75 keV source), we interpret this source as the so-called above-the-loop-top (ALT) HXR source (e.g., Masuda et al. 1994). We estimated the difference between the centroid of this source and the centroid of the 6-12 keV source based on the field line geometry of the NLFFF extrapolation model, and found that it is about 20,000 km. This is in agreement with past studies that measured the size of the

current sheet formed between coronal HXR source and thermal looptop source in the flare of similar magnitude (M1.2, 17,500 - 33,000 km; Sui & Holman 2003). It is possible that this source is a thermal source, and we will briefly discuss the variation in the model corresponding to this interpretation in later section (Section 3.4.3). Figure 3.2 (right) shows the background-subtracted (background time range was 17:11 - 17:18 UT) RHESSI HXR photon spectrum created by the Object Spectral Executive (OSPEX; Schwartz et al. 2002) software, integrated over 8 seconds centered at 18:05:32 UT. The spectral fit was done using OSPEX, with a single-temperature thermal bremsstrahlung radiation function ("*vth*") and the instantaneous nonthermal bremsstrahlung with an isotropic pitch-angle distribution ("*thin2*"). The fitted parameters and goodness-of-fit value are listed in Table 3.1.

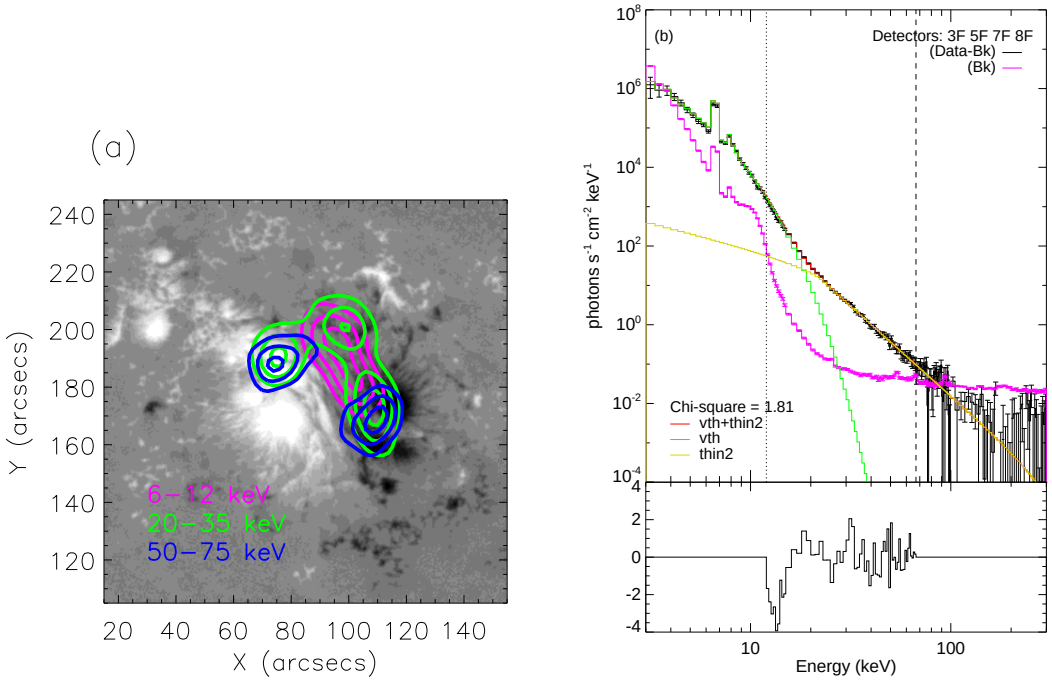

Figure 3.2 (a) RHESSI CLEAN image contours (integrated over 2 minutes) at 18:05:32 UT, overplotted onto the HMI LOS magnetogram taken at 18:04:26 UT. (b) RHESSI HXR photon spectrum taken at 18:05:32 UT, accumulated over 8 seconds using the front-end of collimators 3, 5, 7, and 8. The background was taken from 17:11 UT to 17:18 UT. The spectral fit was done combining *vth* and *thin2* functions in 12-76 keV (dashed lines), to obtain the instantaneous electron flux density distribution. The goodness-of-fit value was 1.81, with the normalized residuals plotted at the bottom.

Table 3.1 The Summary of the OSPEX Fitted Parameters for the Photon Spectrum Taken At 18:05:32 UT, With *vth + thin2*

Parameter	**Values**
Emission Measure (*vth*)	1.3×10^{49} cm^{-5}
KT (*vth*)	2.0×10^{7} K
Normalized flux density	2.4×10^{55} cm $^{-2}$ s $^{-1}$
E_{cutoff}	22.1 keV
δ_1	3.6
E_{bk}	291.1 keV
δ_2	6.5
E_{max}	32,000 keV
χ^2	1.81

Figure 3.3 (bottom) shows the background-subtracted (background's time range was 17:47:43 UT - 17:48:33 UT) MW total intensity spectrum taken from EOVSA at 18:05:32 UT. Figure 3.3 (top left) shows $ln(V_{Rel})$ vs. B_λ^2 plot from the longest baseline, which is able to resolve the smallest feature among all baselines, and the top right shows one of the shorter baselines with different orientation angle. As introduced in the previous section, if this plot shows a linear dependence, then from the slope we can estimate the one-dimensional characteristic source size in the direction determined by the baseline orientation; -53 degrees for the former and 71 degrees for the latter, clockwise from the Heliocentric-Cartesian x-axis. Note that y values above zero (at the low B_λ^2 end) are not considered in the analysis for both baselines, since the

numerator of $\frac{a_{ij}}{\sqrt{a_{ii}a_{jj}}}$ should not be larger than the denominator in general. We believe that they are coming from the effect of dissimilar calibration at those frequencies among four antennas involved. The longer baseline shows a linear dependence in $10^7 < B_\lambda^2 < 7 \times 10^8$ (corresponding to $6 < f_{GHz} < 15$, as B_λ has a one-to-one correspondence with frequency as shown in Equation. 3.1), whose slope indicates a size of ∼16 arcsec (the least-square fit to the range determined by eye). There seems to be a steeper slope in lower B_λ^2 range, although it is difficult to determine the exact source size because of the scatter in the data points (estimates vary between ∼20 to ∼35 arcsec depending on the fit). The plot above $B_\lambda^2 \sim 7 \times 10^8$ looks rather flat or even increasing, which would indicate that there is a new source with competing intensity but different characteristic size appearing above this frequency. Since such judgment is not possible unless we extend the plot beyond the high frequency limit of the instrument, we will not use this part of the relative visibility plot for the observational constraint for our model. The shorter baseline also shows a relatively straight slope in $400,000 < B_\lambda^2 < 1,500,000$ ($8 < f_{GHz} < 15$), which is calculated to have the size of ∼27 arcsec. In summary, these two plots tell us that our target source has a simple east-west elongated shape from ∼8 to ∼15 GHz, and perhaps slightly larger size in $\lesssim$ 6 GHz in -53 degree direction.

3.3 Simulation Platform and Workflow

As mentioned in the Introduction, in this study we create a sophisticated 3D model that places within a realistic three-dimensional magnetic field data cube a set of electron populations that reproduce observed HXR and MW emissions. The simulation platform we use is the *GX Simulator* (Nita et al. 2015). It is an IDL-based, graphical-user-interface (GUI) platform which has a highly diverse functionality of which we employ here the following.

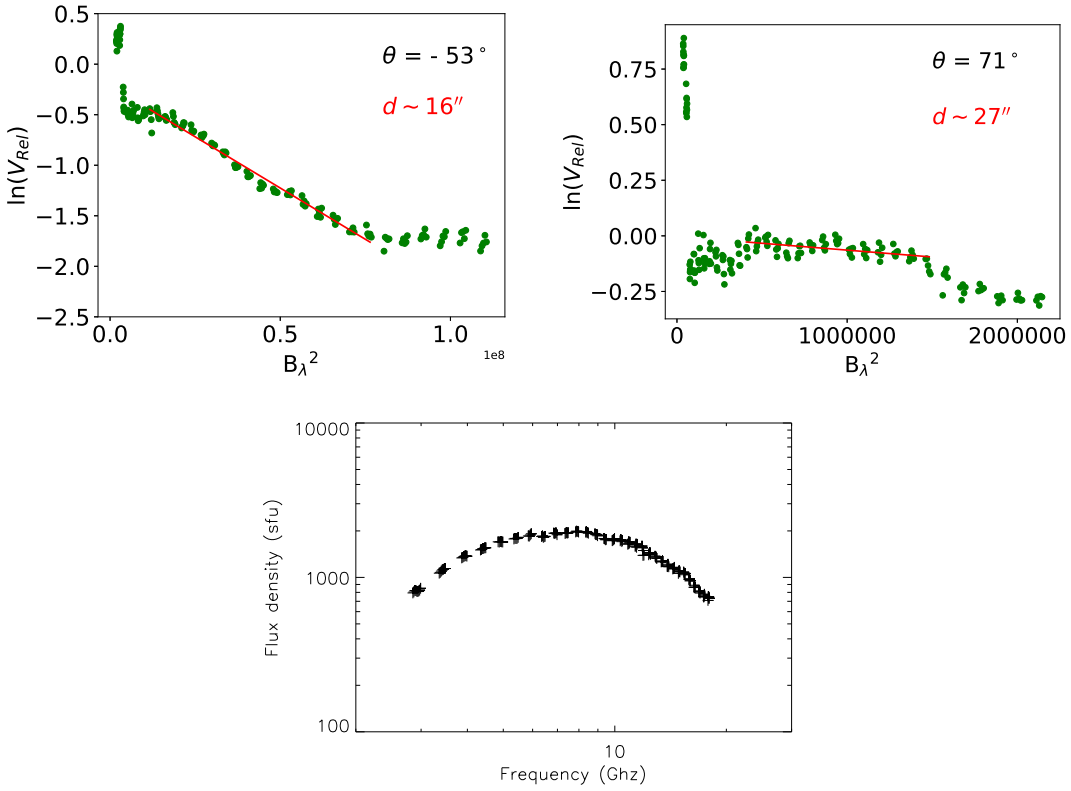

Figure 3.3 Top: EOVSA's $\ln(V_{Rel})$ vs. B_λ^2 plot calculated from the cross-correlated amplitudes taken from the longest baseline (left) and one of the shorter baselines (right) that were available on 2015, Jun. 22. The straight negative slope can be used to calculate the characteristic source size in the direction of the baseline orientation (θ, clockwise from the Heliocentric-Cartesian x-axis). Note that y values above zero are not considered in the analysis (see Section 3.2.2). The red lines are the least-squared fits to the ranges of B_λ^2 determined by eye (each corresponding to $6 < f_{GHz} < 15$ and $8 < f_{GHz} < 15$, respectively, as B_λ has a one-to-one correspondence with frequency). d is the one-dimensional characteristic source size calculated from those fitted slopes. Bottom: EOVSA background-subtracted total intensity spectrum plot taken at 18:05:32 UT.

First, we import an externally-defined NLFFF magnetic field model into the simulator. Then, we investigate the magnetic field topology and create magnetic flux tubes using the observed HXR images for guidance. This flux tube construction process is an iterative process, and we try to find the magnetic field model that contains the field lines that best connect the observed HXR sources. After several trial-and-error iterations, we selected the model cube extrapolated at 18:24 UT. The models at other times, for example, the one at 18:00 UT, had too much shear in the overall field line geometry, and we could not obtain the desired source connectivity. Since 18:24 UT is later than our modeling time (18:05:32 UT), this cube must contain more post-reconnection loops, which should be more suitable for modeling MW emissions that presumably come from trapped electron populations. The flux tubes are developed using these central guiding field lines.

Next, we populate the flux tube with thermal and nonthermal populations of electrons, defined to have the required spatial and energy distribution functions. Here, the spatial distributions of the electrons are assigned based on the observed HXR images in Figure 3.2(a), and the energy distribution functions are assigned guided by the OSPEX's spectral fit to the observed HXR spectrum in Figure 3.2(b). The simulator allows users to define the electron spatial distribution functions independently for thermal and nonthermal electron populations. For particle energy distribution, the simulator provides a predefined list of well-known functions such as thermal-plus-single-power-law, thermal-plus-double-power-law, Kappa, and others, as well as the choices of pitch-angle distribution such as isotropic, exponential loss-cone, Gaussian loss-cone, Gaussian, and a generalized Gaussian (full list provided in Fleishman & Kuznetsov 2010; Nita et al. 2015). The simulator also has an ability to define chromospheric layers with parameters such as plasma density, temperature, and depth. For this study, the energy distribution for each of the electron populations were taken from the RHESSI spectral fit that was introduced in Section

3.2.2, which is a thermal-plus-double-power-law consisting of single-tempearture thermal bremsstrahlung and the instantaneous nonthermal bremsstrahlung radiation functions. The thermal and nonthermal parts were appropriately assigned based on our interpretation of the nature of the observed sources.

Then, we generate 2D HXR and MW images and spectra through calculations using internal codes. The simulator's HXR code calculates the observable flux of HXR photons at 1AU by summing the combination of thermal and nonthermal bremsstrahlung radiations from each voxel. The thermal part of the X-ray code calculates the total bremsstrahlung power radiated from the plasma with a single temperature T, taking into account collisions with hydrogen and other atoms, free-free and free-bound transitions, and various line emissions (Schwartz et al. 2002). The nonthermal code uses the instantaneous bremsstrahlung expression for each voxel of the volume:

$$I(\epsilon, \vec{r}) = \frac{n_p(\vec{r})V}{4\pi R^2} \int_{\epsilon}^{\infty} Q(E, \epsilon) F(E, \vec{r}) dE \tag{3.2}$$

where R is 1AU distance, V is the volume of the voxel, ϵ is photon energy, $F(E, \vec{r})$ is the electron flux density distribution over energy in the given voxel, and $Q(E, \epsilon)$ is the angle-averaged bremsstrahlung cross-section introduced by Haug (1997). Then, provided that the HXR emission is optically thin, the individual contributions are added up along the LOS to form a set of HXR images at various energies. The emission can then be integrated over the image to yield the total power HXR spectrum for comparison with Figure 3.2(b). Currently, the HXR code only calculates electron-ion bremsstrahlung and does not account for Compton scattering or photoelectric absorption of HXRs in the solar atmosphere, with the latter known to produce a broad hump on the photon spectrum around 30-50 keV (Bai & Ramaty 1978). Also, since the nonthermal code calculates the instantaneous bremsstrahlung (i.e.,

thin-target model), it cannot self-consistently model the injection spectrum of the energetic electrons predicted by the thick-target flux model. We note, however, that the nature of the simulator allows us to model each type of the observed HXR sources separately, while in the observation and the subsequent spectral forward-fitting, we are not spatially resolving the sources. Therefore, we expect that the final model consists of a mixture of the thin- and the thick-target bremsstrahlung, and only for the case where we are modeling the source solely produced by the thick-target bremsstrahlung, we will give the proper modification to that modeled electron spectral index accordingly.

The simulator's radio emission code is based on the fast gyrosynchrotron (GS) algorithm developed by Fleishman & Kuznetsov (2010), which accounts for GS and free-free radio emission and absorption in a thermal plasma (e.g., Razin effect is included) within the modeled cube (vacuum outside). The fast GS code is a generalization of a numerical Petrosian-Klein (PK) approximation of the exact GS equations, which is more precise than that approximation and also valid for an anisotropic pitch-angle distribution. It can reproduce discrete harmonic structures at low frequency if requested by the user, or averages over them otherwise. The 2D image at a given frequency is calculated by solving the radiative transfer equation along the LOS, and it includes frequency-dependent mode coupling in addition to emissivity and absorption.

Lastly, we compare simulated HXR and MW images and spectra with the observed images and spectra. The simulator has an ability to convolve the pixelated 2D model image with a user-defined point-spread-function/beam, which enables the user to directly compare the model images to the observed images that go through instrumental responses. For HXR, the model images are convolved with a Gaussian point-spread-function with FWHM of 6.79 arcseconds, according to the nominal FWHM resolution of the finest resolving collimator that was used to reconstruct the

observed RHESSI image (collimator 3). For MW, the model visibility was obtained by convolving the visibility of the pixelated model image from the simulator with the sampling function of the EOVSA array at the modeling time. We fine-tune the model in HXR first, and then in MW. The HXR model images and spectra are first created and tested against the observed HXR emission spectra and images. After fine-tuning this HXR-constrained model, we use it to produce the model MW images and spectra, which are later tested against the observed MW images and spectra. This MW-constraining step requires another fine-tuning in MW, which alters the match obtained in the HXR fine-tuning, so another HXR fine-tuning is run again, and so on. We iterate these fine-tunings several times to converge to the unified model that can simultaneously reproduce the observed HXR and MW images and spectra. During the fine-tuning process, most of the initial parameters (both spatial and energetic) can be modified to obtain the best match with the observations, but emission measure is constrained by comparing the emission measure calculated by the simulator (the square of thermal particle density integrated over the model volume) with the emission measure calculated from the OSPEX "*vth*" function. This workflow, which is based on the framework introduced by Gary et al. (2013), is illustrated in Figure 3.4.

3.4 Model Construction

3.4.1 Constraining in HXR

As the first step in this modeling workflow, we created three flux tubes to reproduce HXR emission in three different energy channels, guided by the RHESSI HXR images. We could not reproduce all observed sources with a one or two-loop model because the field line rooted in the 50-75 keV footpoint source locations did not trace out the 6-12 keV source nor cross the 20-35 keV ALT source.

Figure 3.5 shows each flux tube and their respective thermal and nonthermal populations. Note that we will be representing the non-ALT 20-35 keV source by the

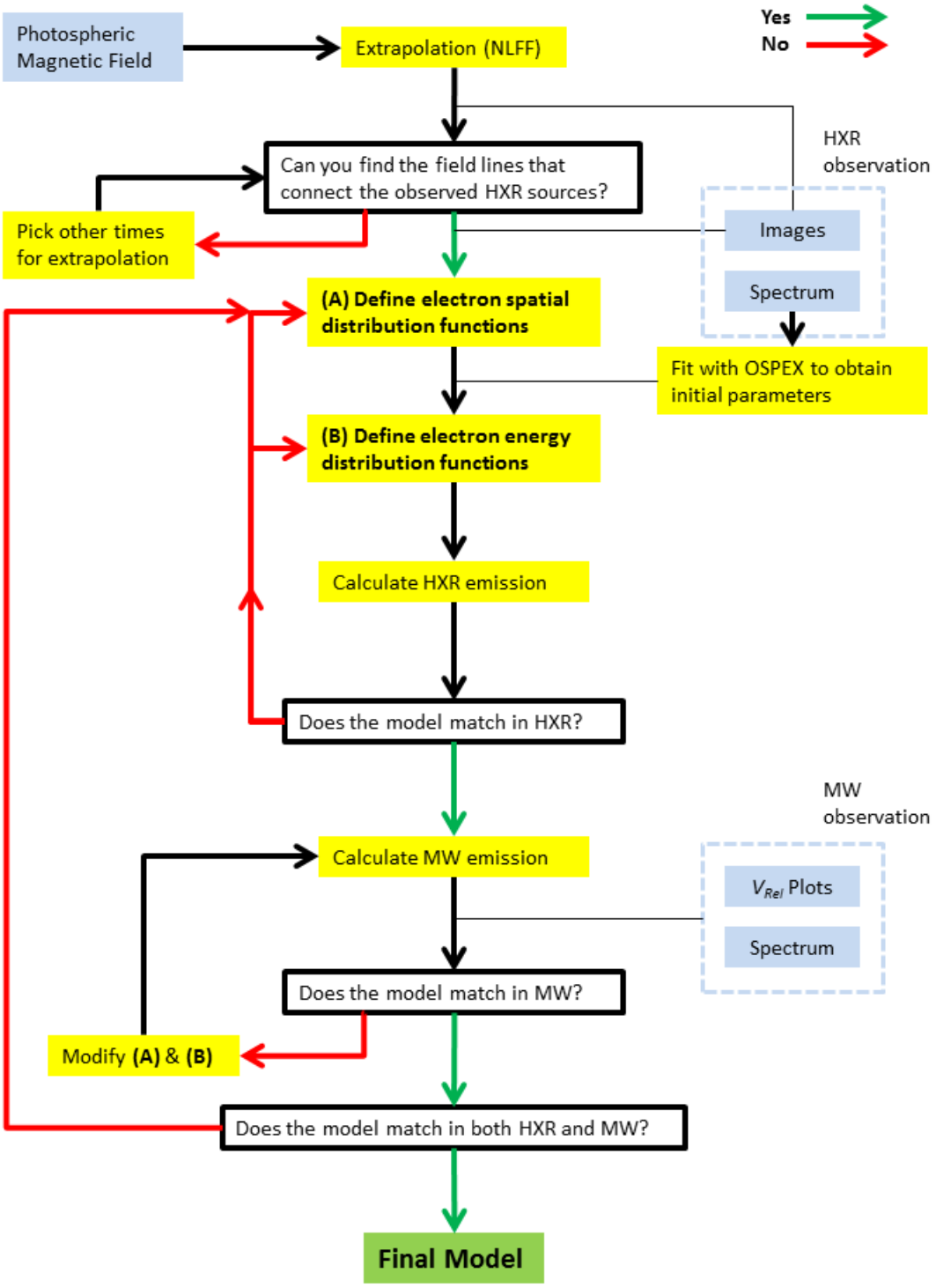

Figure 3.4 The diagram illustating the workflow of the simulation in this study, based on the framework introduced by Gary et al. (2013).

footpoint emissions from the flux tube representing 50-75 keV sources, since they are spatially close to 50-75 keV footpoint sources in RHESSI image and creating another loop footed at the non-ALT 20-35 keV sources will overcomplicate the model. The first flux tube, in Figure 3.5 (a), is the one representing the 6-12 keV source, lying low in the corona with the apex height of ∼8,200 km from photosphere, filled with the thermal population slightly concentrated at the looptop. We note that it was necessary for us to choose such a low-lying structure based on the observed 6-12 keV image; any field lines higher than the selected field line resulted in the misorientation of the model source compared to the observed source. We call this loop "Thermal-only loop". For the thermal population, we kept the temperature predicted by OSPEX (20 MK), but altered the density distribution to match the observed source shape, adding one Gaussian function centered slightly off from the looptop to the uniform distribution. Then, we fine-tune the density so that the emission measure calculated from the simulator becomes equal to the one predicted from OSPEX. As a result, we found that the thermal population has a density of 1.1 $\times 10^{11}$ cm^{-3} at the bottom and 1.6 $\times 10^{11}$ cm^{-3} at the top of the loop. We assign this flux tube zero nonthermal particle, assuming that this loop is dominated by thermal plasma from chromospheric evaporation - an expected outcome from earlier episodes of particle acceleration.

The second flux tube, Figure 3.5(b) and (e) (middle column), is the one representing the 50-75 keV double footpoint sources, thermal electrons and nonthermal electrons uniformly distributed along the loop with the height of ∼21,000 km from the photosphere. Note that the HXR emission from this loop will be dominated by footpoints even though the nonthermal electrons are uniformly distributed along the loop, due to a dense chromospheric layer within the magnetic field cube (defined with $n_p = 10^{13}$cm^{-3}, T = 3,500K, and the depth of ∼2000 km, the default values assigned by the simulator). We call this loop "Lower loop", and assign its thermal populations a density of 5.0×10^9 cm^{-3}, which is the default value of the simulator,

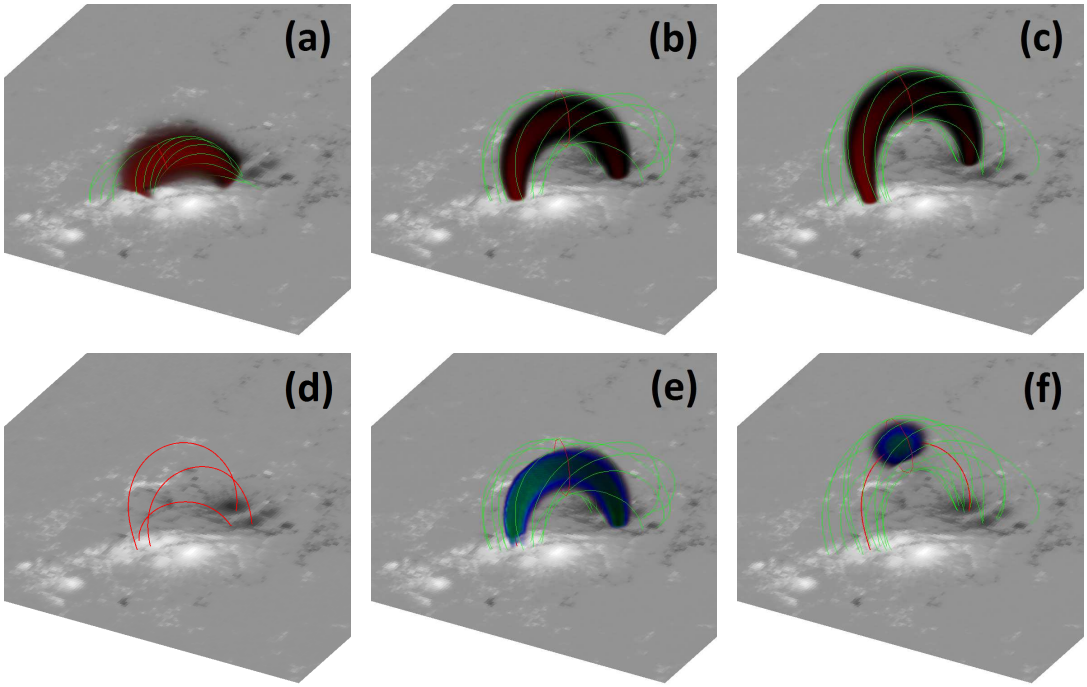

Figure 3.5 The magnetic flux tubes and the corresponding thermal and nonthermal electron populations placed within NLFFF extrapolation cube taken at 18:24 UT, based on the RHESSI image from Figure 3.2. (a) Thermal population occupying the flux tube representing the 6-12 keV source, slightly concentrated at the top of the loop. (b), (c) Thermal population occupying the flux tube representing the 50-75 keV double footpoint sources and 20-35 keV ALT source, respectively. (d) The central field lines of three flux tubes shown together within the model. (e) Nonthermal population occupying the flux tube representing the 50-75 keV double footpoint sources. The footpoint will be enhanced in the model HXR image, since a dense chromosphere (not shown) will be included in the final calculation. (f) Nonthermal population occupying the flux tube representing the 20-35 keV ALT HXR source, highly concentrated at the top of the loop. The nonthermal population for the flux tube (a) is not shown because this loop is assigned with extremely low nonthermal electron density, assuming that it is dominated by thermal electrons. Note that color hues are used only for visual purpose and are scaled individually for each plot.

about an order of magnitude lower than the value assigned for thermal-only loop. For the temperature, we assign 20 MK, but this value is not strictly constrained since the emission measure is solely constrained by the thermal-only loop. We therefore consider the allowable range for the temperature later. Its nonthermal electron spatial distribution was defined as a single Gaussian function slightly off-centered from the loop-top, and was fine-tuned to have 1.9 $\times 10^6$ cm^{-3} at the top and 1.3 - 1.4 $\times 10^6$ cm^{-3} at the bottom of the loop (slightly higher for western FP). For energy distribution, we kept the lower cutoff energy of 22.1 keV from OSPEX, and used the single power-law spectrum with the spectral index of 3.1 extending up to 10 MeV, in order simultaneously reproduce the observed HXR photon spectrum and the negative spectral slope in the high frequency part of the observed MW spectrum. This modification should be well justified since the accuracy of δ_2 predicted by OSPEX is doubful, E_{bk} being well above the energy range of the spectral fitting (12-76 keV).

The third flux tube, Figure 3.5(c) and (f) (right column), is the one representing the 20-35 keV ALT source, with thermal electrons uniformly distributed (Figure 3.5(c)) and nonthermal electrons highly concentrated near the highest point of the loop (Figure 3.5(f)), which is ∼27,300 km above from the photosphere. We call this loop "Higher loop". We assign the thermal population of this loop the same parameters as the lower loop ($T = 20$ MK and $n_{thermal} = 5.0 \times 10^9$ cm^{-3}). However, the density of the nonthermal electrons concentrated at the loop-top is set to be much higher than that of the lower loop, 6.5 $\times 10^8$ cm^{-3}. This high density is required to make the ALT source intensity competitive to the footpoint emissions produced by the lower loop, which are innately bright due to the interaction of their nonthermal particles with the dense chromosphere. Furthermore, we found that this dense source has to be concentrated energetically as well, since the ALT source does not appear at all in 50-75 keV image. This required the nonthermal energy distribution to have a double power-law with a softening break of +3.2 at 43 keV.

Figure 3.6 shows the comparison between the observed and the modeled image contours in three HXR photon energy ranges, resulting from the model of these three loops. Figure 3.7 shows their contributions (pink, blue, and green), compared to the observed HXR photon spectrum from RHESSI (black). It is evident that the HXR model is complete with the combination of three loops.

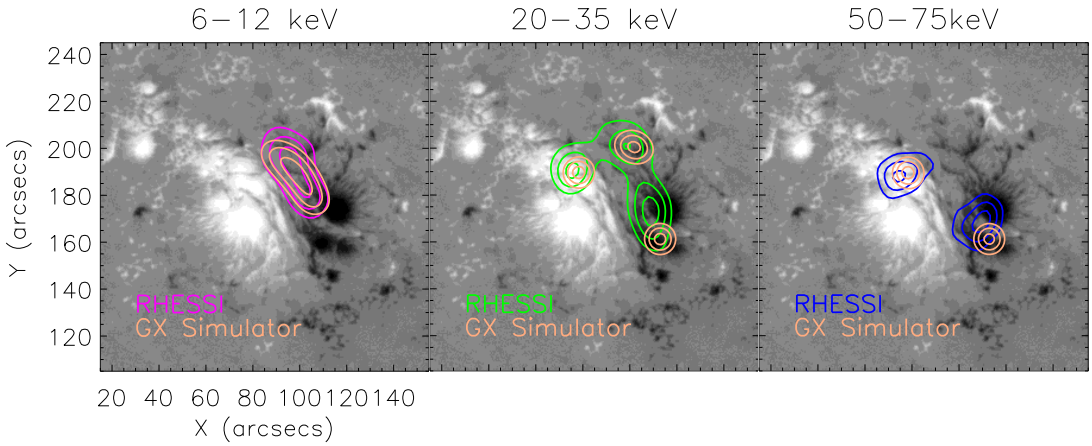

Figure 3.6 The comparison between the observed and the modeled image contours (50, 70, and 90 %) in three HXR photon energy ranges. The observed image contours are the same as Figure 3.2. The model images are produced as pixelated images by the simulator, so they are further convolved with a Gaussian point-spread-function with the size according to the nominal FWHM resolution of the finest RHESSI collimator used in image reconstruction (collimator 3; 6.79 arcseconds).

3.4.2 Constraining in MW

Next, we must test this HXR-constrained model in MW. Figure 3.8 shows the contributions from the three HXR-producing loops in MW (pink, blue, and green), compared to the observed MW total intensity spectrum from EOVSA (black). It is clear that the total MW emission from these three loops does not completely fill the spectrum, especially in the low frequency part. The total area of the HXR-constrained model is too small to reproduce the observed MW emission intensity in this region. Therefore, we considered the existence of another flux tube and its associated electron population that emits mostly in the low frequency MW range, but is "HXR invisible",

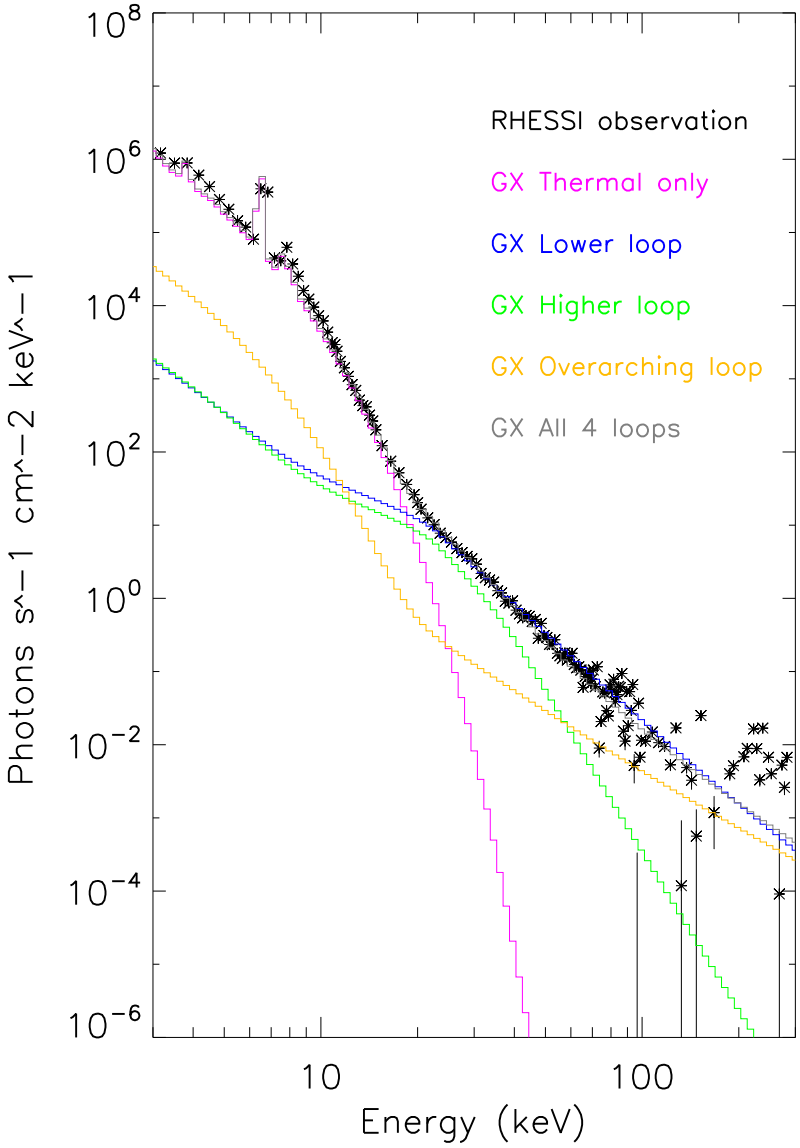

Figure 3.7 The comparison between the observed and the modeled HXR photon spectra, with the breakdown of the contributions from each of four loops in the final model. Grey curves are the emission from the model comprising all four loops in one volume. The slight excess of the HXR emission from the model lower loop compared to the emission from all four loops combined ($\gtrsim 40$ keV) is due to the simulator's voxel ownership implementation, which is confirmed to be negligible (see Section 3.4.2).

i.e., does not emit significantly in HXR. This is the last "overarching loop" that we investigated. This source cannot be created by a thermal population since it would require a high density that will violate the emission measure already constrained in the HXR simulation. Therefore, this source must be created by nonthermal populations. For the GS emission from nonthermal particles to fill the low frequency part of the spectrum, first, the magnetic field strength has to be relatively weak to lower the peak frequency. Second, the nonthermal particle density may be relatively low since it is not detected in HXR. Consequently, third, the area of the source must be relatively large in order to compensate the deficit created by such low particle density. Considering all of these conditions, we created a flux tube that is located above the HXR emitting loops and has ∼10-12 times larger volume than the two other nonthermal loops. Figure 3.9 shows our final four-loop model that includes HXR-constrained three loops and MW-constrained overarching loop. We initially assigned to the overarching loop the identical thermal particle population as the other two loops (T = 20 MK and $n_{thermal} = 5.0 \times 10^9$ cm^{-3}). Fine-tuning this model loop requires the use of the relative visibility plots from Figure 3.3, and after several iterations (including the second fine-tuning in HXR, in both images and spectrum), we obtain a nonthermal population that has the density of 5.7 $\times 10^6$ cm^{-3} concentrated at the intermediate height of the loop, where the magnetic field is weak. The concentrated density spatial distribution was required by the characteristic source size constraint derived from the observed relative visibilities. The relative location of this population within the flux tube, which is close to the three HXR-emitting loops (Figure 7, right), suggests that this population may have been part of the population occupying the HXR-emitting loops but was transported and was accumulated in the region of weaker magnetic field. Its nonthermal energy distribution is found to have a spectral index of 2.0, if we assume a single power-law, and a cutoff energy of 22.1 keV like the other two nonthermal loops. Figure 3.10 shows the comparison between the $\ln(V_{Rel})$ vs. B_λ^2

plots from the EOVSA observation and that calculated from the model. It is evident that the slopes of the model plots are in reasonable agreement with those of the observation in both baselines with different orientation angles, validating that our model is successfully reproducing the observed source size in two different directions. A slight size difference between the model and the observation in the shorter baseline (right plot) is calculated to be about 4 arcseconds.

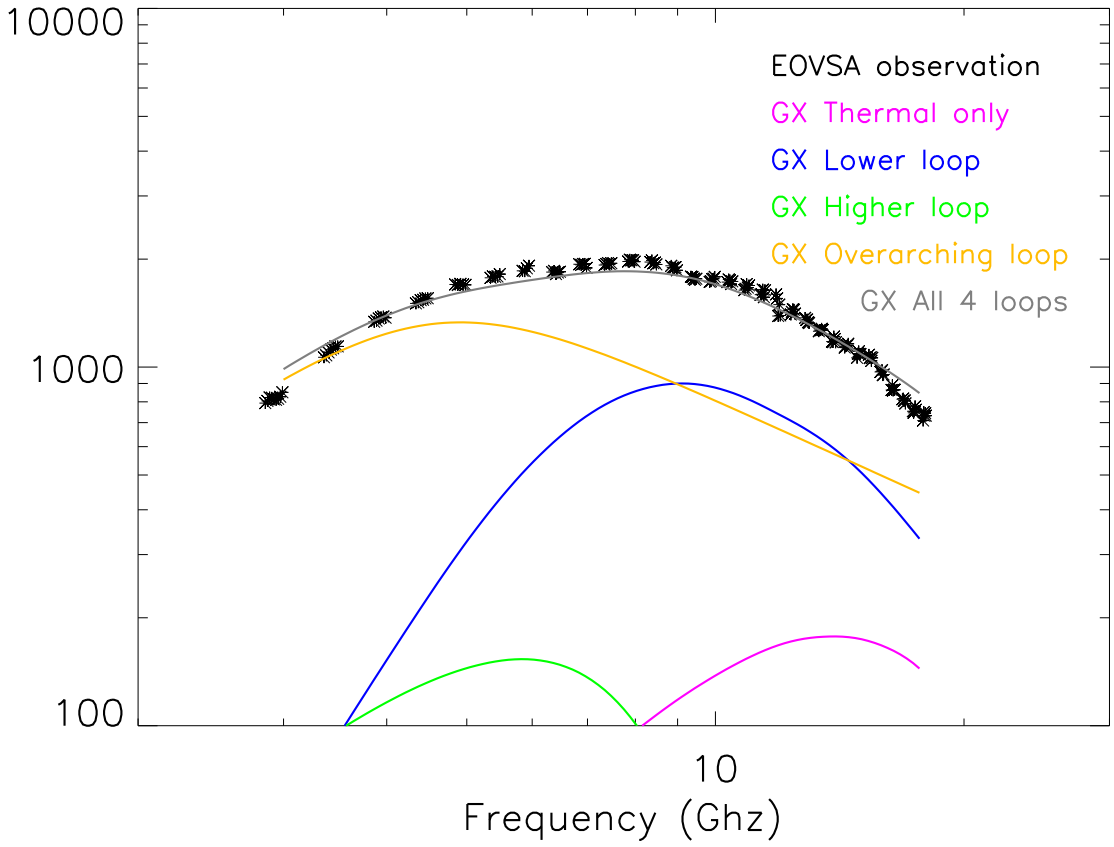

Figure 3.8 The comparison between the observed and the modeled MW total integrated flux density spectra, with the breakdown of the contributions from each of four loops in the final model. Grey curves are the emission from the model comprising all four loops in one volume.

The HXR emission contribution from this loop is evidently lower than the other two loops (Figure 3.7, yellow), and it is so compared to the lower loop because of the difference in the plasma density of the two source regions: 10^{13}

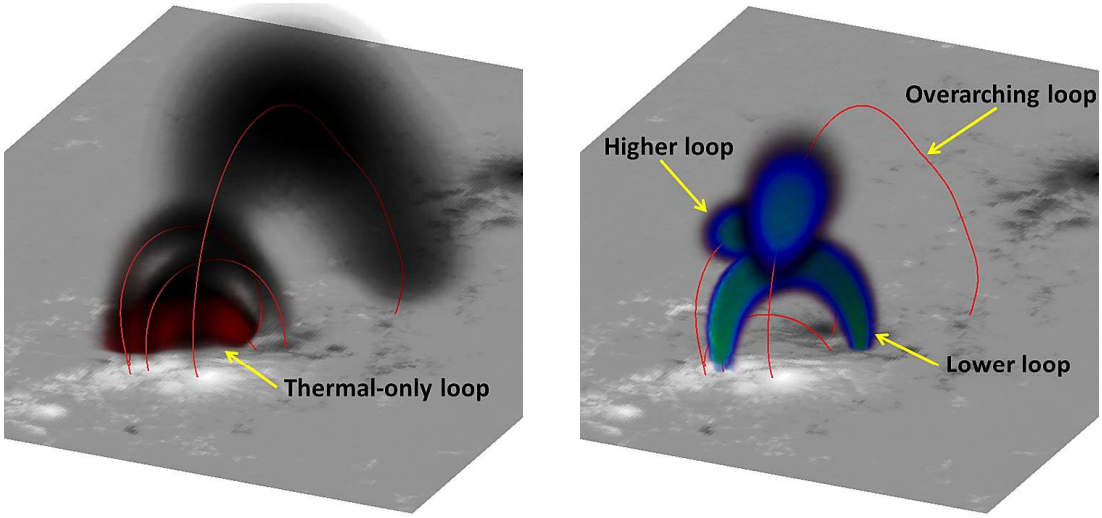

Figure 3.9 The visual representation of thermal (left) and nonthermal (right) electron populations occupying four loops found in the final model. The base image is the HMI photospheric magnetogram taken at 18:24 UT, and the red lines are the central field lines of four loops. The color hues are not in actual density scale. The detailed electron parameters for each named loop are shown in Table 3.2.

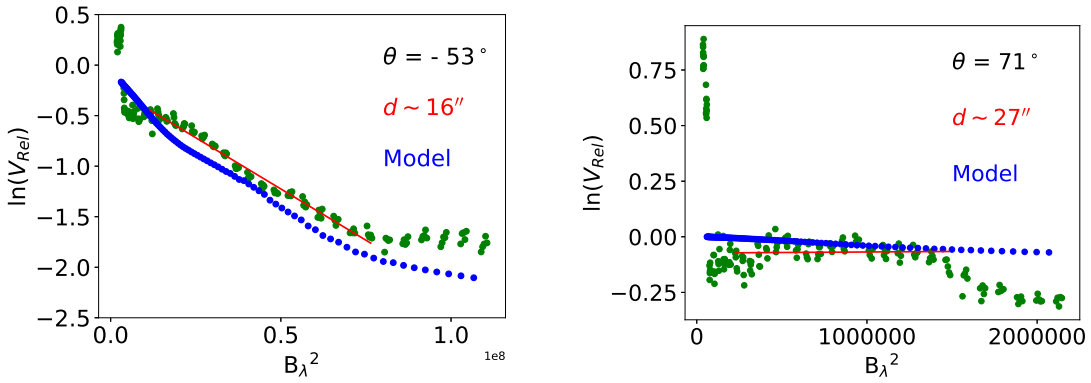

Figure 3.10 The comparison between the $\ln(V_{Rel})$ vs. B_λ^2 plots from the observation (green) and from the model (blue). The model visibility was obtained by convolving the visibility of the pixelated model image from the simulator with the sampling function of the EOVSA array at the modeling time. The slope of the model plot is in reasonable agreement with that of the observation. A slight size difference between the model and the observation in the shorter baseline (right) is calculated to be about 4 arcseconds.

cm^{-3}, chromosphere, for the lower loop, and 5.0 $\times 10^9$ cm^{-3}, high corona, for the overarching loop. Compared to the higher loop, on the other hand, the emission is smaller in the overarching loop simply due to the lower nonthermal particle density; both populations are concentrated within the coronal part of the loop, but the higher loop has 10^8 cm^{-3} nonthermal electrons while the overarching loop has 10^6 cm^{-3} nonthermal electrons. The modeled emission intensity from the overarching loop is lower than the observed emission intensity by an order of magnitude or more for most of the statistically significant energy range (less than $\sim$76 keV), and this may be the reason why this source is "invisible" in HXR, as the dynamic range of RHESSI is about 10 (Saint-Hilaire & Benz 2002; Hurford et al. 2002). We note that the total emission from all four loops combined (grey curve) is slightly less than the sum of the emission from individual loops (other colors). This is because the model comprising all four loops is a complex system with several loops crossing with each other, and in such cases the simulator is designed to calculate the emission with a physically reasonable approximation that the voxels of higher nT pressure dominate the contribution in the total emission. In this model, the thermal-only loop is partially intercepting one of the footpoints of the lower loop, and since the former has higher emission measure (thus higher nT) than the latter and has virtually no nonthermal particles, the emission from the lower loop in the combined model is slightly suppressed in the intercepted footpoint. This effect is also confirmed to be negligible in MW.

3.4.3 Possible Ranges of The Modeled Parameters

We now discuss the possible ranges of some of the modeled electron parameters that were not strictly constrained in the model construction process presented above. First, the density and the temperature of the thermal population for the three nonthermal loops (the higher, the lower, and the overarching loops) are not strictly constrained since the emission measure of the entire model is solely constrained by the thermal-

only loop. We obtain the ranges for the density and the temperature by fixing one of the two parameters at the values assigned during the model construction and varying the other (the target parameter) until the noticible changes start to appear in the spatially integrated HXR model spectrum or images. We separately test the overarching loop and the combination of the lower and the higher loops, since their effective volumes are largely different. For the combination of the lower and the higher loops, we find the upper limit of the temperature to be ∼50 MK, at which the thermal bremsstrahlung starts to appear in the 20-35 keV image, violating the observation. For density, we find the upper limit of $\sim 6 \times 10^{10}$ cm^{-3}, at which the thermal bremsstrahlung from the two loops starts to appear in the 6-12 keV images, violating the observation. For the overarching loop, these limits are more restricted since the emitting volume is larger, and we find the upper limit of the temperature to be ~ 30 MK and of the density to be $\sim 10^{10}$ cm^{-3}. We find virtually no lower limit for the two parameters since any emission measure values below the observational constraint is allowed for these loops.

For the nonthermal population, the density of the higher loop and the minimum energy of the overarching loop are not strictly constrained. For the higher loop, we must consider the lower limit for the nonthermal density corresponding to the upper limit for the thermal density, to keep the same level of nonthermal bremsstrahlung emission. We calculate the lower limit to be $\sim 5.2 \times 10^{7}$ cm^{-3}. The upper limit should be that of the thermal density, $\sim 6 \times 10^{10}$ cm $^{-3}$. For the overarching loop, the electron spectrum was modeled only in the MW range, and since the effective energy of the MW-emitting electrons is above several hundred keV, the spectrum below this energy cannot be strictly constrained. We obtain the more strictly constrained energy range and the number density by testing several different values of cutoff energy and the corresponding normalized number density. As a result, we find that at least 4

$\times 10^4$ cm^{-3} nonthermal electrons above $E_{cutoff} \sim 600$ keV are needed to match the low-frequency MW observations.

Table 3.2 summarizes the spatial and energetic parameters of each loop and their thermal and nonthermal electron populations, with possible ranges for the unconstrained parameters discussed above shown in red. We would also like to mention that, since this simulation is a forward-fitting simulation, there could be other "solutions" of flux tubes that can equally reproduce the observed HXR and MW emissions (even more than four loops). In this respect, we consider our model to be a "minimally optimized" flux tube model, and believe that our methodology, which starts from the construction of the model based on the HXR observation, was the best approach in obtaining a simultaneous fit to the observational constraints that were available for this event. Also, we coincidentally found several remote brightenings in an AIA 1600 $\AA$ channel image taken at the modeling time that correspond to the western footpoints of the overarching loop in our model, as seen in Figure 3.11 (yellow arrows). This correspondence could be interpreted as the signature of the precipitation of the nonthermal particles in the overarching loop into the chromosphere. The fact that the brightenings appear only at the western end of the loop may be due to the large difference in the magnetic field strength (thus the mirror ratio) at the two ends: they are ~2,000 G and ~1,000 G at the eastern and western end, respectively, and only the magnetically weaker end is allowing the particles to precipitate through. The fact that the locations of these remote brightenings closely match with the furthest end of the model loop strongly supports that the size and the extent of our overarching loop is correctly representing the actual flaring loop. For the possible variation in the HXR-constrained model, we briefly consider how our model may vary if we interpret that the 20-35 keV ALT source is a thermal source, as mentioned in the introduction. We find that modeling the 20-35 keV ALT source with $n_{thermal} \sim 10^{10}$ cm^{-3} and $T \sim 60$ MK can equally

produce the observed HXR images and spectrum without violating observed emission measure. However, we find that, in this model, the total number of electrons contained in the volume of the overarching loop exceeds that contained in the total volume of the HXR-emitting loops. This model therefore requires an additional source of the nonthermal electrons into the overarching loop other than the HXR-emitting loops. Thus, we believe that our model with the nonthermal interpretation of the HXR ALT source is more self-consistent and allows more straightforward physical interpretation.

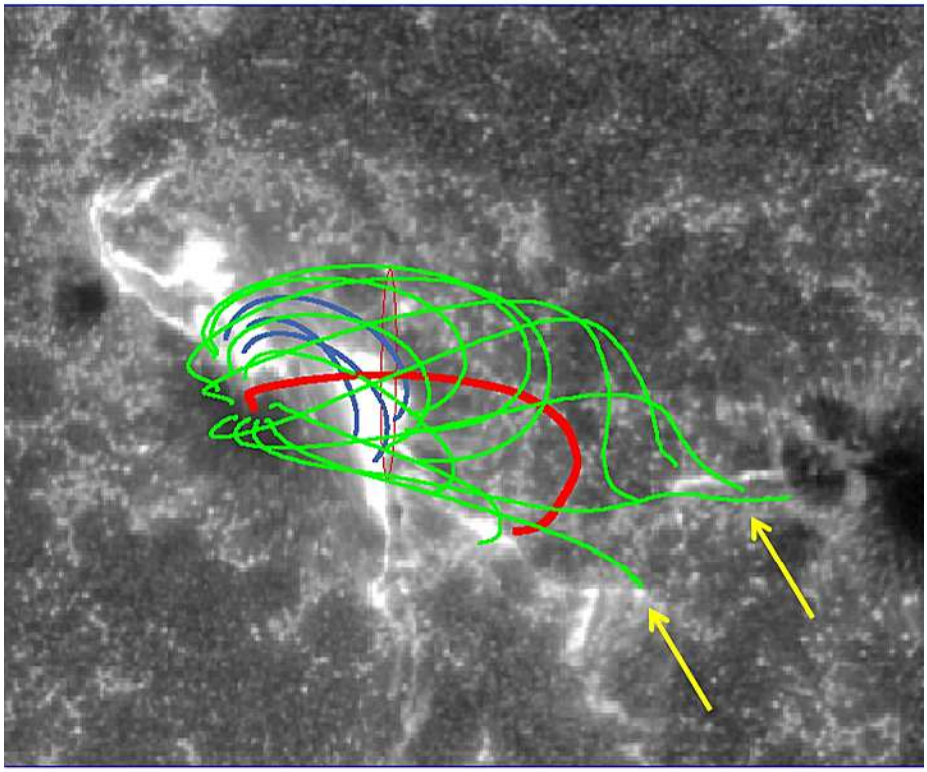

Figure 3.11 The top view of our four loop model overlayed on AIA 1600 $\mathring{A}$ image taken at 18:05:28 UT. The blue lines are the central guiding field lines of the three HXR-constrained loops, the red line is the central guiding field line of the overarching loop, and the green lines are the enveloping field lines of the overarching loop. The red thin ellipse in the middle is the top view of the circular cross section of the overarching loop, defining the extent of green field lines. Only the field lines contained in the overarching loop are shown. The western end of this loop seems to match the locations of the remote brightenings indicated by the yellow arrows, which can be interpreted as the precipitation of the nonthermal electrons into the chromosphere on the magnetically weaker side of this loop.

Table 3.2 Summary of the Modeled Parameters for all four Loops in the Final Model. The Values that Have Possible Ranges are Indicated In Red, and The Ranges Are Shown In The Footnotes.

	Thermal-only loop	**Lower loop**	**Higher loop**	**Overarching loop**
Loop radius (gridpoints)	5	10	10	23
(B_{min}, B_{max}) (G)	(856, 1925)	(401, 1847)	(250, 1984)	(85, 2225)
Thermal density (cm^{-3})	1.1-1.6 $\times 10^{11}$	5.0×10^{9}[b], uniform[a]	5.0×10^{9}[b], uniform[a]	5.0×10^{9}[b], uniform[a]
Tempearture (MK)	20	20[b]	20[b]	20[b]
Nonthermal density (cm^{-3})	0	1.3-1.9 $\times 10^{6}$	6.5×10^{8}[c], concentrated	5.7×10^{6}[d], concentrated
E_{cutoff} (keV)	-	22.1	22.1	22.1[d]
δ_1	-	3.1	3.1	2.0
E_{bk} (keV)	-	-	43	-
δ_2	-	-	6.3	-
E_{max} (keV)	-	10,000	10,000	10,000
Pitch-angle distribution	-	isotropic	isotropic	isotropic

[a] "Uniform" means that the vertial distribution follows a simple hydrostatic formula adapted from §3.1 of Aschwanden (2004); $n_z[z/R] = exp[(-z/R)/(6.7576 \times 10^{-8}T)]$ where z is the distance from the solar surface, R is the solar radius, and T is the constant flux temperature defined in the next row (Nita et al. 2015). The density becomes lower toward the looptop and difference within the loop becomes larger as the loop height increases. However, in this model such differences were confirmed to be negligible (the largest difference was ~6% for overarching loop).

[b] **The lower and the higher loop: $T < 50$ MK and $n_{thermal} < 6 \times 10^{10}$ cm $^{-3}$. The overarching loop: $T < 30$ MK and $n_{thermal} < 10^{10}$ cm^{-3}.** The thermal parameters for this loop are not strictly constrained since the emission measure is solely constrained by the thermal-only loop. See section 3.4.3 for details.

[c] **Range: $\sim 5.2 \times 10^{7} < n_{nonthermal} < 6 \times 10^{10}$ cm^{-3}.** The lower limit is considered based on the upper limit of the thermal density, while the upper limit is equal to the upper limit of the thermal density. See section 3.4.3 for details.

[d] **Range: $E_{cutoff} > 600$keV and $4 \times 10^{4} < n_{nonthermal} < 5.7 \times 10^{6}$ cm^{-3}.** The nonthermal electron energy spectrum for this loop cannot be constrained under several hundred keVs since the emission from this loop is only visible in the MW low-frequency range. See Section 3.4.3 for details.

3.5 Discussion and Conclusions

Based on these results, we draw the following conclusions about the spatial and the energetic distributions of the energetic electrons producing HXR and MW emissions at the end of the impulsive phase of 2015-06-22 M6.5 flare.

First, based on the observed HXR emission sources, the magnetic field configuration that best represents the flaring loop geometry in our study was found to be the post-reconnection loop configuration. We compared the field line connectivity of the NLFFF extrapolation cube created near the modeling time of 18:05:32 UT, and found that field lines contained in the cube created at the earlier time did not have the desired connectivity for our observed HXR sources due to its sheared overall field line geometry. It is evident that our modeled peak has not started at 18:00 UT yet (see Figure 3.1), so it is reasonable to think that the shear reduced due to the reconnection event responsible for our modeled peak. The chosen cube at 18:24 UT should contain more post-reconnection loops, and although the field model with finer time cadence considering the dynamics of the flaring loop may still improve the accuracy of the model, our results show that this post-reconnection cube can reproduce the relative locations of the observed HXR sources and the characteristic size of the observed MW source well.

Second, the low frequency part of the MW spectrum is dominated by the emission from a "HXR invisible" source containing a non-negligible number of nonthermal electrons in a relatively large volume with relatively weak magnetic field. The nonthermal particle population in the overarching loop fills a volume ∼10-12 times larger than the other two nonthermal loops. As mentioned above, the primary reason that this source is "HXR invisible" although it contains up to 5.7×10^6 cm^{-3} nonthermal electrons is because this source resides in the high corona where n_p is relatively low, and in HXR, the emission from this source is overcome by the bright footpoint emission from the chromosphere with $n_p = 10^{13}$ cm^{-3}. This population

has an interesting nonthermal energy spectrum with the spectral index of 2.0, the hardest of all three nonthermal populations. We interpret this as a result of particle accumulation and trapping at that location above the main loops, caused by some transport process underway throughout the impulsive phase. Such an interpretation is also reasonable if one notices that the low frequency part of the MW spectrum grew over several minutes only toward the end of the impulsive phase, as evident in the 4.43 GHz lightcurve (red) in Figure 3.1. We also note that this result is essentially insensitive to the possible variation in the model parameters of the lower loop, which contributes to the high-frequency part of the spectrum, because the GS emission from the lower loop cannot have much lower peak frequency due to the strong magnetic field strength in the low corona (see Figure 3.8, blue). In other words, the deficit in the low frequency part of the MW spectrum will be present as long as we confine the main HXR loops at lower heights based on the observed HXR images.

Third, the overall geometry and the locations of the electron populations in the three HXR emitting loops in our model fit well within the standard flare model. The thermal-only loop can be interpreted as a result of chromospheric evaporation; dense (10^{11} cm^{-3}) thermal plasma concentrated toward the looptop. It is interesting that this loop was found to lie relatively low, and this may be a result of our choice of the NLFFF magnetic field model from a time (18:24 UT) that is later than 18:05:32 UT, which contains more post-reconnection loops. However, considering that our modeling time is already near the end of the impulsive phase when most of the loops reconnected and became low-lying post-reconnection loops, we consider that our modeled geometry is correctly representing the actual geometry of the flare loops. The spatial and energy distribution of the nonthermal electrons in the lower and the higher loop fits the standard picture as well. The lower loop population produces 50-75 keV HXR footpoint sources and MW high frequency emission, and the higher loop population produces 20-35 keV HXR ALT source. For the lower loop

population, we have to modify the modeled electron spectral index compared with that obtained from the thin-target fit up to a certain energy since the HXR emission from this population is only seen in the footpoint where thick-target model needs to be employed. The modification is the following. The electron flux spectrum, electrons s^{-1} keV^{-1}, which is usually used in thick-target model, can be expressed in electron number density spectrum, electrons cm^{-3} keV^{-1}, which can then be compared to the instantaneous, thin-target model (Brown 1971; Holman et al. 2011; White et al. 2011). After the conversion, the electron number density spectral index δ inferred from the HXR photon spectrum with index γ differs by 2 between thin- and thick-target model: $\delta_{thin} = \gamma - 0.5$ and $\delta_{thick} = \gamma + 1.5$. Thus, we have to soften the modeled spectral index by $\sim$2. This means that the lower loop population has the broken power-law with $\delta_1 = 3.1 + 2 = 5.1$ and $\delta_2 = 3.1$. What is interesting here is that this $\delta_1 = 5.1$ is similar to the dominant spectral index of the ALT source population, $\delta_2 = 6.3$ above 43 keV. Since thick-target model calculates the spectral index of the *injected* electron population, we can combine the higher and lower loop population into a unified picture as the following. First, the 20-35 keV HXR ALT source is produced via thin-target bremsstrahlung by the population with a soft spectrum, $\delta \sim 6.3$. This population keeps streams down in the loop-legs of the lower loop, losing its low-energy end via collisional scattering into the loss-cone, while its high-energy end gets trapped and produces GS emission in the MW high frequency range. Here, this high-energy population must evolve to a much harder spectrum, $\delta \sim 3.1$. The population's low-energy end bombards the chromosphere, and produces thick-target bremsstrahlung radiation that hardens the emitted HXR photon spectrum from $\sim$ 6.3 to $\sim$ 3.1. The question here is where E_{break} is in this broken power-law spectrum. We claim that this is around 300 keV, where the normalized nonthermal electron density of the higher loop population and the lower loop population coincides in the order of 10^4 cm^{-3} keV^{-1}. We cannot test if the

spectral hardening of -3.2 at 300 keV was already present coming out of the ALT source, or because some of the lower energy population moved to the higher energy population via second-stage acceleration that preferentially accelerates higher energy electrons during the propagation and the trapping, or both.

In summary, our results show that our three-dimensional forward-fit modeling of the flare HXR and MW emission can reveal the properties of the nonthermal particles in the flare in much more quantitative detail than those obtained by conventional means, both within and outside of the standard flare model. We would like to emphasize the importance of our finding, the existence of the "HXR invisible" nonthermal particles that can only be investigated through the properties of the MW low frequency emission. This suggestion is not new (e.g., Lee et al. 1994; Fleishman et al. 2016a), but has been largely neglected in the standard flare model because the focus of the flare-accelerated electrons has been mainly in the HXR range (and their counterpart in MW high frequency range) where the bulk of their energy is deposited. Even though these low frequency MW-emitting electrons are still at the "tail" of the electron number distribution, their high energy and the trapped condition may make them an energetically important player in the overall flare energetic scenario, even after the impulsive phase. For instance, these trapped high-energy electrons may escape directly or be further accelerated by CME shocks and become Solar Energetic Particles. Our modeling also stimulates the further investigation into the possible spectral break in the population emitting in both HXR and MW range. Our model for this particular flare seems to support the existence of the break, but other flares may not show such a break. Running this type of modeling for many other flares could lead to the findings of the properties of the flare that may or may not result in a break. Such information should enable us to discriminate among the competing models of flare particle acceleration.

CHAPTER 4

SUMMARY AND FUTURE PERSPECTIVES

The works presented in this dissertation are focused on the study of the high-energy electrons produced during the impulsive phase of two major solar flares, 2011-02-15 X2.2 flare and 2015-06-22 M6.5 flare. We conducted the multi-wavelength analysis and modeling enabled by the unique combinations of the state-of-the-art high-cadence observations and the newly-developed realistic three-dimensional simulation platform. Particularly, the results from the quantitative and spatially-resolved study of the HXR and the MW emission were compared with the current picture of the standard flare model. The major results of each study are the followings.

4.1 The 2011-02-15 X2.2 Flare

In this study, we examined the source locations of seven distinct temporal peaks observed in HXR and MW impulsive phase using the RHESSI 50-75 keV channels and NoRH 34 GHz channel, respectively. This was the first study of this well-observed flare that used the high-cadence HXR and MW observations simultaneously.

1. **The seven peaks came predominantly from two sources in both HXR and MW, each with multiple temporal peaks, suggesting the two separate locations of magnetic reconnection sites.**

   As shown in Figure 2.7 and Figure 2.10, HXR and MW emission sources basically evolve with similar patterns, with the same multiple peaks for each source observed in both wavelengths. The match in temporal and spatial transition between two wavelengths fit to the current picture of the standard flare model; a common population of the electrons accelerated in one reconnection event produce both HXR and MW emission. However, for HXR

the transition between two stages occur rather quickly within ∼30 s, and the first source quickly decays. On the other hand, the MW emission from the first source stays strong until much later and decays more slowly. This difference can be interpreted as the result of the trapping of the MW-emitting electrons.

2. **The MW peaks were found to lag the HXR peaks by 1.9-3.0 s with an uncertainty below 1 s, although these values were found not to be related or dependent on other parameters, thus providing us no clear quantitative relationship between HXR-emitting and MW-emitting components of the accelerated electrons.**

   As shown in Table 2.1, for this flare the meaningful peaks for delay analysis (peak 1, 3, 4, and 7) showed that the MW emission consistently lags the HXR emission by 1.9-3.0s. The delays for the peaks in the second source (3, 4, and 7) were found to increase with the calculated decay times of the MW 17 GHz emission, which is in line with the idea introduced by Gary & Tang (1985), that the HXR-emitting and MW-emitting population share the same acceleration profiles but MW-emitting population gets trapped and thus decays more slowly, which results in the observed delay. However, the decay time profiles become more blended and thus unreliable as the flare progresses. Furthermore, no correlations were found between the delays and such parameters as the MW energies, the peak X-ray or the MW flux or their ratio, the power-law index, or two stages of reconnections. Therefore, no clear quantitative conclusion can be drawn regarding the relationship between the HXR-emitting and MW-emitting populations of the accelerated electrons in this flare, although the trapped nature of the MW-emitting component is qualitatively inferred from the above-mentioned difference in spatial transition between two stages of reconnections.

3. **The two stages of magnetic reconnection can be interpreted as the temporally and the spatially distributed tether-cutting reconnection scenario (Moore et al. 2001).**

   Prior to this study, Wang et al. (2012) found a permanent enhancement of the horizontal field strength at a certain area along the polarity inversion line of this flare site, which was interpreted as the evidence of the collapsing magnetic fields expected from the quadrupolar configuration within the tether-cutting scenario. The location of this field enhancement corresponds to the second source that we observed in this study. Based on the observation of the remote emission source observed in HXR (both in this study and in Wang et al. (2012)), which is also expected in the geometry of the tether-cutting scenario, we concluded that our first source could also be interpreted as the earlier stage of a two-stage tether-cutting scenario. This is an interesting discovery which was not revealed in Wang et al. (2012), which was based on the available vector magnetogram data. Its cadence of 12 minutes, a time-scale comparable to almost the entire duration of the impulsive phase of this flare, was not sufficient to distinguish two stages.

4. **The electron power-law energy spectral indices inferred from the MW observation seems to be harder than usual by $1 \sim 2$ for this flare.**

   The time profile of electron spectral indices inferred from the MW observation of this flare is shown in Figure 2.11. The differences between these and the ones inferred from the HXR observation (from Milligan et al. (2014)) is 3∼4, about 1∼2 larger than usual (∼2). However, since the values inferred from the HXR observation is in the usual range, it seems that the MW-inferred indices are unusually hard for this event. We did not investigate further into the reason behind this unusual hardness.

5. **We observed the emission intensity asymmetry between the HXR and the MW source that is attributed to the asymmetrical magnetic field strengths of the loop, discussed by Sakao et al. (1996) and Wang et al. (1995).**

   After correcting for the possible projection effect on the locations of the observed MW sources and based on the observation of the polarization gradients over the sources, we suggest that there is an asymmetry in the magnetic field strength within the observed MW source, between the opposite sides of the polarity inversion line. The HXR emission from the stronger side was evidently less, which agrees with the idea that stronger mirroring effect impedes the precipitation of the HXR-emitting electrons into the chromosphere.

4.2 The 2015-06-22 M6.5 flare

In this study, we created one unified multi-loop electron population model that can simultaneously reproduce the observed HXR and MW images and spectra at the end of the impulsive phase of the flare, using the three-dimensional multi-wavelength simulation platform *GX Simulator*, a realistic NLFFF magnetic field model, and the observational constraints from the RHESSI and the EOVSA.

1. **The magnetic field configuration that best represents the observed HXR emission sources was found to be the post-reconnection loop configuration.**

   In this study, obtaining a realistic magnetic field model that represents the flaring loop geometry was an important first step. We obtained such a model cube by using the observed HXR images as a guide to locating the field lines with the required connectivity in the NLFFF model extrapolated from the HMI photospheric magnetogram data. As a result, the best cube was found to be from the data taken **after** the time being analyzed, which was at the end of the

impulsive phase when the flaring loops had already closed. Otherwise, the cube does not contain post-reconnection loops corresponding to the flaring loops.

2. **The low frequency part of the observed MW spectrum is dominated by the emission from a "HXR invisible" source containing a non-negligible number of nonthermal electrons in a relatively weak but large magnetic field volume.**

   We found that the electron populations that sufficiently reproduce all of the observed HXR sources and spectrum cannot sufficiently reproduce the observed MW intensity level, especially in the low frequency part of the MW spectrum. We found that a nonthermal electron population with the density up to 5.7×10^6 cm^{-3} contained in a large, weak magnetic loop "overarching" the HXR-emitting loops is needed to explain this discrepancy, while not violating constraints from the observed HXR images or spectrum. The volume of this large loop is ~10-12 times larger than the HXR-emitting nonthermal loops, and we found remote EUV brightenings at the locations corresponding to the footpoints of this large loop, which can be interpreted as the site of precipitation of its nonthermal population into the chromosphere. The hardness of the modeled energy spectrum suggests that this population was most likely transported from elsewhere and became trapped, perhaps accumulating throughout the time of the impulsive phase. Therefore, this population may originate in the acceleration process assumed in the traditional standard flare model, but may contain additional information about the transport, trapping and loss mechanisms of the electrons with $E >$ several hundred keV that have not yet been widely recognized or discussed.

3. **The overall geometry and the locations of the electron populations in the "HXR visible" loops fit well in the standard flare model. The**

thermal population with $T \sim 20$MK and $n_e \sim 10^{11}$cm^{-3} can produce the observed HXR 6-12 keV source, and the nonthermal population having a broken-power law energy spectrum with $E_{break} \sim 300$ keV can produce the observed HXR ALT (20-35 keV) and FP (50-75 keV) sources below E_{break} and the observed MW high frequency source above E_{break}.

The modeled HXR 6-12 keV source can be interpreted as the dense thermal source produced by plasma evaporated from the chromosphere, as several episodes of reconnection caused the particle bombardments and the heat conduction from the corona prior to this modeled peak. The 20-35 keV ALT source can be explained by a dense nonthermal population with soft spectrum in order to be consistent with the observed range of the energy. This population streams down toward the chromosphere, and produce thick-target 50-75 keV FP emission that hardens the observed photon spectrum by ∼2. Meanwhile, the high-energy end of the same population must have a harder spectrum in order to be consistent with the observed high frequency slope of the MW emission. The low-energy end and the high-energy end coincides at $E \sim 300$ keV in the order of 10^4 cm^{-3} keV^{-1}. Therefore, the "common population" of the nonthermal electrons responsible for the HXR and MW emission, in the view of the traditional picture of the standard flare model, must have an upward break in its energy spectrum for this flare. We did not explore the reasons behind the harder spectral index for the MW-emitting component of this population in this study.

4.3 The Summary of The Dissertation

The main goal of this dissertation is to find the relationship between HXR-emitting and MW-emitting electron population in finer details and offer possible solutions

to some of the discrepancies that have been found between the observations made in these two wavelengths. In response to this goal, the major findings of this dissertation are the followings.

1. We found clear evidence of the correlated two stages of magnetic reconnection in 2011-02-15 flare, which can be interpreted as tether-cutting flare scenario that assumes the traditional picture of the HXR-emitting and the MW-emitting electron population in the standard flare model; two populations are accelerated by the energy released in the same magnetic reconnection event. (Chapter 2)

2. In this traditional picture of the two populations in the standard flare model, however, the three-dimensional, spatially-resolved modeling reveals that the broken power-law energy spectrum with different parts of the spectrum emitting at two wavelengths at different parts of flare loop is required. (Chapter 3)

3. Furthermore, there may be a population of trapped nonthermal electrons that has not been discussed in the standard flare model, and this population can be studied through the analysis of MW low frequency emission and may be observed using future HXR instrument with enough dynamic range. (Chapter 3)

4. Time delays in this study did not provide any new findings about the relationship between two electron populations. For future studies of the same kind, less complicated flare that allows more accurate calculation of the MW decay time constant may be more appropriate. (Chapter 2)

4.4 Future Perspectives

We will introduce in below the possible directions of the future research, motivated by the research in this dissertation.

- The continuation and the expansion of the modeling research using the GX simulator, much like the one introduced in Chapter 3, is promising. Particularly, modeling at several different times during the flare will enable us to model the temporal evolution of the energy and the evolving locations of the nonthermal electrons. This will help us explore the particle transport process in realistic three-dimensional nature. Also, one aspect of the modeling that can be improved is the accuracy of the magnetic field model during the flare. Our current use of 12-minutes cadence NLFFF model may not represent the highly dynamic flaring morphology accurately enough. A magnetic field model developed through MHD simulation (e.g., as performed by Inoue et al. (2014) for our first event) is one approach that could be used for this purpose.

- The formation and the decay of the large "HXR invisible" population of nonthermal electrons may be directly observed and modeled. The relationship between this population and the SEPs can be explored; e.g., by estimating the energy spectrum of SEP electrons from the modeled trapped electron spectrum and the possible geometry of the observed CME shock.

- With the full operation of the EOVSA in our site, the study of the high-energy end of the flare-accelerated electrons will be greatly advanced, with possible new discoveries. The 1s-cadence images may be used to study the rapidly evolving impulsive phase, and as the observational constraint to evaluate the performance of the aforementioned MHD simulation.

- The nature and the physics behind the spectral break in the nonthermal electron population, found in our modeling (Chapter 3), should be explored further, with spatially resolved MW spectra from EOVSA. Kontar et al. (2007) found that the break in the HXR photon spectrum can be explained by the contribution from the electron-electron bremsstrahlung (thus the true electron energy spectrum

does not require a break), which is not yet included in the X-ray code used in the GX simulator. Although the difference in the spectral indices found in our modeling is much larger than the one studied in Kontar et al. (2007) ($\sim$3.2 and 0.5, respectively), it is interesting to look at this effect. The statistical study using the same modeling scheme over many other flares may reveal some relationship between the parameters of the modeled electron distribution (e.g., E_{break}, partition of the total number of nonthermal electrons) and the properties of the flare site (e.g., magnetic field geometry) that can help us constrain the particle acceleration mechanism.

The study of the flare-accelerated electrons will greatly contribute to the advance of space weather research in many ways. Understanding of the particle acceleration mechanism is one of the most important subjects in solar physics, as it possibly leads to the prediction of the energy and the number of nonthermal particles produced in flares. This information can further be used to model the response of the chromospheric plasma that appears in the SXR range, which is the operational measure of the flare intensity, as introduced in the beginning. The knowledge of the particle acceleration mechanism may be applicable to the phenomena observed in Earth's magnetotail, where the magnetic reconnection and the particle acceleration are also suspected to occur. Also, as stated above, the prediction of SEP electrons (and possibly ions as well, if we could constrain the particle acceleration mechanism in the event), directly contributes to the benefits of our society, as SEPs are known to be hazardous. In summary, the works introduced in this dissertation are directly applicable within the larger context of the space weather research, and motivate the further exploration into the subject of flare-accelerated electrons.

APPENDIX

DERIVATION OF RELATIVE VISIBILITIES

Visibility on a particular baseline is defined as the Fourier transform of the sky brightness distribution. Let us assume a simple Gaussian source flux function:

$$S(x) = ae^{\frac{-(x-x_0)^2}{\alpha^2}} \tag{1}$$

where $S(x)$ is the flux intensity as a function of spatial coordinate x, a is a unit amplitude at $x = x_0$, and α is the 1/e width of the unit amplitude (half power beam width). Then the visibility as a function of spatial frequency s (x/λ) is

$$V(s) = \int_{-\infty}^{\infty} S(x)e^{-2\pi isx}dx = ae^{-x_0^2/\alpha^2}e^{(\frac{x_0}{\alpha^2}-\pi is)^2}\alpha^2 \int_{-\infty}^{\infty} e^{-[\frac{x}{\alpha}-\alpha(\frac{x_0}{\alpha^2}-\pi is)]^2}$$

$$= a\sqrt{\pi}\alpha e^{-\pi^2 s^2\alpha^2}e^{-2\pi ix_0 s} \tag{2}$$

Relative visibility is defined as the visibility divided by the total power $(s \to 0)$,

$$V_{Rel} = \frac{V(s)}{V(0)} = e^{-\pi^2 s^2\alpha^2} \tag{3}$$

where V_{Rel} is a unit amplitude $(x_0 = 0)$. Plugging in the definition of spatial frequency s and the conversion factor between α and the FWHM of the source, d,

$$s = \frac{1}{\theta}rad^{-1} \sim B_\lambda rad^{-1} = \frac{B_{cm}f_{GHz}}{30}rad^{-1}$$

$$= -8.351 \times 10^{-11}B_\lambda^2 arcsec^{-1} = 1.62 \times 10^{-7}B_{cm}f_{GHz}arcsec^{-1}$$

$$\alpha \sim 0.6d$$

(A3) becomes

$$V_{Rel} = e^{-8.351\times10^{-11}B_\lambda^2 d^2} = e^{-9.325\times10^{-14}B_{cm}^2 d^2 f_{GHz}^2} \tag{4}$$

where θ is the fringe spacing, B_λ is the projected baseline length in number of wavelength, B_{cm} is the projected baseline length in cm, f_{GHz} is the observing frequency in GHz, and d is in arcsec. Note that V_{Rel} here is a unit amplitude ($x_0 = 0$). In practice, $V(s)$ is the cross-correlated amplitude from a particualr baseline and $V(0)$ is the geometric mean of the total power from the two antennas on that baseline. That is,

$$V_{Rel} = \frac{a_{ij}}{\sqrt{a_{ii}a_{jj}}} \tag{5}$$

where a_{ij} is the cross-correlated amplitudes from the baseline consisting of antenna i and j, and a_{ii} and a_{jj} are the auto-correlated total power amplitudes from antenna i and j, respectively. Combining (A4) and (A5), we have

$$V_{Rel} = \frac{a_{ij}}{\sqrt{a_{ii}a_{jj}}} = e^{-8.351\times10^{-11}B_\lambda^2 d^2} = e^{-9.325\times10^{-14}B_{cm}^2 d^2 f_{GHz}^2} \tag{6}$$

or

$$\ln(V_{Rel}) = \ln(\frac{a_{ij}}{\sqrt{a_{ii}a_{jj}}}) = -8.393\times10^{-11}B_\lambda^2 d^2 = -9.325\times10^{-14}B_{cm}^2 d^2 f_{GHz}^2 \tag{7}$$

BIBLIOGRAPHY

Allen, C. W. 1973, Astrophysical quantities

Arzner, K. 2004, Inverse Problems, 20, 1729

Asai, A., Kiyohara, J., Takasaki, H., Narukage, N., Yokoyama, T., Masuda, S., Shimojo, M., & Nakajima, H. 2013, Astrophysical Journal, 763, 87

Aschwanden, M. J., Dennis, B. R., & Benz, A. O. 1998, Astrophysical Journal, 497, 972

Aschwanden, M. J., Schwartz, R. A., & Alt, D. M. 1995, Astrophysical Journal, 447, 923

Bai, T., & Ramaty, R. 1978, Astrophysical Journal, 219, 705

Bastian, T. S., Benz, A. O., & Gary, D. E. 1998, Annual Review of Astronomy and Astrophysics, 36, 131

Benz, A. O. 2017, Living Reviews in Solar Physics, 14, 2

Brown, J. C. 1971, Solar Physics, 18, 489

Carmichael, H. 1964, NASA Special Publication, 50, 451

Cliver, E. W., & Dietrich, W. F. 2013, Journal of Space Weather and Space Climate, 3, A31

Cornell, M. E., Hurford, G. J., Kiplinger, A. L., & Dennis, B. R. 1984, Astrophysical Journal, 279, 875

Crosby, N. B., Aschwanden, M. J., & Dennis, B. R. 1993, Solar Physics, 143, 275

Dennis, B. R. 1988, Solar Physics, 118, 49

Dulk, G. A. 1985, Annual Review of Astronomy and Astrophysics, 23, 169

Emslie, A. G., Fennelly, J. A., & Machado, M. E. 1986, Advances in Space Research, 6, 139

Fleishman, G. D., Anfinogentov, S., Loukitcheva, M., Mysh'yakov, I., & Stupishin, A. 2017, Astrophysical Journal, 839, 30

Fleishman, G. D., & Kuznetsov, A. A. 2010, Astrophysical Journal, 721, 1127

Fleishman, G. D., & Melnikov, V. F. 2003, Astrophysical Journal, 587, 823

Fleishman, G. D., Pal'shin, V. D., Meshalkina, N., Lysenko, A. L., Kashapova, L. K., & Altyntsev, A. T. 2016a, Astrophysical Journal, 822, 71

Fleishman, G. D., Xu, Y., Nita, G. N., & Gary, D. E. 2016b, Astrophysical Journal, 816, 62

Forbes, T. G. 2000, Journal of Geophysical Research, 105, 23153

Gary, D. E., Fleishman, G. D., & Nita, G. M. 2013, Solar Physics, 288, 549

Gary, D. E., & Hurford, G. J. 1990, Astrophysical Journal, 361, 290

Gary, D. E., & Keller, C. U., eds. 2004, Astrophysics and Space Science Library, Vol. 314, Solar and Space Weather Radiophysics - Current Status and Future Developments

Gary, D. E., & Tang, F. 1985, Astrophysical Journal, 288, 385

Ginzburg, V. L., & Syrovatskii, S. I. 1969, Annual Review of Astronomy and Astrophysics, 7, 375

Gopalswamy, N. 2004, in Astrophysics and Space Science Library, Vol. 317, The Sun and the Heliosphere as an Integrated System, ed. G. Poletto & S. T. Suess, 201

Guo, J., Emslie, A. G., Massone, A. M., & Piana, M. 2012, Astrophysical Journal, 755, 32

Hanaoka, Y. 1996, in Astronomical Society of the Pacific Conference Series, Vol. 111, Astronomical Society of the Pacific Conference Series, ed. R. D. Bentley & J. T. Mariska, 200–205

Hanaoka, Y. 1997, Solar Physics, 173, 319

Hanaoka, Y., et al. 1994, in Proceedings of Kofu Symposium, 35–43

Haug, E. 1997, Astronomy and Astrophysics, 326, 417

Hirayama, T. 1974, Solar Physics, 34, 323

Holman, G. D., et al. 2011, Space Science Reviews, 159, 107

Hudson, H. S. 2011, Space Science Reviews, 158, 5

Hurford, G. J., et al. 2002, Solar Physics, 210, 61

Inoue, S., Hayashi, K., Magara, T., Choe, G. S., & Park, Y. D. 2014, Astrophysical Journal, 788, 182

Ishikawa, S., Krucker, S., Takahashi, T., & Lin, R. P. 2011, Astrophysical Journal, 737, 48

Jeffrey, N. L. S., & Kontar, E. P. 2013, Astrophysical Journal, 766, 75

Jing, J., Xu, Y., Cao, W., Liu, C., Gary, D., & Wang, H. 2016, Scientific Reports, 6, 24319

Kane, S. R. 1974, in IAU Symposium, Vol. 57, Coronal Disturbances, ed. G. A. Newkirk, 105–141

Kerr, G. S., & Fletcher, L. 2014, Astrophysical Journal, 783, 98

Kontar, E. P., Emslie, A. G., Massone, A. M., Piana, M., Brown, J. C., & Prato, M. 2007, Astrophysical Journal, 670, 857

Kopp, R. A., & Pneuman, G. W. 1976, Solar Physics, 50, 85

Krucker, S., & Battaglia, M. 2014, Astrophysical Journal, 780, 107

Kundu, M. R., Grechnev, V. V., White, S. M., Schmahl, E. J., Meshalkina, N. S., & Kashapova, L. K. 2009, Solar Physics, 260, 135

Kundu, M. R., Schmahl, E. J., & Velusamy, T. 1982, Astrophysical Journal, 253, 963

Kundu, M. R., White, S. M., Gopalswamy, N., & Lim, J. 1994, Astrophysical Journal, Supplement, 90, 599

Kushwaha, U., Joshi, B., Cho, K.-S., Veronig, A., Tiwari, S. K., & Mathew, S. K. 2014, Astrophysical Journal, 791, 23

Kuznetsov, A. A., & Kontar, E. P. 2015, Solar Physics, 290, 79

Lee, J., & Gary, D. E. 2000, Astrophysical Journal, 543, 457

Lee, J. W., Gary, D. E., & Zirin, H. 1994, Solar Physics, 152, 409

Lemen, J. R., et al. 2012, Solar Physics, 275, 17

Lin, J., & Forbes, T. G. 2000, Journal of Geophysical Research, 105, 2375

Lin, R. P., et al. 2002, Solar Physics, 210, 3

Litvinenko, Y. E. 1996, Astrophysical Journal, 462, 997

Liu, C., et al. 2016, Nature Communications, 7, 13104

Masuda, S., Kosugi, T., Hara, H., Tsuneta, S., & Ogawara, Y. 1994, Nature, 371, 495

Melrose, D. B. 1980, Plasma astrohysics. Nonthermal processes in diffuse magnetized plasmas - Vol.1: The emission, absorption and transfer of waves in plasmas; Vol.2: Astrophysical applications

Melrose, D. B., & Brown, J. C. 1976, Monthly Notices of the RAS, 176, 15

Milligan, R. O., et al. 2014, Astrophysical Journal, 793, 70

Moore, R. L., Sterling, A. C., Hudson, H. S., & Lemen, J. R. 2001, Astrophysical Journal, 552, 833

Nakajima, H., Sekiguchi, H., Sawa, M., Kai, K., & Kawashima, S. 1985, Publications of the ASJ, 37, 163

Nakajima, H., et al. 1994, IEEE Proceedings, 82, 705

National Science and Technology Council. 2015, National Space Weather Action Plan

Neupert, W. M. 1968, Astrophysical Journal, Letters, 153, L59

Nishio, M., Yaji, K., Kosugi, T., Nakajima, H., & Sakurai, T. 1997, Astrophysical Journal, 489, 976

Nita, G. M., Fleishman, G. D., Kuznetsov, A. A., Kontar, E. P., & Gary, D. E. 2015, Astrophysical Journal, 799, 236

Nita, G. M., Hickish, J., MacMahon, D., & Gary, D. E. 2016, Journal of Astronomical Instrumentation, 5, 1641009

Nitta, N., & Kosugi, T. 1986, Solar Physics, 105, 73

Pesnell, W. D., Thompson, B. J., & Chamberlin, P. C. 2012, Solar Physics, 275, 3

Qiu, J., Cheng, J. X., Hurford, G. J., Xu, Y., & Wang, H. 2012, Astronomy and Astrophysics, 547, A72

Reznikova, V. E., Melnikov, V. F., Ji, H., & Shibasaki, K. 2010, Astrophysical Journal, 724, 171

Reznikova, V. E., Melnikov, V. F., Shibasaki, K., Gorbikov, S. P., Pyatakov, N. P., Myagkova, I. N., & Ji, H. 2009, Astrophysical Journal, 697, 735

Saint-Hilaire, P., & Benz, A. O. 2002, Solar Physics, 210, 287

Saint-Hilaire, P., Krucker, S., & Lin, R. P. 2010, Astrophysical Journal, 721, 1933

Sakao, T., Kosugi, T., Masuda, S., Yaji, K., Inda-Koide, M., & Makishima, K. 1996, Advances in Space Research, 17

Schou, J., et al. 2012, Solar Physics, 275, 229

Schwartz, R. A., Csillaghy, A., Tolbert, A. K., Hurford, G. J., McTiernan, J., & Zarro, D. 2002, Solar Physics, 210, 165

Schwenn, R. 2006, Living Reviews in Solar Physics, 3, 2

Shibata, K., & Magara, T. 2011, Living Reviews in Solar Physics, 8, 6

Silva, A. V. R., Wang, H., & Gary, D. E. 2000, Astrophysical Journal, 545, 1116

Smith, D. M., Share, G. H., Murphy, R. J., Schwartz, R. A., Shih, A. Y., & Lin, R. P. 2003, Astrophysical Journal, Letters, 595, L81

Sturrock, P. A. 1966, Nature, 211, 695

Sui, L., & Holman, G. D. 2003, Astrophysical Journal, Letters, 596, L251

Takakura, T. 1972, Solar Physics, 26, 151

Tandberg-Hanssen, E., & Emslie, A. G. 2009, The Physics of Solar Flares

Torre, G., Pinamonti, N., Emslie, A. G., Guo, J., Massone, A. M., & Piana, M. 2012, Astrophysical Journal, 751, 129

Usoskin, I. G. 2017, Living Reviews in Solar Physics, 14, 3

Wang, H., Gary, D. E., Zirin, H., Schwartz, R. A., Sakao, T., Kosugi, T., & Shibata, K. 1995, Astrophysical Journal, 453, 505

Wang, H., et al. 2017, Nature Astronomy, 1, 0085

Wang, S., Liu, C., Deng, N., & Wang, H. 2014, Astrophysical Journal, Letters, 782, L31

Wang, S., Liu, C., Liu, R., Deng, N., Liu, Y., & Wang, H. 2012, Astrophysical Journal, Letters, 745, L17

Wheatland, M. S. 2005, Space Weather, 3, S07003

Wheatland, M. S., Sturrock, P. A., & Roumeliotis, G. 2000, Astrophysical Journal, 540, 1150

White, S. M., Krucker, S., Shibasaki, K., Yokoyama, T., Shimojo, M., & Kundu, M. R. 2003, Astrophysical Journal, Letters, 595, L111

White, S. M., et al. 2011, Space Science Reviews, 159, 225

Wiegelmann, T. 2004, Solar Physics, 219, 87

Wiegelmann, T., Inhester, B., & Sakurai, T. 2006, Solar Physics, 233, 215

Wiegelmann, T., Lagg, A., Solanki, S. K., Inhester, B., & Woch, J. 2005, Astronomy and Astrophysics, 433, 701

Woods, T. N., et al. 2012, Solar Physics, 275, 115

Zharkov, S., Green, L. M., Matthews, S. A., & Zharkova, V. V. 2013, Solar Physics, 284, 315